Spring 2022

The Active Tail in the MMS Era: An Ion Perspective

Anthony Jason Rogers
University of New Hampshire, Durham

The Active Tail in the MMS Era
An Ion Perspective

By

Anthony Jason Rogers
B.S. Physics, University of Iowa, 2015
M.S. Physics, University of New Hampshire, 2020

DISSERTATION

Submitted to the University of New Hampshire
in Partial Fulfilment of
the Requirements for the Degree of

Doctor of Philosophy
in
Physics

May, 2022

This dissertation has been examined and approved in partial fulfillment of the requirements for the degree of Doctor of Philosophy in Physics by:

Charles J. Farrugia, Research Professor of Physics
Thesis Adviser

Roy B. Torbert, Professor Emeritus of Physics

Amy Keesee, Associate Professor of Physics

Elena Long, Assistant Professor of Physics

Terry Forbes, Research Professor Emeritus of Physics

On 27 April, 2022.

Approval signatures are on file with the University of New Hampshire Graduate School.

To Grandma Xenia 'Babe' Rogers
For all the conversations we never got to have.

Acknowledgments

This work has been supported, in part, by NASA contract 499878Q

Several people have been instrumental in helping me get this far, a village of family and friends who have supported me through trials, failures, and this ultimate success:
Mom & Dad, Tim, Sean, Cindy, Jacie, Xander, and Eli thank you for patience over many family vacations while I droned on and on about 'space stuff.'
Alli, Zach, Luke, Carol, Jennie, Jessie, Nick, Zia, Trish, Diego, Leo, Jaime, Bruce, Sarah, Jon, Hallie, Kae, Teresa, and so many more, you are the distributed support system I survive on.
Theresa, Carolyn, and Krista, there will never be thanks enough.

I love you all.

TABLE OF CONTENTS

LIST OF TABLES

LIST OF FIGURES

Abstract

The Earth's magnetic field has a complex and dynamic relationship with the greater solar system. The solar wind and interplanetary magnetic field extend the influence of the Sun's atmosphere to the orbit of Earth and well beyond, carrying charged particles in a constant stream of varying density and velocity. These solar influences carry energy which interacts with every object they encounter, including the Earth and its magnetic field.

The primary mechanism for the energetic interaction and exchange of energy between the Earth's magnetic field and the solar wind is called Magnetic Reconnection, a process by which two opposing magnetic fields may cancel each other in a limited region and allow the plasma restrained by each to cross the boundary between magnetic fields and interact. The effects of this interactions are as varied as they are wonderful, including the aurora, intercontinental radio communications, and threats to orbiting satellites. As such, understanding magnetic reconnection and its effects is an important task for space science research.

This work is devoted to characterizing and identifying magnetic reconnection region in one part of the Earth's magnetosphere, the magnetotail, as well as the conditions in the magnetotail necessary for reconnection to begin. This is done through the analysis of data from the Magnetospheric Multi-Scale Mission, a fleet of four identical orbiting observatories designed specifically to study reconnection. Methods to identify reconnection derived from historical assumptions as well relatively new techniques, so-called Scalar Parameters, are employed and compared. Finally, a combination of these methods is brought to bear in an attempt to understand why magnetic reconnection in the magnetotail occurs more often in

some locations than others.

Some Fundamental Physics Concepts

The subject of this dissertation is magnetic reconnection and the magnetospheric context in which it occurs in the geomagnetic tail. This is, it is safe to say, a niche subject within the much broader field of physics. As such I am providing below a short introduction to some of the key physics concepts and equations which will govern much of the work to follow. While this is by no means a comprehensive review of the physics associated with this subject, I hope it does provide enough of an introduction to understand what follows for those who have not the time or inclination for a more complete study of the subject.

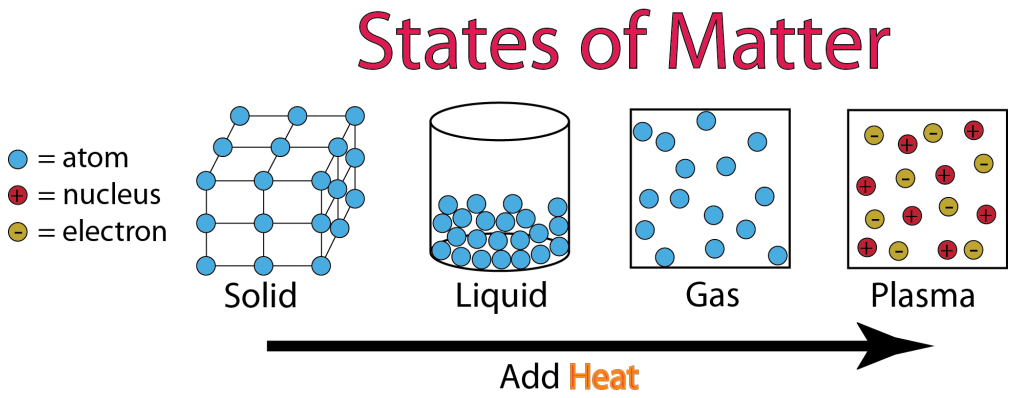

Figure 1: The four common states of matter. See text for details. [Wikicommons: Public Domain]

A plasma in this context is a fourth state of matter beyond gas in the hierarchy of organisation of matter. If we think about matter on an atomic level, a solid represents atoms all arranged together in a repeating pattern (see Figure 1a). In all matter there is some random motion of the atoms; a 'jiggling' around of each individual atom even in solids

as the atoms stay in their place while vibrating a bit. This random 'jiggling' is what is referred to as heat in matter. The more heat matter has, the more the atoms jiggle about.

If we add more heat to our ideal solid described above the atoms in their neat, organized, repeating pattern will jiggle more; the more heat we add the more the atoms will move. Eventually, the atoms will be jiggling and vibrating so much that they can't stay in their place in the pattern and all of the atoms just mush around each other in a puddle; the solid we started with has become a liquid (Figure 1b). Extending this concept and adding more and more heat to the matter, the atoms will continue to move around more and more until they aren't even staying near their neighbors at all any more and instead start flying all around the room; the liquid has become a gas (Figure 1c).

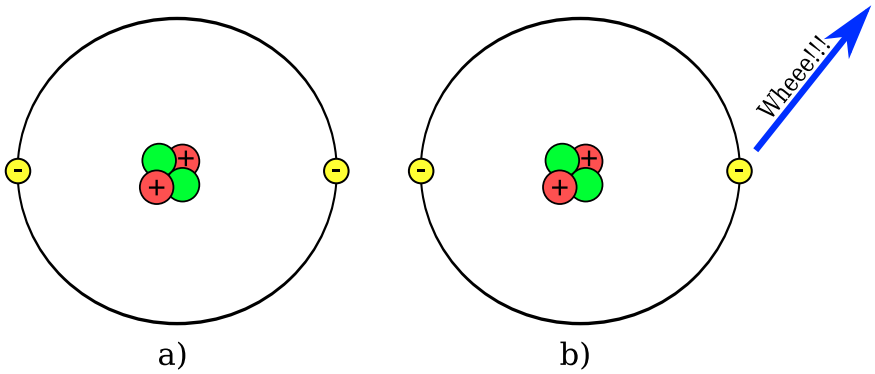

Figure 2: ***a)*** A representative view of the atom. At the center is the nucleus made up of positively-charged protons (red) and electrically neutral neutrons (green). Orbiting around the nucleus are negatively-charged electrons (yellow). ***b)*** When the atom absorbs sufficient heat energy one or more electrons will no longer be able to maintain their normal orbit about the nucleus and will move indepentantly of the remainder of the now net-positively-charged ion. The degree of enthusiasm which electrons feel on achieving this freedom is not well-understood.

These are the three states of matter generally taught in school. To get to "plasma" we need to look at the atoms themselves. A simple picture of an atom has the heavy, positively-charged protons (along with some slightly heavier neutrons) all collected together in the center or the nucleus of the atom, while the relatively light, negatively-charged electrons orbit around the nucleus in layers determined by how much energy each one has (see Figure

2). The whole time we've been adding heat to matter in our example the atoms have gained energy and jiggled around more and more, but so have the electrons, protons, and neutrons. If we keep adding heat energy to the gas we had before, the individual atoms will jiggle and bounce more and more, but the electrons inside each atom will gain energy as well and orbit faster and faster and jiggle and bounce more and more themselves. Eventually, there will be enough heat in the atom that the electrons stop orbiting the nucleus and instead fly off on their own, leading to a gas of separated negatively-charged electrons and positively-charged nuclei all bouncing around chaotically (Figure 1d). This is a plasma. Plasma makes up the vast bulk of observed matter in the universe; the Sun, stars, fluorescent and neon lights all are made up of plasma. The process of heating up an atom or gas until it starts losing electrons is called ionisation and we call nuclei which have lost some or all of the electrons that used to orbit them ions.

Because the particles which make up plasma have electrical charge, they can carry an electrical current and can both generate and be moved around by magnetic forces. Magnetic fields are also common in the universe; the Sun and most of the planets in our solar system generate their own magnetic fields due to their rotation and composition of their inner layers. These magnetic fields behave similarly to gigantic bar magnets aligned (roughly) along the axis of rotation of each star or planet (see Figure 3). Magnetic fields, like electric fields, have both a strength and direction. If two magnetic fields get close to each other then the net magnetic field at any point is going to be the combination of contributions from each individual field. This means that if the two fields are pointed in opposite directions they can cancel each other out where they meet; or can change direction to be different from either contributing field. This will change the shape of the field and will release or redistribute energy carried by the magnetic fields.

If a plasma is mixed in with a magnetic field then these field interactions become more interesting. For example, if two oppositely-directed fields interact while each carries a plasma,

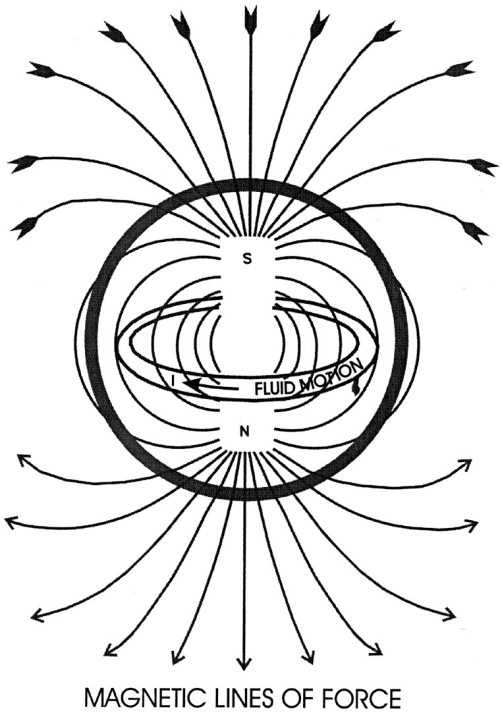

Figure 3: A simple schematic of the magnetic field generated by the inner dynamo of most stars and planets, including the Earth and the Sun. Rotation of a conducting inner layer (such as the molten metallic core of the Earth) will generate a magnetic field which will appear similar to the field of a common bar magnet away from the rotating dynamo. [Vallee, 1998]

then the point where those field cancel each other out will lead to mixing of the plasma from each. Similarly, the energy carried by the magnetic fields and that carried by the plasmas will also become mixed and move around. This interaction is what is meant by **magnetic reconnection**; the transfer of energy between interacting magnetic fields and the plasma carried by them.

The first of the equations which govern these interactions is the Lorentz force $\vec{F} = q\vec{E} + q\vec{v} \times \vec{B}$ where the force applied onto a charged particle in the plasma is determined by the charge of that particle (q) the electric field present ($\vec{E}$) the motion of the particle ($\vec{v}$) and the magnetic field ($\vec{B}$) . Most of the time in plasmas in space and especially near the Earth the contribution to this force by the electric field is very small compared to that of the magnetic field. Places where the electric field exerts more influence than the magnetic field are of particular interest; areas near magnetic reconnection are usually such places.

The application of the Lorentz force in an environment with a static magnetic field and small electric field leads to the concept of Guiding Center Motion; that is, treating the motion of a charged particle entirely in relation to a Guiding Center. This guiding center is represented by the common conceptual aid of a magnetic field line. As a magnetic field is, mathematically speaking, a vector field it does not actually have lines running through it. However, the concept of magnetic field lines to visualize the direction and magnitude of the vector field is useful (see Figure 3). Accepting magnetic field lines as useful conceptual aids, we can then imagine the motion of a charged particle in relation to those field lines. The magnetic component of the Lorentz force $q\vec{v} \times \vec{B}$ indicates, by way of the cross-product operator $\times$, that the magnetic field applies force in proportion to the perpendicular motion of the particle; *i.e.* if the particle is moving perfectly parallel to the magnetic field $\vec{B}$, then it will experience no force from $\vec{B}$.

The net result of the perpendicular force is to cause a charged particle to orbit around a particular magnetic field line (its guiding center) as it finds equilibrium in the absence of

other external forces. As this still does not preclude any motion parallel to the magnetic field the particle may have carried into this situation with it, the net result is for the particle to gyrate around the guiding center in a helical path (see Figure 4). For a charged particle of mass m, charge q, and speed perpendicular to the magnetic field $v_\perp$ associated with a magnetic field of strength $|B|$ the radius of the orbit about the filed line guiding center will be the gyroradius $r_g = \frac{mv_\perp}{|qB|}$ and the angular gyrofrequency about which it orbits the guiding center field line is $\omega = \frac{|qB|}{m}$. It should be reiterated that this behavior happens in the absence of other forces on the particles, such as an external electric field. An equivalent statement is that the magnetic moment $\mu = \frac{mv_\perp^2}{2B}$ is constant; this is referred to as the first adiabatic invariant. If an external force operates on the particle in such a way that μ changes significantly over a period on the same scale as that of the gyromotion (*i.e.* a gyroperiod $t_g = \frac{2\pi m}{|qB|}$), then the first adiabatic invariant is said to be broken and the particle is no longer 'frozen into' the magnetic field. This state is a key concept behind magnetic reconnection discussed later on.

The other equations which describe the collective behavior of plasmas in the regions discussed here are called Maxwell's Equations (see Table 1). These equations help us describe the collective behavior of plasma as opposed to just one particle at a time. In these the plasma is represented as a collection of charges (ρ as charge density is the number of electrons or negative charges subtracted from the number of protons or positive charges in a given volume) or as the carriers of electrical current ($\vec{j}$ being current density). The nabla symbol (∇) represents a change over distance and $\frac{d}{dt}$ represents a change over time for whatever parameter each is next to. ϵ_0 and μ_0 are both constants to make the units come out right. Thus the change in the shape of an electric field $\nabla \cdot \vec{E}$ is related to the amount of charge or number of charged particles in that region (ρ). Similarly, the shape of a magnetic field $\nabla \times \vec{B}$ is related to the motion of charged particles or current ($\vec{J}$).

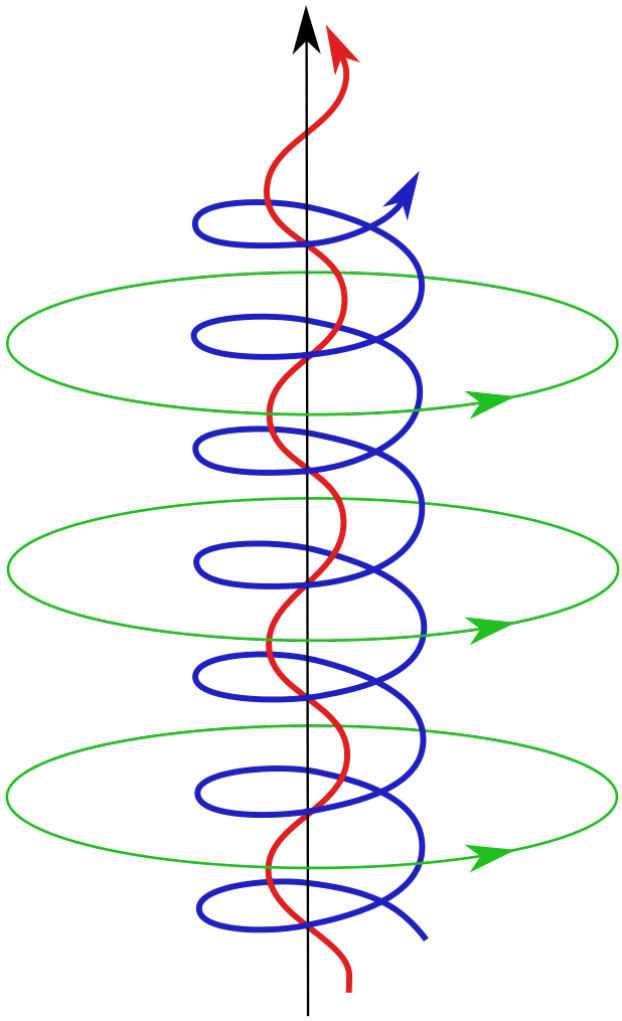

Figure 4: The guiding center field line (black) and the orbits of particles with different amounts of perpendicular and parallel energy associated with them. Those with no parallel velocity (green) will simple orbit around the guiding center without any other motion. Those with more perpendicular energy than parallel energy will move along the guiding center while still spiralling tightly about the guiding center (blue). Those with significant parallel velocity will move mostly along the guiding center with only small gyrating orbits about the field line (red). [Public Domain]

Gauss' Law ($\vec{E}$)	Gauss' Law ($\vec{B}$)
$\nabla \cdot \vec{E} = \frac{\rho}{\epsilon_0}$	$\nabla \cdot \vec{B} = 0$
Faraday's Law	**Ampere's Law**
$\nabla \times \vec{E} = -\frac{\delta \vec{B}}{\delta t}$	$\nabla \times \vec{B} = \mu_0 \vec{j}$

Table 1: The differential forms of Maxwell's Equations. The constants ϵ_0 (the permittivity of free space) and μ_0 (permeability of free space) are a consequence of using SI units. Note that Ampere's law as written here neglects Maxwell's addition

CHAPTER 1

Introduction & Historical Overview

In order to describe the advances and developments I am responsible for in the field, some conceptual review and historical background might be useful.

1.1 The Beginnings of Geoscience

The existence of the Earths magnetic field has been known, if not understood, since the invention of the compass two or three millennia ago. Changes in compass behavior related to observations of the aurora have been recorded since the age of discovery and changes to both have been related to activity on the surface of the Sun since the famous Carrington event of 1859. Becequerel and Goldstein independently hypothesized in the late 19th century that the influence of the Sun on the Earths magnetic field was communicated by way of a stream of charged particles eminating from the Sun. Observations of comets throughout the early 20th century, combined with expanding observations of the aurora and geomagnetic storms, led to work by Chapman & Ferraro (e.g. [Chapman and Ferraro, 1931]), Alfvén (e.g. [Alfven and Lindblad, 1945, Alfvén, 1957]) and others indicating that this stream must be fairly constant, with only occasional variations in strength, must consist of both positively-charged protons and negatively-charged electrons, and must carry its own magnetic field embedded within in. Eugene Parker combined all of these observations into a theoretical framework which treated the stream, what he called the "solar wind" [Parker, 1958b], as a magnetized, conducting fluid [Parker, 1958a]. Alfvén and Parker's magneto-hydrodynamic

(MHD) approach became the primary framework to study and understand interactions of the interplanetary solar wind plasma with the Earths magnetic field.

1.2 The Dungey Cycle and the Active Magnetosphere

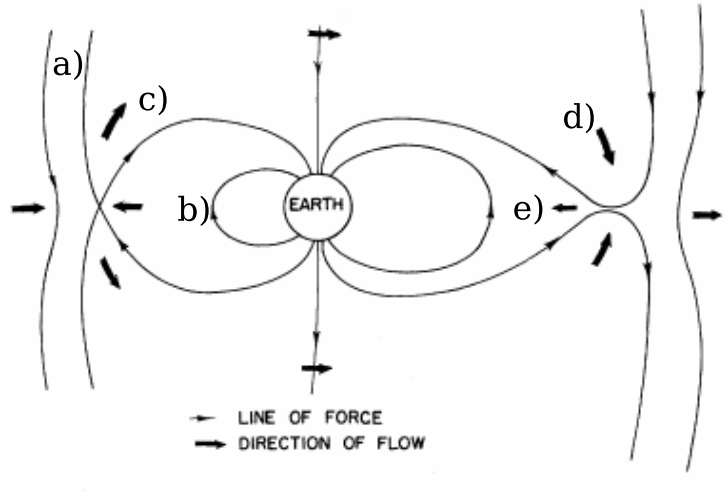

Figure 1.1: The original schematic depiction of the Dungey Convection Cycle. [Dungey, 1961]

Around this same time Dungey was considering the interaction of such a Solar Wind on the Earth's magnetosphere [Dungey, 1961]. He proposed that the solar wind plasma, combined with a southward-pointing interplanetary magnetic field (IMF; Figure 1.1*a*), would interact with the northward-pointing magnetic field of the Earth (Figure 1.1*b*) leading to neutral points where the magnetic fields would cancel each other out. This would allow for plasma in the solar wind and the Earth's magnetosphere to mix, reducing overall plasma pressure in the magnetosphere and introducing higher-energy particles from the solar wind. This would also lead to so-called 'open flux' where magnetic field lines coming from the Earth's magnetic poles are connected to the IMF instead of to the opposite pole (Figure 1.1*c*). These field lines would then be carried by the flow of the solar wind away from the Sun and over the Earth to collect or 'pile-up' on the nightside (Figure 1.1*d*). As the magnetic

flux collected, magnetic pressure would also increase, driving magnetic field lines together until they once again closed from one pole to the other and began rotating back to the dayside to begin the process again, a process now referred to as the Dungey cycle.

Magnetic pressure and flow pressure from the solar wind also have the effect of distorting the magnetosphere from its ideal "Dumbo ears" dipolar shape (see Figure 3). On the dayside, the magnetic field is compressed or squished towards the Earth by the combined flow pressure of the solar wind plasma and the magnetic pressure of a northward-pointing IMF in a manner first described by Chapman & Ferraro [Chapman and Ferraro, 1931](Figure 1.2a). On the nightside the same forces cause the Earth's magnetic field to stretch out away from the Sun [Alfvén, 1957, Dungey, 1963] in a manner not unlike the tail of a kite stretching out nominally to at least the distance of lunar orbit and often several times that length (e.g. [Dungey, 1965, Gombosi et al., 1998], Figure 1.2b). The shape of this geomagnetic tail was well-described by Coroniti & Kennel [Coroniti and Kennel, 1972] using the parameters described as well as the electrostatic potential measured across the polar cap. Pilipp & Morfill went further to provide an analytical description of how the plasma and magnetic flux convection would create a compressed sheet of trapped plasma in the center of the tail, between the northern and southern halves or lobes [Pilipp and Morfill, 1978].

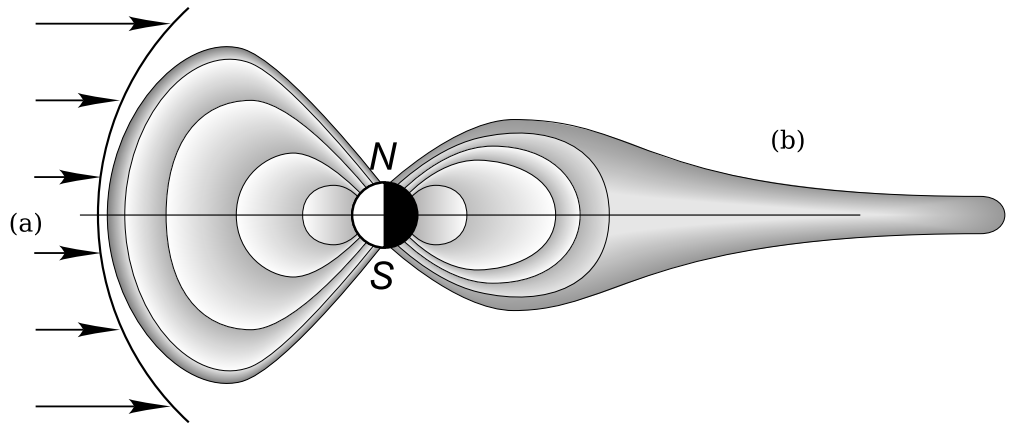

Figure 1.2: A picture of the normal, quiet magnetosphere. [NASA: Public Domain]

Observational support for this tail configuration was amply provided by a series of missions in the early 1960s. Ness, Heppner, and others used *in situ* measurements from the IMP 1, Explorer 10, and other missions to show a magnetic field stretched out from the polar caps, leaving a neutral sheet of relatively dense plasma between the northern and southern lobes ([Ness, 1965] and references therein). Ness also points out that the configuration as observed provides direct observational support to the open magnetosphere convection model of Dungey.

Further support for the Dungey model was found when early magnetic field measurements in the IMF were compared to ground magnetometer readings during Polar Magnetic Substorms (referred to hereafter as simply 'substorms')[Fairfield and Cahill, 1966]. Substorms comprise a disturbed geomagnetic field, characterised by strong shifts in the horizontal component of the Earth's magnetic field. This is measured by means of magnetometers located around the world, particularly in and around the Arctic circle as these connect to magnetic field lines which stretch to regions of the magnetosphere of scientific interest (*e.g.* the distant magnetotail and the dayside magnetopause). The same substorm events are associated with increased auroral activity, which has been well-correlated with the behavior of the geomagnetic field during substorms [Akasofu, 1964].

Fairfield & Cahill reported observing substorms reliably occurring after the North-South component of the IMF turned from North to South, often with a delay of up to an hour. Contrariwise, a steady North component to the IMF was typically associated with quiet geomagnetic conditions. In many ways these observations are showing the beginning and end of the chain of energy transfer required for substorms without considering the middle. According to the Dungey model, a southward IMF will cause the dayside magnetosphere to be 'eroded'(Figure 1.1). This is due to the Earth's magnetic field being primarily northward-pointing, therefore a southern component to the IMF will cancel out part of the Earth's magnetic field on the dayside, effectively 'breaking' those field lines (Figure 1.3-1) and allow-

ing the ends to be carried by the solar wind (Figure 1.3-2). The magnetic flux thus released from the dayside will then flow over the Earth's poles to the nightside where it will build-up in the geomagnetic tail (Figure 1.3b). Eventually the pressure of this built-up magnetic flux will compress the northern and southern halves of the 'disconnected' magnetic field lines in the lobes and 'reconnect' them in the tail neutral sheet [Dungey, 1963] (Figure 1.3-3). *In situ* magnetometer data showed that the amount of magnetic flux in the tail increased by a significant amount during periods of southern IMF and ground magnetometer readings suggested that the tail first stretched out as the IMF turned southward and then relaxed over time after the IMF turned north [Russell and McPherron, 1973], which is consistent with geomagnetic field lines being opened to the IMF on the dayside by reconnection and closed again to each other in the tail. This chain of magnetic flux transfer from the dayside to the magnetotail and then towards the Earth before convecting back to the dayside accounts for the delay in the measurements in the IMF and the effects seen on the ground [Fairfield and Cahill, 1966]. All three stages were observed in sequence during an event in 1968 [Aubry et al., 1970], offering clear evidence of the Dungey cycle in action.

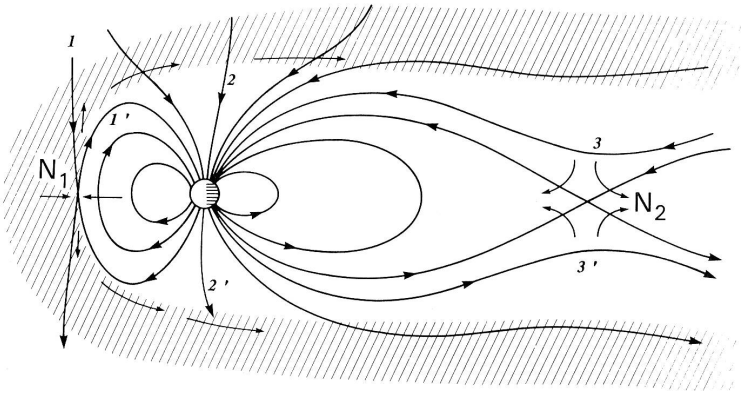

Figure 1.3: The modified Dungey picture showing the locations where field lines are broken and reconnected. [NASA: Public Domain]

Additionally, particle measurements both in the tail (e.g. [Frank, 1965]) neutral sheet as well as much closer to earth (e.g. [McDiarmid and Burrows, 1965]) suggest that plasma in the

tail neutral sheet is accelerated earthward during these substorms, serving as a source of both inner magnetosphere hot plasma populations as well as effects such as the aurora. Better instrumentation provided better *in situ* observations of particle acceleration in the near-tail neutral sheet. Frank et al. (1976) showed electron and ion spectrogram observations from the IMP-8 satellite during several encounters with localized regions of strong plasma heating and acceleration at or near tail neutral sheet crossings, dubbed 'Magnetotail Fireballs.' The direction of both ions and electrons in these flows along the Earth-Sun line were strongly correlated with the North-South component of the magnetic field; Earthward flows were embedded with northward magnetic fields, indicating a closed magnetic field line connected at each end to the Earth, while tailward flows were associated with southward magnetic fields, indicating that the field lines were connected to the IMF rather than the Earth's magnetic poles. In their conclusion, Frank et al. state that "the merging of magnetic field lines... is probably the dominant acceleration mechanism participating in magnetotail dynamics.."

1.3 Magnetic Reconnection

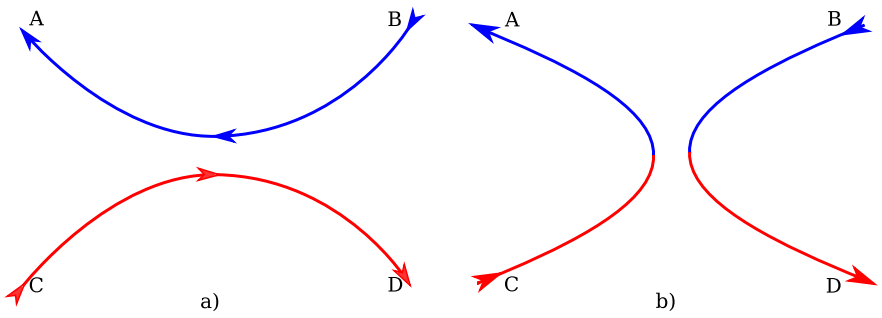

Figure 1.4: A before ***a)*** and after ***b)*** picture of magnetic reconnection. Two magnetic field lines, one running from **B** to **A** (blue) and another running from **C** to **D** which approach each other. At the point of 'contact' they will cancel each other out, producing a magnetic null (not pictured). The magnetic field can then be reconfigured with the magnetic flux from **C** now connected to **A** and that from **B** connected to **D**. In essence, the magnetic field lines have broken and 'reconnected' into a new topological configuration.

Magnetic field lines merging or otherwise interacting is not a particularly unique or spec-

tacular event in isolation. One can cause the interaction of magnetic fields by simply placing two magnets near each other in any arbitrary orientation (Figure 1.4). The particularly interesting aspect of reconnection in the context of space plasma physics is the addition of a plasma embedded within the magnetic fields involved. A population of charged particle co-located with a changing magnetic field means that the energy involved is not only that of the magnetic flux transferring from one location or geometry to another, but also the kinetic energy and heat of the plasma associated with it. Adding to the complications is the fact that a magnetic field can not only apply a force on a particle in motion via the Lorentz force, but is also *generated* or modified by moving charges, by way of Ampere's law (see Table 1). Exploring and describing this complicated state of affairs has been the work of four generations of scientists throughout the space age.

Plasma acceleration due to magnetic field line merging, also referred to as magnetic field annihilation, magnetic nulls, or magnetic reconnection, had been discussed as a theoretical means of accelerating the solar wind since the 1940s (e.g. [Hoyle, 1949]). The mechanism for converting magnetic energy to kinetic energy in the plasma was initially described in detail using MHD by Eugene Parker after a description by P.A. Sweet ([Parker, 1957] and references therein). The fundamental principal behind the Sweet-Parker picture of magnetic reconnection is that of two oppositely directed magnetic fields (for the sake of argument, one may be labelled positive while the other is negative) which approach each other with a plasma embedded in both. As the fields approach each other they will cancel each other out, the sum of a positive and negative trending towards zero, creating a thin layer of null magnetic field strength but retaining the plasma. The magnetic pressure of these colliding magnetic fields will squeeze the plasma between them, increasing the plasma pressure. The plasma, no longer tied to either magnetic field inside the null between them, will then be forced along the interface between interacting fields, accelerating out the ends of the interaction region (Figure 1.5).

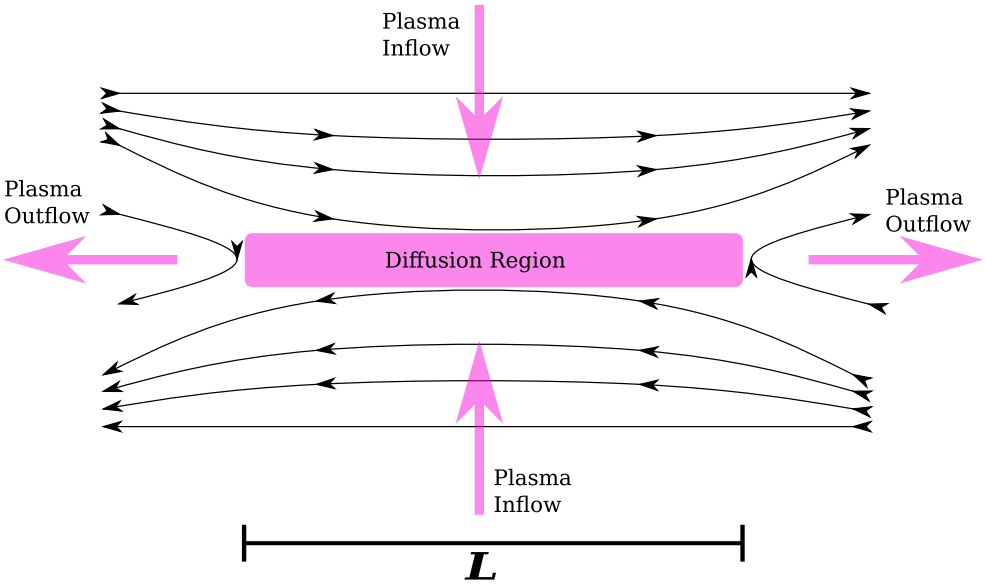

Figure 1.5: A schematic look at the Sweet-Parker reconnection model. Plasma (magenta arrows) flows in towards the neutral sheet between oppositely directed magnetic fields (black lines). The compression of the plasma between magnetic fields causes diffusion of magnetic field energy into heating of the plasma in the Diffusion Region. The increase in plasma pressure drives the plasma out the 'sides' of the reconnection region, perpendicular to the inflow direction.

While this theory was instrumental in first providing an analytical model for converting stored magnetic energy into plasma energy, it was insufficient to explain the rate at which that energy conversion had been observed in solar flares. The length of the current sheet (*i.e.* the interface between interacting magnetic fields) required to reach the observed plasma velocities was so large that it would require more than a hundred times the observed timescale of solar flare activity to achieve the observed energies. In short, Sweet-Parker reconnection was considered too slow to match observations. A refinement of Sweet-Parker reconnection was proposed by Petschek which utilized MHD waves to increase the reconnection rate and decrease both the size of the current sheet as well as the time required to reach solar flare energies [Petschek, 1964].

These MHD models of reconnection were further extended by Sonnerup (1970) and Yeh and Axford (1970) (and brilliantly summarized and explained by Vasyliunas; [Vasyliunas, 1975]) to clarify the necessary two-dimensional geometry of plasma flow in and near the merging interface between magnetic fields. However, all the work up to this point had been done assuming a uniform fluid of plasma moving throughout the system; the compressibility of the fluid being considered only in later models [Yeh and Axford, 1970]. Vasyliunas pointed out this omission as well as detailing the unrealistic nature of the boundary conditions necessary to each model. He invoked the generalized Ohm's law [Rossi and Olbert, 1970, Dungey, 1958] to imply that the differential behavior of electrons and ions within the reconnection region might be of interest.

A Short Digression Regarding Ohm's Law

The full(ish) generalized Ohm's law is derived here from the equation of motion for electrons (as opposed to the combined equations of motion for electrons and ions). Traditionally, Ohm's law is written so as to include a myriad of electron effects but with few mentions of ion motion except as is included in the concept of current density $\vec{j}$. This is due to the mass

ratio between electrons and protons being greater than 1800, indicating that any changes in ion velocity will be miniscule compared to those of electrons in the same conditions. By accounting for all of the myriad possible individual forces acting on electrons in the region of interest we are essentially applying Newton's Second Law ($\vec{F}_{net} = \sum \vec{F}_{individual}$ or the net force on an object is the sum of all individual forces on that object). Additional effects from ions would not fundamentally change the concepts explored in this derivation, only add additional terms to the categories which will be discussed below.

Throughout the derivation $\frac{\mathrm{d}}{\mathrm{dt}}$ is defined as the convective (or material) derivative such that $\frac{\mathrm{d}}{\mathrm{dt}} = \frac{\delta}{\delta \mathrm{t}} + (\vec{u} \cdot \nabla)$.

$$-\vec{F_e} = m_e \frac{\mathrm{d}\,\vec{u_e}}{\mathrm{dt}} = \underbrace{q_e(\vec{E} + \vec{u_e} \times \vec{B})}_{\text{Lorentz Force}} - \underbrace{\frac{1}{n_e}\nabla \cdot \bar{P}_e}_{\text{Electron Pressure}} - \underbrace{m_e \nu_{ei}(\vec{u_e} - \vec{u_i})}_{\text{Collisions}}$$

Where $\vec{u_i}$ = Ion bulk velocity, $\vec{u_e}$ = Electron bulk velocity, and $\nu_{ei} \equiv$ Collisional Frequency

Apply the definition of:

$$\vec{j} = ne(\vec{u_i} - \vec{u_e}) \Rightarrow \vec{u_e} = \vec{u_i} - \frac{\vec{j}}{ne}$$

$$\Rightarrow \frac{m_e}{q_e}\frac{\mathrm{d}\,\vec{u_e}}{\mathrm{dt}} = \vec{E} + \vec{u_e} \times \vec{B} - \frac{1}{n_e q_e}\nabla \cdot \bar{P}_e - \frac{m_e \nu_{ei}}{ne^2}\vec{j}$$

Assume plasma consists entirely of electrons and protons such that:

$$q_e = q_i = e$$

$$\text{And let } \eta = \frac{m_e \nu_{ei}}{ne^2}$$

$$\Rightarrow \frac{m_e}{e}\frac{\mathrm{d}\,\vec{u_e}}{\mathrm{dt}} = \vec{E} - \frac{1}{ne}\vec{j} \times \vec{B} + \vec{u_i} \times \vec{B} + \frac{1}{ne}\nabla \cdot \bar{P}_e - \eta\vec{j}$$

Now we rearrange terms:

$$\boxed{\underbrace{\vec{E} = \eta\vec{j}}_{\text{Classical Ohm's Law}} - \underbrace{\vec{u_i} \times \vec{B}}_{\text{Ion Convection}} + \underbrace{\frac{1}{ne}\vec{j} \times \vec{B}}_{HallTerm} - \underbrace{\frac{m_e}{e}\frac{\mathrm{d}\,\vec{u_e}}{\mathrm{dt}}}_{e^- \text{ Inertial Term}} - \underbrace{\frac{1}{ne}\nabla \cdot \bar{P}_e}_{e^- \text{ Pressure}}} \tag{1.1}$$

Resistivity η in a medium is largely dependent on physical collisions of particles within the medium with one another, impeding the motion of any given particle. However, in plasmas typical of the regions surrounding the Earth, as well as in interplanetary space, the density is very low, meaning that there is very little resistance to motion due to collisions and electrical conductivity in the plasma approaches infinity. Plasmas with such low densities as those with which this work is primarily concerned enjoy this state of affairs and are commonly referred to as "collisionless" plasmas. That being the case, the first term on the

right side of Equation (1.1) typically goes to zero.

The convective electric field, represented by $\vec{u}_i \times \vec{B}$, is the dominant source of electric fields in MHD. The ion bulk velocity $\vec{u}_i$ is often taken as a proxy for the bulk flow of the entire plasma, electrons and ions both, due to ions carrying the vast majority of the mass. This means that if both electrons and ions are frozen into a magnetic field then their velocities are also locked together, meaning that the ions carry the bulk of the kinetic energy of the magnetized plasma. In such regions this will be the only term of significance with all the other right-hand side terms of Equation (1.1) ignored as being orders of magnitude smaller than the convective electric field described by it.

The Hall term, named for the Hall effect and the experimentalist Edwin Hall who discovered it, requires the differential flow of electrons and ions within the plasma in order to generate the current $\vec{j}$; in other words the ions and electrons cannot be moving as a single fluid or medium as supposed by Sweet and Parker, Petschek, Sonnerup, or Yeh and Axford. What's more, the motion of some of these particles must be in a different direction than the local magnetic field in order for the $\times\vec{B}$ operator to be non-zero. In practical terms this means that the electrons, being lighter and more easily influenced by the magnetic field, will continue to move with the magnetic field even as the field weakens and changes near the interface between reconnecting fields, while the ions are too heavy and slow to keep up with the rapid changes to the field around them. This leads to the ions becoming detached from the dominion of the magnetic field (or demagnetized) and moving separately from both the magnetic field and the electrons which are still attached to it. The differential motion creates a current pointed away from the magnetic field, leading to the Hall effect and a Hall electric field.

Next in Equation (1.1) is the electron inertial term which represents the accumulated momentum of the electrons. When Ohm's law is derived from a combination of both electron and ion equations of motion this term becomes the convective derivative of the current

density $\frac{\mathrm{d}\vec{j}}{\mathrm{dt}}$ with some additional cross terms. Given the near total lack of magnetic field influence in regions where this term will deviate significantly from zero and the rapid and easy acceleration of electrons in such a case, leaving this term as only considering the acceleration of electrons is not a wholly unreasonable approximation.

Finally, we have the electron pressure (or stress tensor) term which offers a significant contribution in relation to the other terms already discussed only when the electrons move agyrotropically; that is, when the electrons no longer obey the first adiabatic invariant. This term and the electron inertial term are only significant once the electron motion is no longer dominated by the motion of the magnetic field, or at interaction scale lengths smaller than the typical electron gyroradius ($\approx 5 - 10km$ in the geomagnetic tail).

It should be noted that none of the above derivation or physical interpretations are derived from or dependent on MHD. By beginning from the equation of motion for a representative electron this expression of a generalized Ohm's law is essentially a kinetic theory of plasma behavior.

1.4 New Thinking on Reconnection

Thinking regarding magnetic reconnection evolved as a reaction to the weaknesses pointed out by Vasuliunas. In 1979 Sonnerup described a modified mechanism for reconnection which departed from the traditional approach of assuming the plasma was a single, continuous medium of uniform composition. Again invoking the Generalized Ohm's Law he described a two-fluid model where first the ions and then electrons ceased to behave according to a MHD convective paradigm and instead were primarily influenced by the Hall, pressure, and inertial terms identified in the Ohm's law above. While a Diffusion Region, defined as the region around the center of the reconnecting current sheet where the diffusion of energy into heat was caused by collisional, turbulent, or other broadly resistive effects [Sonnerup, 1979], had long been a key feature of magnetic reconnection theory, Sonnerup postulated a

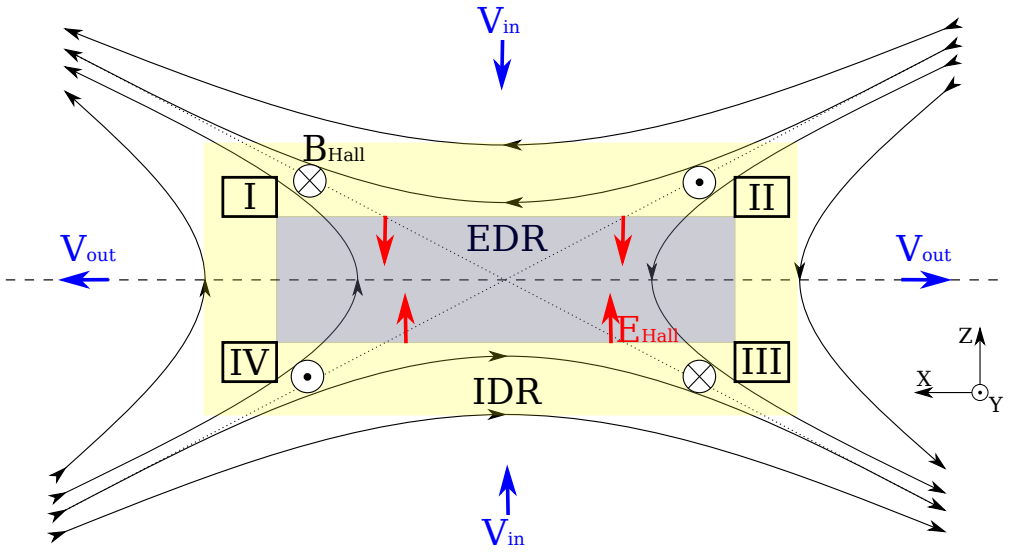

Figure 1.6: A schematic of Hall reconnection, assuming a two-species plasma.

two-stage structure previously unexplored. The (outer) Ion Diffusion Region (IDR, Figure 1.6) on the scale of the ion gyroradius or inertial length was where ions convecting towards the reconnecting current sheet were demagnetized and engaged in meandering motion while electrons remained magnetized, convecting with the remaining (weak) magnetic field. An (inner) Electron Diffusion Region (EDR, Figure 1.6), embedded within the IDR and on the scale of the electron inertial length, was then where electrons were in turn demagnetized in the immediate neighborhood of the magnetic null between interacting magnetic fields and themselves subjected to diffusive effects.

In this formulation, while inertial and finite gyroradius effects (arising from off-diagonal terms in the pressure tensor) are central to energy diffusion in the EDR [Vasyliunas, 1975], Hall electric fields and currents have a significant role to play at ion scales. The charge separation caused by electrons continuing to convect towards the reconnecting current sheet after ions begin their meandering motion gives rise to the Hall electric field pointing towards the current sheet (red arrows in Figure 1.6) as well as Hall currents in the same direction. A charge conservation argument implies these Hall currents will also flow in along the boundary between stable and reconnecting magnetic field lines (topologically referred to as the

separatrix; dotted lines in Figure 1.6) as well as out along the current sheet towards the outflow region [Sonnerup, 1979]. The circulating Hall currents will then generate magnetic fields pointing into or out-of the plane we have considered so far (the y-direction in Figure 1.6) forming a quadrupolar system of Hall magnetic fields (represented by circled crosses and dots in Figure 1.6). In this way the Hall fields and currents dominate the ion behavior in the IDR and strongly influence the overall size and organization of the reconnection region in general. This is the basic picture of Hall reconnection.

It was of interest to me to discover on preparing this introduction that Dungey had proposed a very similar two-fluid approach far earlier than was noted by either Vasyliunas or Sonnerup. In a small textbook published in 1958 [Dungey, 1958] Dungey describes the methods and consequences of magnetic null point formation in astrophysical situations, makes a case for MHD to be an insufficient paradigm for describing the plasma near such magnetic nulls, and summarizes a kinetic theory of plasma utilizing a modified Boltzmann equation (easily recognized as the Vlasov equation, neglecting collisional effects). He also derives a generalized Ohm's law for both a single-species plasma which is nearly identical to the derivation above (a great comfort to me after deriving it separately) as well as for a two-species plasma with both electrons and fully-ionized hydrogen (*i.e.* protons). While admitting that he did not immediately see an application for the Hall term in the interactions under his immediate consideration, he does include it in his discussion of the theoretical behavior of magnetic field lines detaching and rejoining near an X-line magnetic null, as well as some discussion of inertial and pressure-related effects. His arguments are fundamentally the same as those made by Vasyliunas and Sonnerup 20 years later and are limited in their conclusions only by the total lack of experimental data which later authors had at their disposal.

Significant questions still remained after the milestone summaries of Vasyliunas (1975) and Sonnerup (1979) regarding the exact mechanism for energy diffusion as well as how a thin current sheet between anti-parallel magnetic fields could transition to a reconnecting current

sheet and vice-versa. Theorists continued to hypothesize and build models for possible onset mechanisms and drivers of reconnection (*e.g.* [BÜCHNER, 1991, Mandt et al., 1994]). However, the overall structure of the neighborhood surrounding a reconnecting current sheet was laid out. What was needed now was data to support it.

1.5 Seeing Signs of Reconnection

The size of the IDR surrounding a reconnecting current sheet, as mentioned above, is on the scale of an ion gyroradius ($\approx 200-2000km$ in active tail regions) embedded in the tail neutral sheet which is more than $2.5e5km$ wide and $1e6km$ long. While it is certainly possible that more than one site of reconnection may be active at a time, this is still reasonably akin to the proverbial needle in a haystack. It is no wonder that the bulk of observational evidence of reconnection in the tail from the 1960s through the 1990s occurred in the form of high-speed flows in compressed regions of the neutral sheet during times of particular geomagnetic activity (*e.g.* [Forbes et al., 1981, Hones, 1985] and references therein).

In the absence of detailed *in situ* tail observations, the rapidly expanding field of computer simulations helped to explore some of the instabilities and boundary conditions necessary to further develop the theory. Some (*e.g.* [Birn, 1980]) visualized the scales, both spatial and temporal, over which the tail current sheet thinning could be expected to extend during geomagnetic substorms. The theoretical work up through Sonnerup (1979) was primarily focused on steady-state reconnection, without considering any explicit mechanism for starting or stopping. Early simulations combined with ground observations of magnetic fluctuations during substorms (*e.g.* [Singer et al., 1988] and references therein) to bound the time scale of tail reconnection and show that it waxed and waned with changes in the IMF and other external driving conditions.

The search for magnetic reconnection in the dayside magnetosphere during this time had much better success. Similarly, observations of time-dependant reconnection in the

form of Flux Transfer Events (FTEs) were observed in several locations across the dayside magnetopause [Russell and Elphic, 1978]. These transient, unsteady, and highly-localized events differ from the classic picture of dayside reconnection that might be expected from Figure 1.2 in that they are not an interaction between the Earth's magnetosphere and the gross IMF magnetic field. Instead FTEs are understood to be magnetic reconnection between the Earth's magnetopause and a discrete, twisted, tube of magnetic field lines (often referred to as a flux tube or flux rope) coming from the Sun. While not consistent with the steady-state reconnection initially assumed by Dungey, they occur frequently, with approximately 1 FTE forming every 10 minutes or so [Farrugia et al., 1988], thus contributing to the overall magnetic erosion on the dayside and the overall Dungey cycle.

In terms of steady-state reconnection, the ISEE 1 and 2 satellites [Ogilvie et al., 1977] observed several rotational discontinuities in the magnetic field at the dayside magnetopause (the interface between the Earth's magnetic field and the IMF) coupled with strong plasma flows in the north-south direction consistent with the outflows of magnetic reconnection on the dayside [Sonnerup et al., 1981]. The electric field at the dayside magnetopause was also measured and found to have a component in the dawn-dusk direction during periods of strong southward IMF (*i.e.* $B_z < 0$ outside the Earth's magnetosphere while $B_z > 0$ inside) [Mozer et al., 1979]. This is consistent with the picture of magnetic reconnection in Figure 1.6 oriented such that the top of Figure 1.6 is in the IMF, the bottom is in the Earth's magnetosphere, and the X-axis of the Figure is roughly in the north-south direction. The dawn-dusk electric field would then be equivalent to an electric field pointing into the figure (*i.e.* out of the plane of the figure), and would be the sum of out-of-plane components of Equation (1.1). While not conclusive separately, these observations combined to greatly enhance the credibility of magnetic reconnection as the dayside engine of the Dungey cycle.

With increasing numbers of simultaneous orbiting observatories as well as the continuing improvement of instrument resolution, observational evidence could now cement the

geomagnetic and auroral substorm as intrinsically connected with magnetic reconnection in the tail ([Russell and McPherron, 1973, Hones, 1979, Forbes et al., 1981, Nagai et al., 1998, Baumjohann et al., 2000], etc.).

1.5.1 Eureka

The first definitive encounter with a reconnection ion diffusion region in the geomagnetic tail was reported by Øieroset et al. (2001). On the first of April, 1999 the *Wind* spacecraft [Acuna et al., 1995, Wilson et al., 2021] was traversing the tail plasma sheet at approximately $(-56, -9.5, 6.6)R_E$ in GSE coordinates, placing it just after local midnight, slightly north of the ecliptic, and nearly the distance of lunar orbit. At a current sheet encounter, characterized by the reversal of the X_{GSE} component of the magnetic field, WIND detected a reversal of the bulk plasma flow from toward the Earth ($+V_X$ in GSE coordinates) to tailward away from the Earth ($-V_X$ in GSE coordinates), each with a speed of several hundreds of kilometers per second. The plasma velocity reversal was correlated with a similar reversal in the sign of the Z_{GSE} component of the magnetic field, indicating a change from magnetic field lines connected to the Earth to those connected to the solar wind. Also observed was an orderly reversal of the Y_{GSE} component of the magnetic field which corresponded well with the expected values of the Hall magnetic field (Figure 1.7).

Nagai et al. (2001) strengthened the case for tail reconnection by examining the plasma distribution functions near tail central plasma sheet encounters. Using data from Geotail [Nishida, 1994], they identified several instances of strong, simultaneous ion and electron heating and acceleration near the central current sheet, matching the expectation of the plasma outflow region near the X-line (V_{out} in Figure 1.6). Counter-streaming low-energy electrons flowing towards a presumed reconnecting X-line were also observed in these instances, alongside the accelerated and heated outflow, which is consistent with the Hall currents required by charge conservation. When these particle observations are combined

with the clear measurements of the Hall magnetic field structure by Øieroset et al., the Hall reconnection picture of the IDR surrounding a reconnecting X-line in the geomagnetic tail became all but certain.

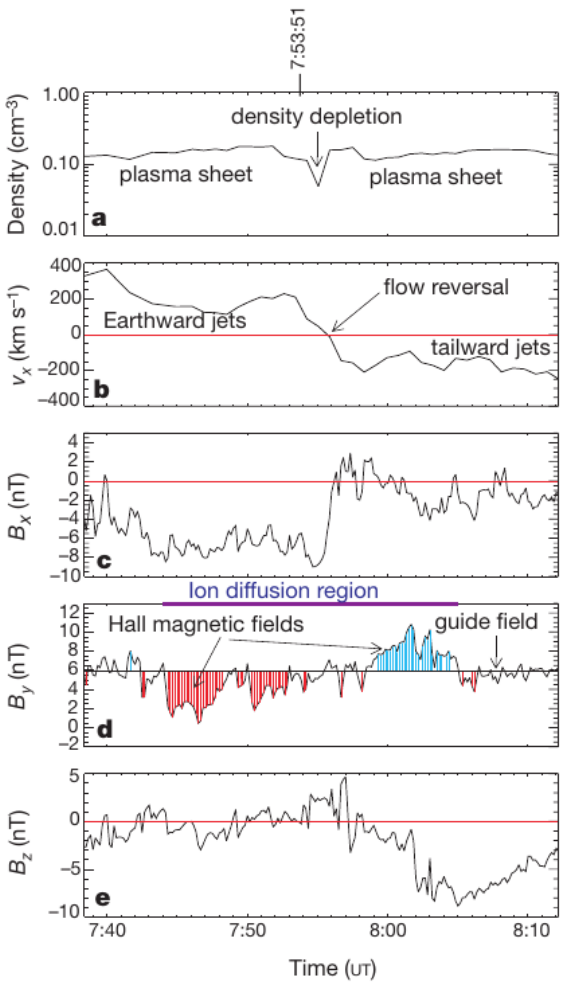

Figure 1.7: Figure 2 from [Øieroset et al., 2001] showing the outflow jets and Hall magnetic field signatures of Hall reconnection.

Between scattered examples of reconnection at the magnetopause and now direct observations of reconnection in the magnetotail, the case in favor of Dungey's picture of global magnetosphere magnetic flux convection from dayside to nightside and back around again by way of reconnecting field lines had received undeniable support. However there still remained huge questions as to the inner workings of magnetic reconnection itself. While Hall

currents and magnetic fields had been observed [Øieroset et al., 2000, 2001, Nagai et al., 2001], the Hall electric field, ostensibly the driver for the current and magnetic fields, still had not been reported; the EDR had still not been directly observed; and the question of reconnection onset, how the tail current sheet transitioned from a compressed but quiet state to reconnection, still perplexed. Looking for answers to these questions with single platforms, the observations from which were not well-coordinated and depended entirely on fortuitous conjunctions (*e.g.* [Singer et al., 1988]), had proven to be comparable to a mouse searching for a needle in the haystack. Farrugia et al. (1988) summarized this difficulty in *in situ* magnetic reconnection studies: "For the future we conclude the strong need for spatially well-separated multipoint observations."

1.6 Multi-point era

What was needed was to have a fleet of orbiting observatories, flying in a regular formation, each possessing the means to measure the magnetic and electric fields as well as the full plasma distribution functions of both ions and electrons. Such a distributed observing platform would allow for simultaneously looking at several individual locations for the signs of reconnection and for providing context from the surrounding region if such signs were found. This ambition was realized in the Cluster mission [Escoubet et al., 2001].

Consisting of four (ideally) identical observatories and flying in a nominal tetrahedron or pyramid formation, Cluster was well-provisioned for seeking out the signs of reconnection. The separation between spacecraft and the time resolution of the instruments on board were all designed to be of a scale necessary to clearly observe ion-scale effects. Its goal was to find and study Ion Diffusion Regions and thus characterize the ion-related aspects of reconnection. This laudable goal was somewhat hampered by mishap; the initial attempt to launch the cluster mission failed when the rocket carrying it exploded before reaching orbit in 1996. The European Space Agency (ESA) which had been leading the Cluster mission refused

to let the idea die, however, and rebuilt the four satellites needed, often using the flight spare hardware from the development process [Hellemans, 1996]. These, dubbed Cluster-II, launched successfully into a near-polar orbit in the summer of 2000.

1.6.1 The Ion Diffusion Region

Roughly a year after Cluster was launched, it demonstrated the values of coordinated multi-point observations. Runov et al. (2003) report that on the first of October, 2001 Cluster made several encounters with the central neutral sheet in the pre-midnight local time sector, all within a reasonably short amount of time [Runov et al., 2003]. The separation between spacecraft in the formation was at the upper end of the ion scales ($\approx 2000km$), which also allowed the fleet to simultaneously sample different parts of active current sheet. A strong tailward plasma flow, coupled with a southward-pointing magnetic field was followed by an even larger Earthward plasma flow coupled with a northward magnetic field, the reversals in each parameter happening nearly simultaneously. Lower-velocity plasma flows coming from the northern and southern lobes were also seen in between the peaks in tailward and Earthward flows. The Y_{GSM} component of the magnetic field as measured by all four spacecraft also showed all four quadrants of the expected Hall magnetic field. All of the expected components of Hall reconnection, excepting the Hall electric field, are clearly observed.

The regularly distributed magnetic field measurements allowed for even more subtle exploration. The regular tetrahedron formation of the observatories allows for a good estimation of the gradient of the magnetic field $\nabla\vec{B}$ at the center of the tetrahedron. From this the more common spatial derivatives of the vector magnetic field (the curl $\nabla \times \vec{B}$, and the divergence $\nabla \cdot \vec{B}$) can also be derived. By exploiting Ampere's law ($\nabla \times \vec{B} = \mu_0\vec{j}$, one of Maxwell's equations of electromagnetism) the current density $\vec{j}$ can be measured at the center of the tetrahedron formation. While current measurements using plasma instruments had been reported previously to this, the magnetic field instruments on board Cluster were

of much higher time resolution than any of the plasma instruments up to that time, and the precision of the magnetic field measurements allowed for a much more precise measurement of the current density than had been possible before. This permitted the analysis of the currents in the region surrounding the reconnecting X-line to be analyzed with the same level of detail as the magnetic field measurements themselves [Runov et al., 2003].

The $\nabla\vec{B}$ estimation available to the Cluster mission also allowed for calculating the magnetic field curvature $\vec{b}\cdot\nabla\vec{b}$ (where $\vec{b}=\vec{B}/|B|$)at the center of the tetrahedron. With this tool, the shape of the magnetic fields could be measured at the center of the formation. [Runov et al., 2003] used this tool to show that the magnetic field was tightly compressed in the Z_{GSM} direction, causing the tightest curvature to be in the X_{GSM} direction, and that the X-curvature pointed in the same direction as the plasma outflows from the X-line (Figure 1.8).

A statistical study of high-speed flows near the neutral sheet [Runov et al., 2005] by Cluster in the tail provided strong evidence of correlation between the direction of plasma flows either toward or away from the Earth and the direction of the strongest magnetic field curvature. Cluster observations also provided a laboratory with which to explore theories regarding the relationship between the measured geometry of the magnetic field near the tail neutral sheet and the overall structure of the neutral sheet [Rong et al., 2010]. Further statistical observations of a variety of thick and thin tail neutral sheets by Cluster supported these theories and provided a clear picture of the structure of the near-tail neutral sheet [Shen et al., 2008, Rong et al., 2011]; a structure revisited in Chapter 4.

Magnetic reconnection was not left out of the statistical studies possible with Cluster data. [Eastwood et al., 2010] identified a collection of 33 instances where Cluster encountered correlated plasma V_x and magnetic field B_z reversals in the geomagnetic tail; of which 18 showed Hall electric and magnetic field signatures consistent with reconnection. This collection represented at least a third of all the IDR candidate events which had been re-

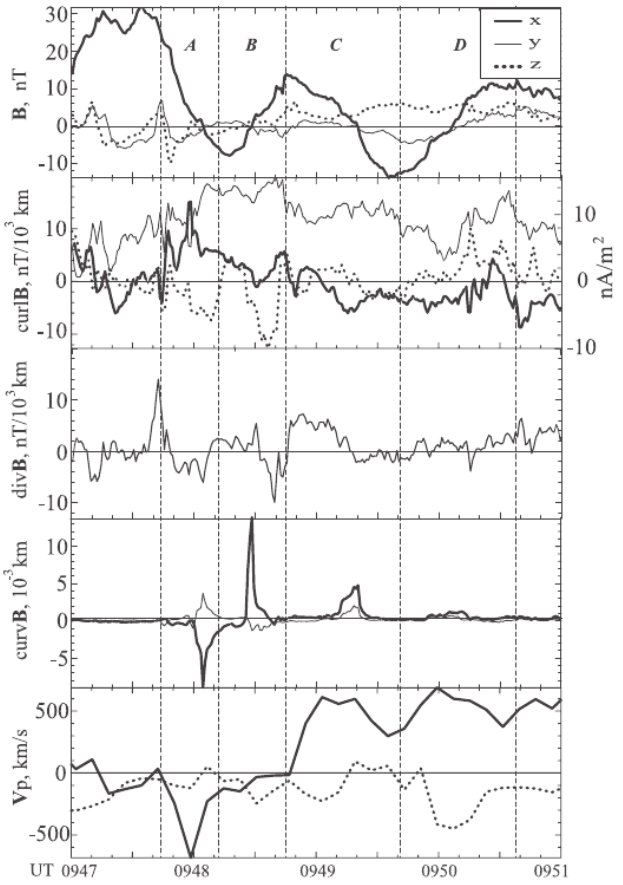

Figure 1.8: Figure 2 from [Runov et al., 2003] showing some of the $\nabla \vec{B}$ parameters calculated from the magnetometer measurements from the four spacecraft of Cluster. Note the strongly negative X_{GSM} curvature of the magnetic field correlated with the strongly negative V_X of the protons. This is discussed at more depth in the text.

ported in the tail by Cluster and other missions such as Wind (*e.g.*[Øieroset et al., 2001]) and Geotail (*e.g.*[Nagai et al., 2005]) to that point. In addition to expanding the number of observed reconnection events, Eastwood et al. also performed a statistical analysis of the magnitudes and prevalence of Hall electric and magnetic fields (Figure 1.9). This work served to confirm Hall reconnection as the preeminent model for magnetic reconnection in the geomagnetic tail.

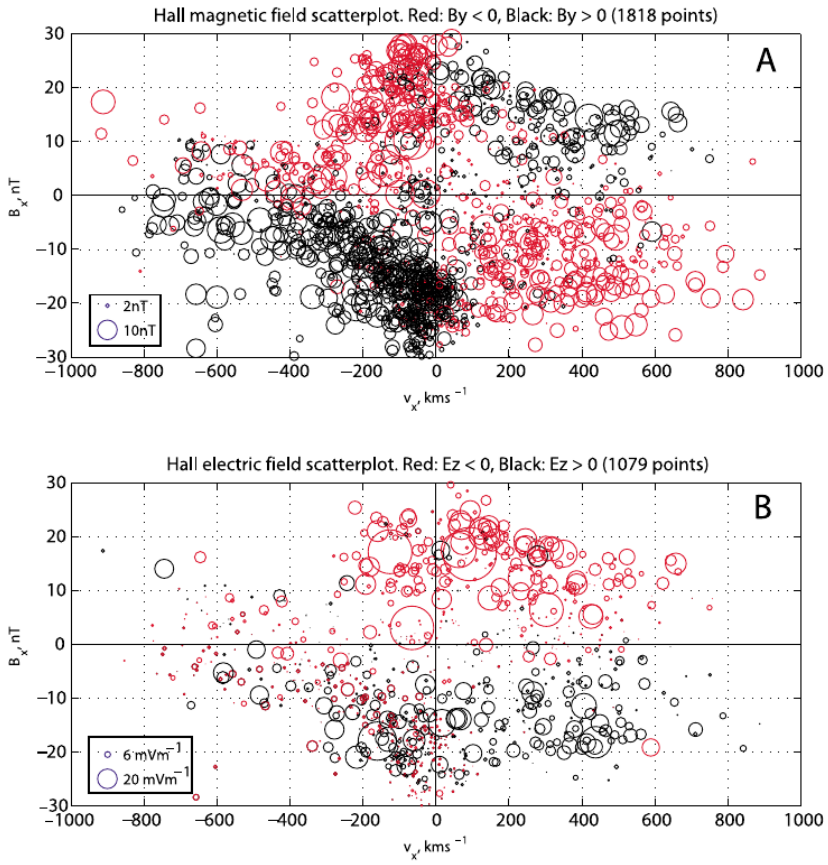

Figure 1.9: Figure 6 from [Eastwood et al., 2010] showing the accumulated measurements of the Hall magnetic (**A**) and electric (**B**) fields. This shows the clear quadrupolar nature of the Hall magnetic fields as well as the bipolar nature of the Hall electric fields.

1.6.2 The MMS Era

Observations using Cluster, and the work of Eastwood et al. [2010] in particular, had solidified the general picture and ion-scale structure of magnetic reconnection in the tail, but many of the same questions which had perplexed for decades remained: How was reconnection initiated? What was the mechanism by which energy was dissipated/converted to heat within the plasma? What regulated the rate of energy conversion? What was the electron-scale structure of the central EDR within the IDR? What influence, if any, did the location of the reconnection region have on its internal parameters?

In order to address these questions additional measurements were required at even higher time resolution and far smaller length scales than Cluster was capable of. At the same time, the power of multi-point formation measurements had been very clearly demonstrated. Not only was an observatory carrying a new generation of instruments needed, at least four of them were required in order to even attempt to answer the questions above. For all of these reasons, NASA developed the Magnetospheric Multi-Scale (MMS) mission [Burch et al., 2016a].

The MMS mission observatories, identified (not very imaginatively) as MMS1–4, each carry a high resolution magnetometer capable of measuring the full direction and magnitude of the magnetic field more than 100 times per second and a set of 6 electric field potential probes to measure the full 3D electric field at the same cadence [Torbert et al., 2016]. In addition, each observatory carries plasma detectors capable of measuring the full electron velocity distribution function (how many particles at what speeds from what directions) every 30ms and the full ion velocity distribution function every 150ms [Pollock et al., 2016]. Also aboard each is an ion spectrometer to determine ion species (*e.g.* hydrogen, helium, oxygen, etc.) as well as high-energy plasma detectors to measure the numbers and energies of particles moving far faster than the bulk of the plasma population [Mauk et al., 2016].

This is by no means a comprehensive list of the instruments on each platform of the MMS mission, but it does summarize those which this work primarily utilizes.

These tools were put to good work almost immediately. Soon after its launch in 2015 the MMS fleet encountered magnetic reconnection at the dayside magnetopause [Burch et al., 2016b]. Utilizing the previously unavailable time resolution measurements of all parameter the demagnetization, heating, and acceleration of electrons at the heart of the EDR was directly measured for the first time. A little more than a year later MMS encountered another EDR, this time in the tail neutral sheet [Torbert et al., 2018]. Here many of the observations of the dayside EDR were confirmed and differences due to the upper and lower inflow regions in the tail being (nearly enough) identically symmetric were also seen (*i.e.* multiple instances of electron acceleration by the reconnection electric field and the minimal influence of turbulence observed).

At last, the smallest scales of reconnection could be observed. However, these were only two examples across decades of theory and conjecture. While these examples were undeniably helpful for informing models and testing specific points, they do not address the question of reconnection onset. Nor do they, in themselves, explain why reconnection and other substorm-related effects have been observed primarily in a narrow wedge of the magnetosphere between 21–24hrs Magnetic Local Time (MLT). A larger library of observations was needed, across many varying initial conditions and contextual situations.

This is where I came in.

CHAPTER 2

Algorithmic Identification of IDRs Using MMS

2.1 Introduction

In situ observations of reconnection in the Earth's magnetotail have been made with several missions since 1999 (*e.g.* [Øieroset et al., 2001, Runov et al., 2003, Nagai et al., 2005, Eastwood et al., 2010]). All of the associated IDRs have been identified by visual inspection of the data products by a human researcher. These identifications and observations have been invaluable in confirming Hall reconnection as the dominant paradigm of ion behavior near a magnetic neutral point in the geomagnetic tail. The typical approach to such visual identification depends on the observation of correlated reversals of the Sun-Earth component ($\hat{x}$) of the plasma flow velocity and the north-south component ($\hat{z}$) of the magnetic field in the appropriate coordinate system (*e.g.* Geocentric Solar Magnetospheric (GSM), Geocentric Solar Ecliptic (GSE), etc.) This assumes that the Earthward flows of plasma (in the $+\hat{x}$ direction) are associated with the northward-pointing ($+\hat{z}$ direction) terrestrial magnetic field, *i.e.* 'closed' magnetic field lines, while the tailward plasma ($-\hat{x}$ direction) are associated with southward ($-\hat{z}$) or 'open' magnetic field lines connected to the IMF and the solar wind. A correlated reversal, *i.e.* $+V_x, +B_z \rightarrow -V_x, -B_z$ or vice versa, would then suggest that a reconnecting magnetic null (or X-line) had moved across the observer.

This observation alone, however, is not quite sufficient. Flow reversals with weak or indeterminate B_z correlation have been observed which in no other way indicate magnetic reconnection [Nagai et al., 2013, Shinohara et al., 2016]. One method to confirm a correlated

field and flow reversal is an IDR and not a non-active flow reversal (NAFR) is to check for the presence of Hall electric and magnetic fields in the neighborhood of the correlated reversal. As described in the introduction (see Section 1.4), Hall fields arise when the heavier ions with their larger gyroradii become demagnetized further from the reconnecting current sheet than their much lighter electron counterparts. The resulting differential motion of charges results in an electric field pointing towards the current sheet, currents to maintain charge conservation, and magnetic fields arising from those currents. However, the tail current sheet frequently is compressed sufficiently to partial demagnetize ions located near it, leading to widespread Hall electric and magnetic fields even in the absence of any local reconnection [Lu et al., 2019].

In a survey of IDRs identified using Cluster data Eastwood et al. (2010) suggest that the magnitude of the electric field $|\vec{E}|$ "may be a useful tool for automatically identifying encounters with the diffusion region in the data." They note that the magnitude of the total DC electric field often reaches several 10s of mV/m, far in excess of that found in the typical quiet neutral sheet. While strong electric field magnitudes are also expected for other dynamic magnetosphere events such as dipolarization fronts ([Fu et al., 2020] and references therein), the combination of all of the above criteria results in a much more selective, and arguably more reliable, identification.

This is essentially the process used by Eastwood et al. (2010) to identify IDRs in Cluster data, leading to impressive statistical analysis within the resolution of Cluster instruments. However, even this high standard has its weak point. The growing list of criteria which must be satisfied creates mounting complexity in the decision-making process of the human researcher applying them. A certain degree of subjectivity will always be included in any identification made this way, regardless of the best intentions of the researcher. One example of this is the potentially arbitrary weight given to selection criteria during examination; another is the possibility that the researcher is distracted or mistaken while viewing a potential

candidate diffusion region.

In an effort to mitigate these sources of subjectivity, and understanding the impossibility of eliminating them, I developed an algorithm in the form of sequential Boolean statements and implemented as an IDL procedure utilizing the SPEDAS library of data analysis tools and utilities[Angelopoulos et al., 2019]. The algorithm applies a total of five tests in sequential stages for each 3-minute interval of MMS observations in the geomagnetic tail. If all five criteria are satisfied in order then the 3-minute data segment is marked for human review as a possible IDR.

2.2 Methodology and Procedure

Data collected by the MMS fleet of spacecraft during the tail phases of 2017–2020 were analyzed. During this time the apogee of the spacecraft orbits reached a typical distance of ~ 25 Earth radii (R_E) during the 2017 and 2018 tail phases and $\sim 29R_E$ during the 2019 and 2020 tail phases. Coverage of the tail during this time was very good (see Figure 2.1). The MMS mission orbits with a small inclination, meaning that it spends a significant portion of each orbit in or near the tail central plasma sheet, compared to that of Cluster which has a nearly polar orbit, meaning it crosses through the central plasma sheet along a line roughly perpendicular to the neutral sheet at its apogee of $\sim 20R_E$. This allows MMS to sample a much larger portion of the near-tail environment than Cluster is able to do.

In order to limit the search to the central plasma sheet of the magnetotail, we adopt a criterion based on plasma particle density, requiring $n_i > 0.05cm^3$ as this has been statistically found to be the minimum density of the tail plasma sheet[Baumjohann, 1993, Raj et al., 2002]. Only time segments which meet this minimum condition are considered for further analysis of the algorithm. Dwell times in the tail plasma sheet are indicated by color scale in Figure 2.1.

MMS data are analyzed in 3-minute segments with a 1-minute overlap between adjacent

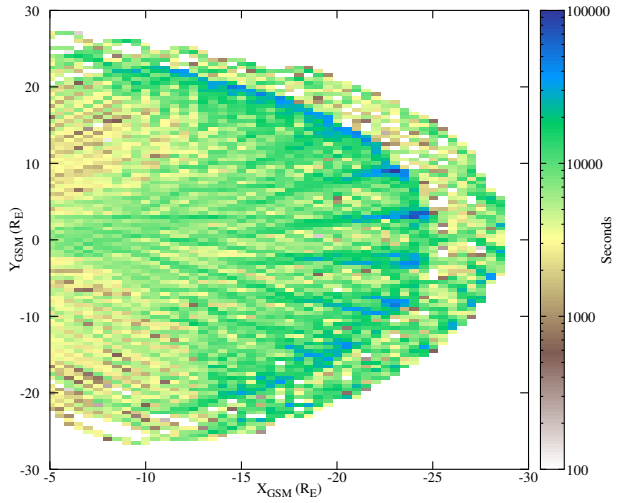

Figure 2.1: Plasma Sheet Dwell Time: The time in seconds (shown by colorbar scale) MMS spent within the tail plasma sheet as determined by plasma number density $n > 0.05cc$ during the 2017–2020 tail seasons.

segments. Each segment determined to be in the plasma sheet by sufficient plasma density is analyzed using a maximum of five search criteria:

i Ion flow reversal in the X_{GSM}, *i.e.* the Earth-Sun, direction

ii Magnetic field reversal in the Z_{GSM} direction

iii Sign correlation of the magnetic field and ion flow reversals

iv Presence of Hall *a)*electric and *b)*magnetic fields

v Significant magnitude of the total DC electric field

These criteria are applied to each 3-minute data segment in sequential stages.

Stage 1 consists of searching for correlated reversals of V_x and B_z within the segment. Flow reversals are further required to be of at least $200km/s$ in magnitude and B_z reversals are required to be of at least $2nT$ in magnitude, centered about 0. Correlation of these

reversals is determined by requiring that V_x should turn from positive (negative) to negative (positive) within $90s$ of B_z turning from positive (negative) to negative (positive). Segments which satisfy these criteria are then analyzed using the criteria for Stage 2. Figure 2.2 shows an example of a segment which passes the Stage 1 criteria where B_z and V_x are represented by red and blue traces, respectively. During the 2 minutes shown the ion flow (blue trace) changes from $V_x < -400$ to $\sim +200km/s$ (*i.e* from tailward to Earthward) and, at practically the same time, B_z (red trace) changes from $-7 \rightarrow +4nT$ (*i.e.* from southward to northward pointing). This is consistent with an X-line passing over the MMS observatory and moving tailward [Øieroset et al., 2001, Runov et al., 2003, Borg et al., 2005].

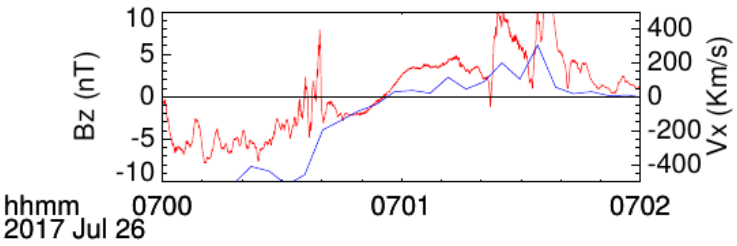

Figure 2.2: Components of the ion velocity moment and magnetic field measured by MMS1 on 26 July, 2017. The correlated reversal of the ion velocity in the X_{GSM} direction (blue) and the normal (Z_{GSM}) component of the magnetic field (red) as observed by MMS1. Given the small separation in time between the velocity and magnetic field reversals and the magnitudes of each both before and after the reversals, this example satisfies the algorithmic requirements for Stage 1.

Stage 2 consists of a search for Hall electric and magnetic fields within the segment. Hall electric fields are determined by measuring the $\hat{z}$ component of the electric field with a magnitude $\geq 3mV/m$ sign anti-correlated with the $\hat{x}$ component of the magnetic field, both in GSM coordinates. This would correspond to a southward-pointing electric field ($E_z < 0$) while north of the magnetotail neutral sheet ($B_x > 0$) and vice versa, with the result being that the Hall electric field points towards the center of the neutral sheet and the reconnecting current sheet assumed to be located there. The bottom panel of Figure 2.3 shows the B_x (blue trace) and E_z (red trace) values for the same time period as in Figure

2.2. B_x is negative throughout, indicating the spacecraft is south of the center of the current sheet. Except for brief excursions, E_z remains positive; thus it is directed toward the central current sheet as expected from the Hall electric field (see Figure 1.6 in section 1.4).

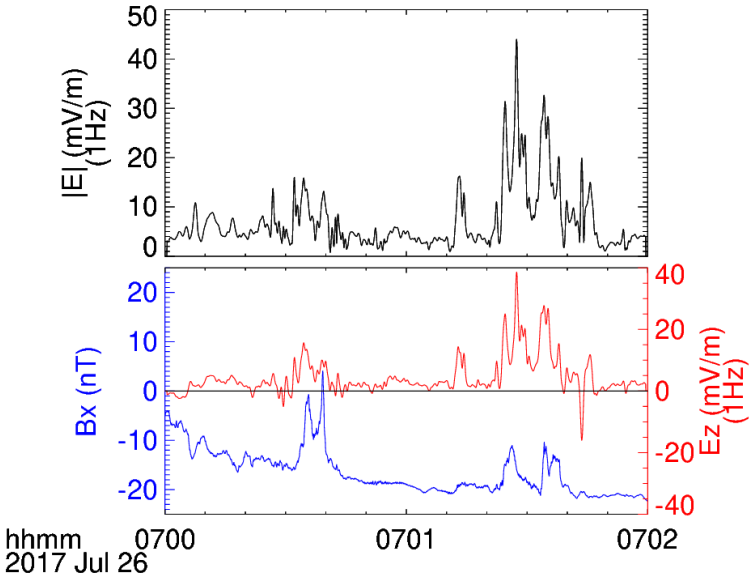

Figure 2.3: Components of the electric and magnetic fields measured by MMS1 on 26 July, 2017. The magnitude of the electric field (top panel) is strong in the neighborhood (within 40s) of the correlated magnetic field and flow reversals as shown above. We also note the strong Z_{GSM} electric field (in red, bottom panel) which is sign anti-correlated with the X_{GSM} magnetic field component (in blue, bottom panel) which suggests the presence of the Hall electric field.

The second part of Stage 2, identifying Hall magnetic fields, is performed by measuring the Y_{GSM} component of the magnetic field where $B_y > 1nT$ and with sign equal to sign$(B_x)\times$ sign(V_x). This sign requirement has the effect of dividing the IDR into four regions (marked with Roman numerals **I**–**IV** in Figure 1.6) within a proxy coordinate system where V_x maps to the abscissa or $\hat{x}$–axis values and B_x maps to the ordinate or $\hat{y}$–axis values. Region **I** is then characterized by positive values for both V_x and B_x; region **II** is where V_x is negative but B_x is positive; region **III** is where both V_x and B_x are negative; and region **IV** is where V_x is positive while B_x is negative. In order to conform to the predicted topology of Hall magnetic fields, B_y should be positive in regions **I** and **III** and negative in regions **II** and

IV. This is the origin of the so-called 'quadrupolar' signature of Hall out-of-plane magnetic fields [Dungey, 1958, Sonnerup, 1979].

Spacecraft motion relative to the reconnecting X-line does not always allow the observatory (or observatories) to sample all four quadrants of the Hall IDR picture. Therefore at least two of the four quadrants implied by the proxy coordinate system outlined above must be populated with B_y measurements taken during the segment and of the correct sign and minimum magnitude to be accepted as indicating the presence of Hall magnetic fields. Figure 2.4 illustrates this during the same event as in Figures 2.2 and 2.3. As indicated by Figure 2.3 the spacecraft are sampling B_y south of the neutral sheet (negative B_x). Tailward of the presumed X-line ($V_x < 0$) the B_y is positive (blue bubbles) as expected from region **III**, while Earthward of the X-line B_y is negative as is expected in region **IV**. This figure also demonstrates a tendency for the magnitude of the Hall magnetic field to be greater closer to the neutral sheet and the X-line, *i.e.* closer to the origin of the proxy coordinate system.

Stage 3 consists of detection of a strong DC electric field of magnitude $|E| \geq 10mV/m$ in the neighborhood of the correlated B_z and V_x reversal, and after showing good evidence of Hall electric and magnetic fields. To limit the influence of strong electrostatic wave activity in this stage the electric field data are subjected to a low-pass filter with a critical frequency of $1Hz$ prior to analysis. Figure 2.3 shows an example of this during the same event previously referenced. $|\vec{E}|$ (upper graph) reached values greater than $40mV/m$ shortly after the correlated reversals at 0701 UTC, satisfying the Stage 3 criteria. If a 3-minute data segment satisfies this criteria, having satisfied all other criteria as and in the order described, then the segment is considered to contain a candidate IDR.

2.2.1 Algorithm Implementation

The algorithm was implemented via a procedure in the IDL programming language (source code available in a GitHub repository: https://github.com/unh-mms-rogers/IDR_tail_search),

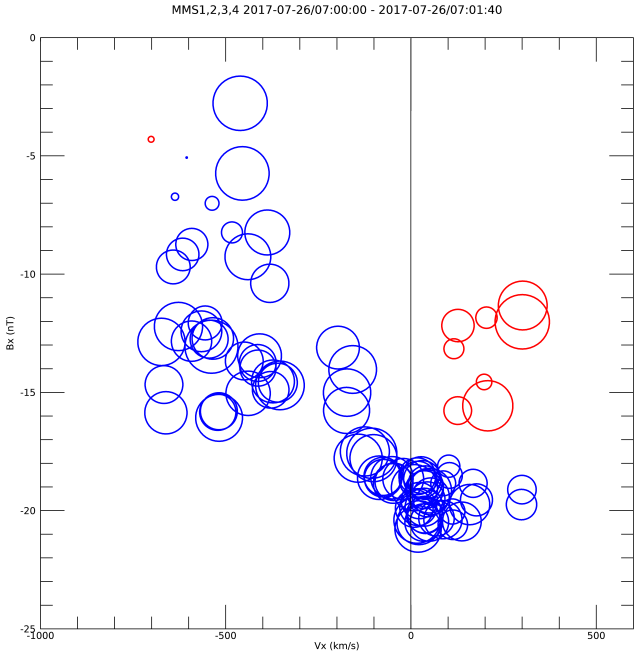

Figure 2.4: Bubbles represent the out-of-plane (Y_{GSM}) component of the magnetic field, where blue circles are positive values and red are negative with area proportional to the square root of the magnitude of $B_y \in [0.1, 5.6]nT$, after [Borg et al., 2005]. The $\hat{x}$ component of the measured ion velocity is the abscissa of the plot, while the ordinate axis is the $\hat{x}$ component of the magnetic field, providing a proxy coordinate system centered on the X-line. Two quadrants of the quadrupolar Hall magnetic field are visible here, with moderate cross-contamination near the $V_i = 0$ point.

leveraging the SPEDAS library [Angelopoulos et al., 2019] for loading and version control of all MMS data files. The procedure check for each of the stages described above by way of conditional Boolean statements applied to each 3-minute segment of time series data from the appropriate instruments, with each segment overlapping the trailing $60s$ of the preceding segment and the leading $60s$ of the following segment. Results are returned in the form of a text file which lists time segments which have passed Stage 1 criteria as well as markers indicating if the segment has also passed Stage 2 and Stage 3. Segments which have passed all three automated stages were then reviewed by myself. The IDRs reported here have passed all three stages as well as my review.

All electric field data were processed using a low-pass digital filter with a critical frequency of $1Hz$ prior to application of the algorithm in order to mitigate the effects of strong electrostatic wave activity during analysis of Stages 2 and 3. FPI measurements of particle moments were used for all reported IDRs and are the default source for particle moments throughout. The implementation of the algorithm automatically falls back on the Hot Plasma Composition Analyzer (HPCA; [Young et al., 2016]) proton moments when FPI moments are not available, although that was not necessary for any of the selected IDRs.

Fast survey data, being of significantly lower temporal cadence than the maximum (Burst mode data) available from MMS, was used throughout this study. Due to telemetry transmission limitations, full-resolution Burst data is only available after being selected for transmission by a designated Scientist In The Loop (SITL) within an orbit or two of being initially observed by MMS. As such, there is an inherent bias in Burst data along the same lines as those outlined above (Section 2.1) but exacerbated by the fact that the SITL is a rotating position filled by a variety of members of the MMS science community. As part of the motivation for this work was to reduce the *a priori* bias included in IDR identification, I elected to use the fast survey data which is available for the bulk of each orbit, despite the lower resolution. (See [Fuselier et al., 2016] for details regarding the differences between fast

survey and burst mode data collection on MMS.)

Hall magnetic fields are identified by quadrant (see Figure 1.6 for quadrant identification). Each B_y data point is checked for the minimum magnitude and correct polarity to satisfy the expected Hall magnetic field parameters in that quadrant, as determined by the V_x and B_x values at that same time step. After checking all B_y data in the 3-minute time segment under analysis, a ratio of data points which satisfy expected Hall parameters to the total number of B_y data points in the segment is calculated. This is compared to a minimum threshold entered as a user-defined parameter at runtime. If the ratio calculated exceeds the threshold provided then the time segment is marked as containing likely Hall magnetic fields. The ratio used for this study was 0.10.

This threshold value was arrived at after studying a reduced sample of previously identified IDRs and considering the amount of B_y data points which did not conform to the expected Hall magnetic field, or 'contamination,' within each quadrant of the time segment as a whole. Requiring an effective threshold ratio of 1.00 proved impractical due to a variety of circumstances such as the IDR and associated Hall fields only occurring during a small fraction of the 3-minute time segment, large-scale motion of the tail current sheet causing MMS to only intermittently encounter the IDR and associated Hall fields, etc. Using the reduced sample set of IDRs, various ratios were tried in an effort to balance correct identification with filtering of obviously non-Hall fields. The resulting ratio of 0.10 was found to functionally eliminate false negatives at this stage of analysis while still significantly reducing the false positives.

Final examination of computer-identified IDR candidates was performed by eye using line plots similar to those shown in Figures 2.5 and 2.7. Human review is focused on checking for clear plasma flow and magnetic field reversals with a minimum of erratic or noisy behavior which may call into question the timing or certainty of the reversals. The electric field in the neighborhood of the reversal is also reviewed to ensure that the maximum is, indeed, near

the reversal and that strong wave activity does not mimic a DC electric field of sufficient size to pass Stage 3 even after the application of the low-pass filter. Hall electric and magnetic fields are reviewed for non-Hall behavior near the field and flow reversal. The Hall magnetic fields are checked for the appropriate quadrupolar signature using bubble plots similar to Figures 2.6 and 2.8 after [Borg et al., 2005].

Non-ideal behavior in any of the three stages can still pass checks in the algorithm as implemented and may represent other geospatial events which are not IDRs (see discussion in Section 2.6). These events are eliminated as IDRs during human review.

2.3 Examples

Below are two case studies to illustrate the mechanism of the algorithm.

2.3.1 Case Study A: 0729 UTC 26 July 2017

Figure 2.5 shows 3 minutes surrounding an IDR as observed by the MMS4 observatory and identified by the algorithm as described in the previous section. This event was previously studied by Ergun et al. (2018) whose emphasis was on the turbulent energy transfer process occurring from 07:21:13 to 07:38:42 UTC. The location of MMS was approximately $(-23.0, 9.94, 2.20)R_E$ in GSM coordinates, or 22.6 MLT at a distance of $24.8R_E$, placing this event in the pre-midnight sector. The FGM data in the top panel show a rapidly changing magnetic field with no fewer than 10 current sheet crossings (identified by reversals in the polarity of B_x) in the period shown. The B_z component also changes sign several times, with a particular reversal of interest from southward to northward at 07:28:46 UTC and marked with a vertical guideline. In the second panel ion speeds up to $400km/s$ are recorded with a transition from tailward to Earthward flow at 07:28:48 UTC. Filtered electric field data in GSM coordinates are shown in the third panel with the fourth and fifth panels dedicated to E_Z and $|\vec{E}|$ respectively. Strong DC electric fields ($\geq 10mV/m$) are measured frequently

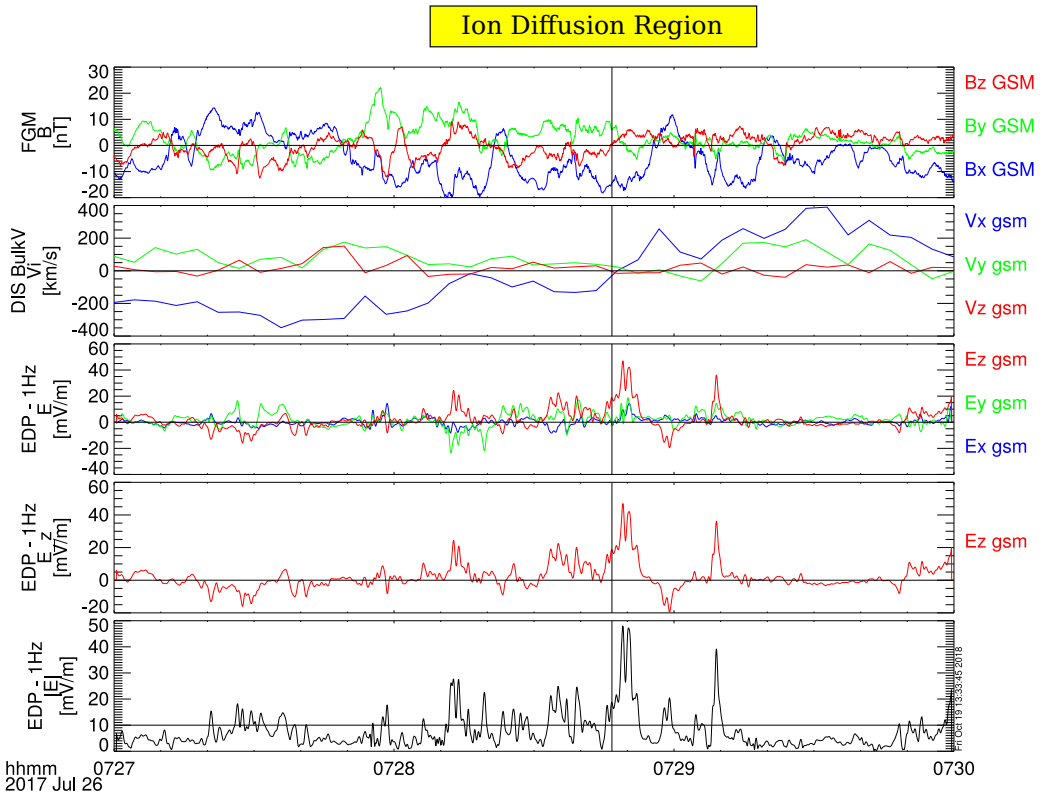

Figure 2.5: A strong reversal in B_z (vertical line) is seen ∼3s before a correlated reversal in V_x. The 30s surrounding these reversals also have strong electric fields, frequently much greater than $20mV/m$. Other regions with strong electric field indicators of reconnection occur both before and after the correlated reversals (07:28:12, 07:30:00). Hall electric fields were also measured in each of these regions and Hall magnetic fields are seen throughout the neighborhood surrounding the reversals. Based on these indicators the time period where the observatory is within the diffusion region is marked by the colored label at the top of the Figure.

during the minute surrounding the correlated field and flow reversal, reaching $\sim 40mV/m$ during the reversal. Comparison of the polarities of B_x and E_z show the expected conditions for Hall electric fields in the region marked with yellow at the top of the figure.

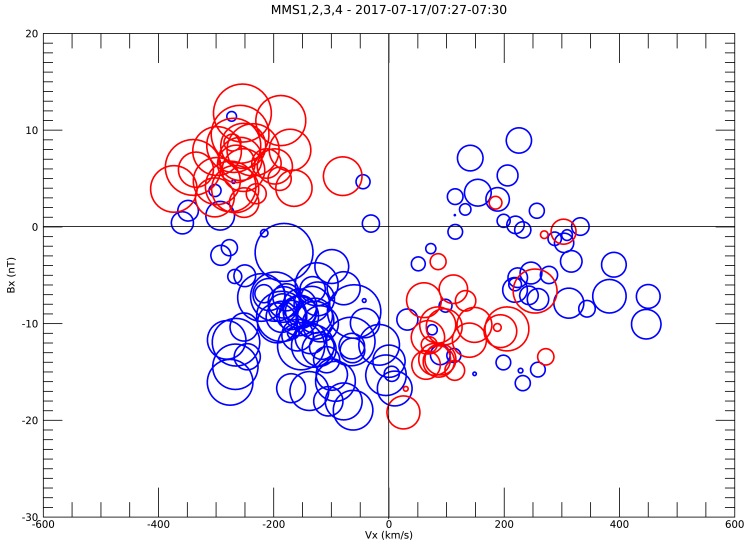

Figure 2.6: In this example all four quadrants of the Hall magnetic field (GSM B_y)are detected by the MMS observatories. The time period of data points used in this plot is the same as for the time series data shown in Figure 2.5. Colors are the same as in Figure 2.4, with the area of each circle again proportional to the square root of the magnitude of B_y.

Figure 2.6 shows the out-of-plane component of the magnetic field (B_y) ordered by the x components of both the magnetic field and ion velocity. Three quadrants of the Hall magnetic field are clearly observed using the combined measurements of all MMS observatories. The out-of-plane magnetic fields are stronger tailward of the reconnecting X-line located at approximately the origin of this figure; a trend typical of events in this study.

2.3.2 Case Study B: 0749 UTC 17 July 2017

Figure 2.7 shows time series data for 3 minutes of observations by the MMS3 observatory roughly centered on an IDR as identified by the algorithm described. The location of MMS

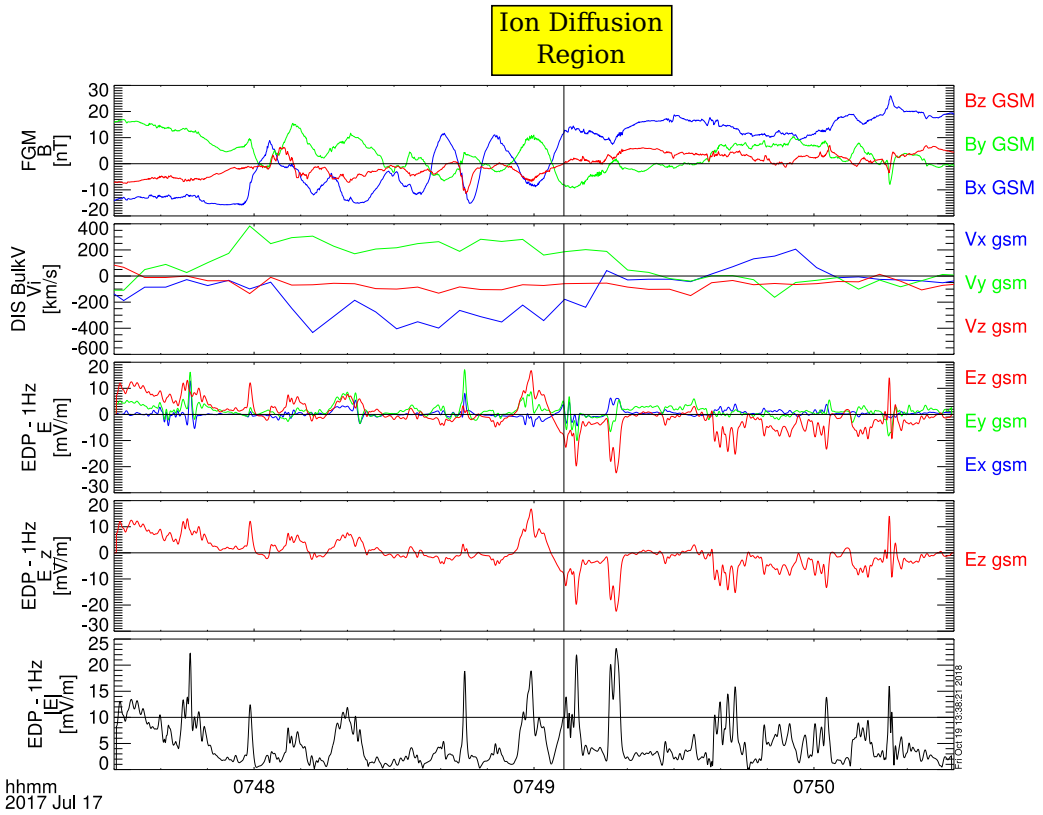

Figure 2.7: A moderate reversal in B_z from $-11nT$ to $6nT$ is the last of a rapid series of neutral sheet crossings, with an associated ion flow reversal approximately 10s later. Moderate to strong Hall electric fields are seen immediately surrounding the reversal.

was $(-18.1, 7.30, 0.66)R_E$ in GSM coordinates, or 22.5 MLT at a distance of $19.5R_E$, in the dusk or pre-midnight sector. The magnetic field data (top panel) shows intense magnetotail flapping as the current sheet moves over the observatory seven times during this period, the final crossing shortly before the zero-crossing of interest in B_z at 07:49:06.4 UTC. Ion velocity data are given in the second panel and show strong tailward flows of $\sim 400km/s$ during the repeated current sheet crossing before reversing to weaker Earthward flows of $\sim 200km/s$ approximately 10s after the correlated B_z reversal. Filtered electric field data are provided showing moderate-strength electric field magnitudes in the neighborhood of and during the minute following the correlated field and flow reversals.

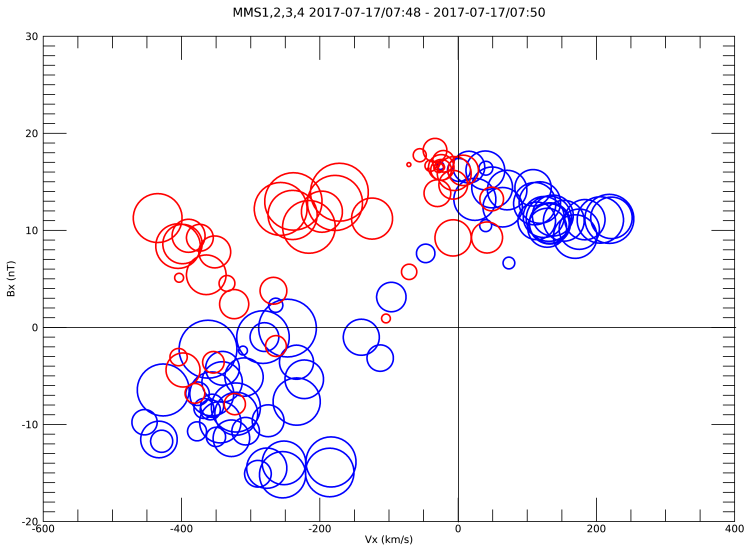

Figure 2.8: In this example, showing the same time period as in Figure 2.7, three quadrants of the Hall magnetic field were observed by the MMS fleet in the minute surrounding the B_z reversal. The organisation of the measured Hall magnetic fields implies a small structure velocity for the X-line and surrounding diffusion region.

Figure 2.8 shows the out-of-plane magnetic field component (B_y) in terms of B_x and V_x where three quadrants of the Hall magnetic field are clearly evident. The significant extension of negative B_y into quadrant I implies there may be a structure velocity to the

X-line relative to the MMS observatories. This would have the effect of moving the origin of the Hall $\vec{B}$ plot along the V_x axis. In this case a structure velocity of $\sim +50 km/s$ can be expected. Using multi-spacecraft timing analysis between the zero-crossings of B_z observed by each MMS observatory a structure velocity in the X_{GSM} direction of $\sim 57.6 km/s$ is calculated. This inference of structure velocity based on the offset origin of Hall $\vec{B}$ plots is similarly borne out by timing analysis for other events.

2.4 Results

Stage Passed	# of events
Stage 1	443
Stage 2	85
Stage 3	42
Confirmed	26

Table 2.1: A table listing the number of events in the 2017–2020 tail seasons which passed each stage of analysis by the algorithm described in the text.

Table 2.1 shows the total number of events which pass each stage of the algorithm described in Section 2.2. Events which pass Stage 1 but not subsequent stages include examples of non-active flow reversals (NAFR), Plasma Sheet Boundary Layer (PSBL) crossings, and other phenomena. Events which also passed Stage 2 but failed to present sufficient $|\vec{E}|$ to pass Stage 3 may include encounters with the inflow region either above or below a reconnecting X-line (see Figure 1.6) without sampling a significant portion of the IDR itself, or may represent other phenomena wherein some portion of the ion population becomes demagnetized, leading to a system of Hall currents.

The 26 IDRs identified by the algorithm and confirmed by human review are listed in Table 2.2. Epochs given in the second column are for the beginning of the ∼3 minute period

Event Label	yyyy-mm-dd/tt:tt UTC	$X_{GSM}(R_E)$	$Y_{GSM}(R_E)$	$Z_{GSM}(R_E)$	$R(R_E)$	MLT
A	2017-05-28/03:57	-19.3	-11.8	0.79	22.6	2.12
B	2017-07-03/05:26	-17.6	3.32	1.75	18.0	23.3
C	2017-07-06/15:34	-24.1	1.41	4.44	24.6	23.8
D	2017-07-06/15:45	-24.2	1.33	4.48	24.6	23.8
E	2017-07-11/22:33	-21.5	4.12	3.78	22.3	23.3
F	2017-07-17/07:48	-18.1	7.30	0.66	19.5	22.5
G	2017-07-26/00:02	-20.6	9.05	3.46	22.8	22.4
H	2017-07-26/07:00	-22.9	8.97	2.28	24.7	22.6
I	2017-07-26/07:27	-23.0	8.94	2.20	24.8	22.6
J	2017-08-06/05:13	-18.9	13.0	0.37	22.9	21.7
K	2017-08-07/15:37	-16.4	4.38	3.77	17.4	23.0
L	2017-08-23/17:53	-18.8	16.1	1.12	24.7	21.2
M	2018-08-15/11:57	-19.2	12.5	1.64	23.0	21.8
N	2018-08-26/06:38	-9.5	12.6	-0.09	15.7	20.5
O	2018-08-27/11:39	-21.1	13.3	0.84	24.9	21.8
P	2018-08-27/12:14	-21.1	3.13	0.97	24.8	21.8
Q	2018-09-10/17:14	-18.2	15.9	1.26	24.2	21.2
R	2018-09-10/23:57	-17.5	12.7	3.10	21.8	21.6
S	2019-07-25/21:40	-24.0	-8.28	4.20	25.7	1.28
T	2019-08-31/12:01	-13.0	13.3	0.44	18.6	20.9
U	2019-09-06/04:38	-22.0	6.55	-0.93	22.9	22.9
V	2020-08-02/16:58	-28.1	-2.71	3.51	28.5	0.39
W	2020-08-02/17:09	-28.1	-2.79	3.46	28.5	0.40
X	2020-08-03/01:04	-27.5	-4.90	1.47	28.0	0.68
Y	2020-08-05/14:19	-25.0	2.98	4.59	25.6	23.5
Z	2020-08-29/09:56	-11.7	11.2	0.92	16.3	21.1

Table 2.2: The 26 Ion Diffusion Regions identified using the algorithm described and confirmed by human review. Included is the start time for the 3 minute time segment where each was identified as well as the location of MMS during that time in both GSM and radial coordinates

which contains the IDR, although some IDRs are observed for greater amounts of time (none more than 6 minutes of MMS data). The positions of each IDR are also given both in Cartesian GSM coordinates and in Magnetic Local Time (MLT) and radial distance from the Earth. This latter system is particularly useful for discussing the distribution of IDRs in the Dawn–Dusk arc (see Chapter 4). Events which passed Stage 3 but were not confirmed as IDRs on review are discussed in Section 2.6.

2.5 Statistical Analysis of Results

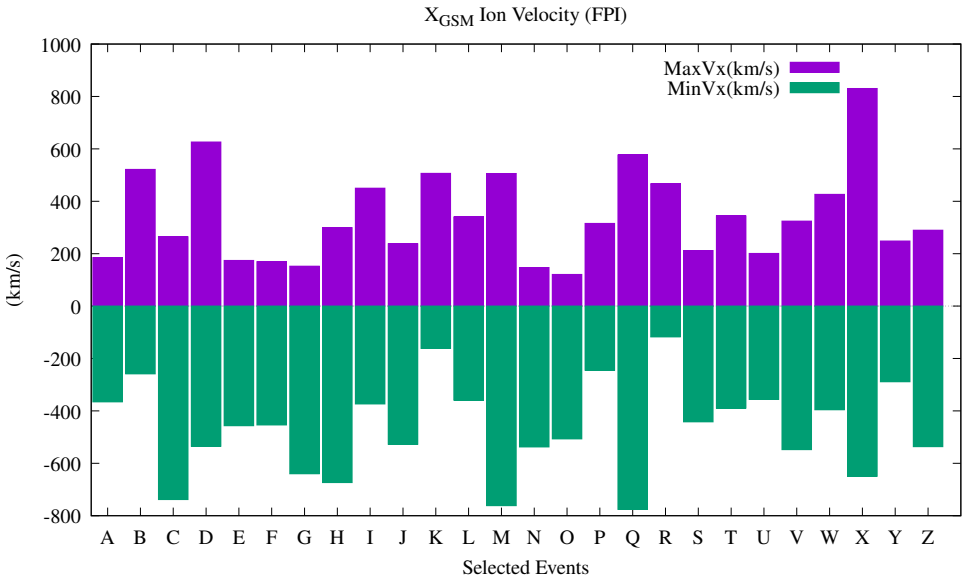

Figure 2.9: The maximum Earthward ($V_x > 0$) and tailward ($V_x < 0$) ion velocities for all of the events listed in Table 2.2. Velocity asymmetries may indicate a structure velocity of the X-line moving Earthward or Tailward (see text)

Maximum positive and negative (*i.e.* highest Earthward and tailward) ion velocities in the X_{GSM} direction for each event are shown in Figure 2.9. These values represent the extrema measured across all four observatories in the MMS fleet during the 3 minute time segments approximately centered on each event. No attempt has been made in these measurements to correct for structure motion relative to MMS; thus asymmetries in the

minimum and maximum may indicate tailward or Earthward motion of the X-line. Any attempt to infer the magnitude of X-line velocity using these asymmetries is hampered by the lack of a reliable coordinate system aligned with the X-line, reconnecting current sheet, and diffusion region in general. While the GSM coordinates are, in general, a reasonable approximation to such a boundary-normal coordinate system, we cannot rely on its accuracy for any particular event (see Genestreti et al. [2018]).

Asymmetries in the component of the magnetic field normal to the reconnecting current sheet (B_z) as shown in Figure 2.10 may also be an artifact of an imperfect coordinate system. Other interpretations include the path of MMS favoring the Earthward ($B_z > 0$) or tailward ($B_z < 0$) side of the X-line during its encounter with the IDR. This argument is reinforced when the average value of B_z during the encounter is on the side of the extrema asymmetry. More subtle explanations are required for events where the average is much smaller than any asymmetry in the extrema values and are beyond the scope of this work.

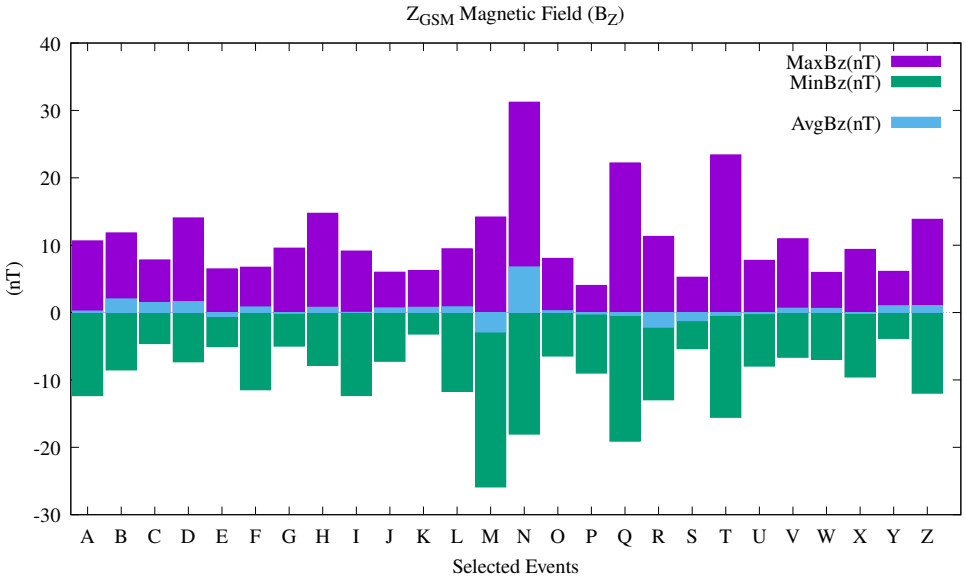

Figure 2.10: The maximum (northward) and minimum (southward) values for B_z in GSM coordinates for each event in Table 2.2

Figure 2.11 shows the maximum and average values of the electric field magnitude during

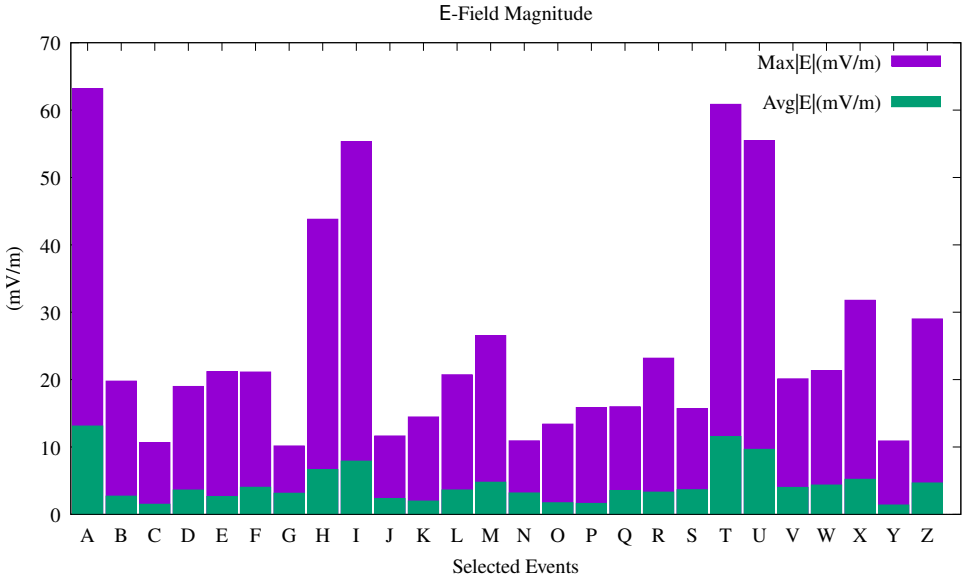

Figure 2.11: Maximum and average DC Electric field magnitude for each of the events listed in Table 2.2. $|\vec{E}| \geq 10mv/m$ in the neighborhood of the V_x/B_z reversal is the requirement to pass Stage 3 of the algorithm described

the 3 minute segment containing each confirmed IDR. As seen in Figures 2.5 and 2.7 the electric field increases significantly in strength when approaching the inner diffusion region, dropping off rapidly as distance increases from the X-line. The broad difference between maximum and average values of $|\vec{E}|$ suggest that strong electric fields exist only very near the thin current sheet with more moderate values elsewhere.

Extrema and average values for both positive and negative E_z are shown in Figure 2.12. Asymmetries in positive versus negative average values are a reasonable proxy for if the observatories spent the majority of each event encounter to the North or South side of the reconnecting current sheet, while similar asymmetries in the extrema values can, by a similar argument to that made for $|E|$, be seen as an indicator of nearest approach to the reconnecting current sheet from the associated side and is well-correlated with the behavior of B_x, a commonly-used proxy for distance to the current sheet. While E_z is used by the algorithm as described as a proxy for the Hall electric field, the accuracy of this assumption

is only as good as the approximation of GSM coordinates to those boundary-normal to the event. As such, analysis could be considered suggestive rather than definitive.

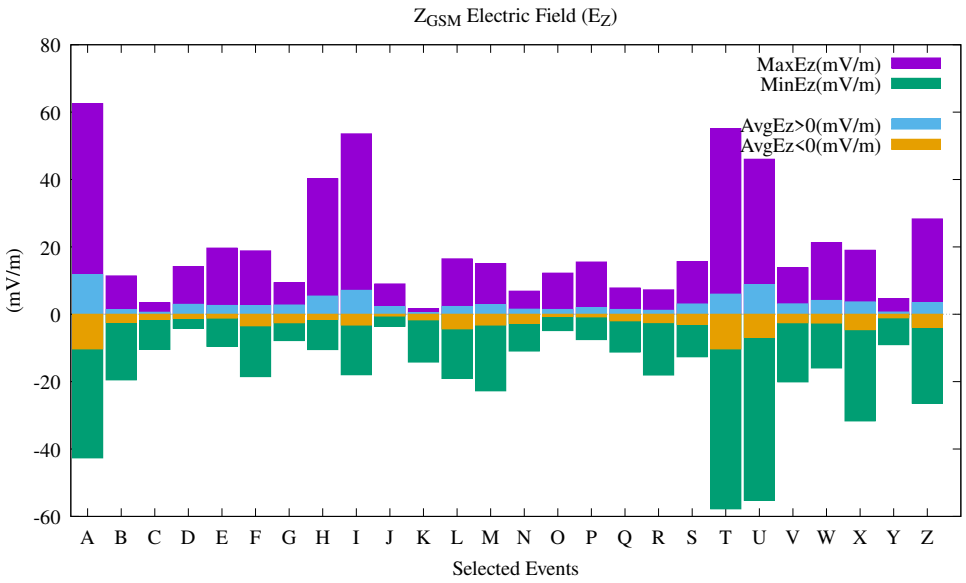

Figure 2.12: Extrema and average values for positive and negative E_z which is used as a proxy for the Hall electric field in this study. Detecting of Hall electric fields (E_z sign anti-correlated with B_x) is part of the requirements for the algorithm's Stage 2

Extreme and average values for all four quadrants of the Hall magnetic field, approximated by B_y and with the same caveats related to coordinate systems which have been mentioned already, are shown in Figure 2.13a and b. The values plotted are those calculated from data across the 3 minute time window containing the confirmed IDR. Again, the approximate nature of the GSM coordinate system relative to the X-line should be kept in mind when interpreting these values. As with the Hall electric field the relative magnitude of the Hall magnetic fields measured in any given quadrant for any given event is dependant to a significant degree on the path of the observatory through the diffusion region. Despite the small separation between spacecraft in the fleet during these mission phases (typically $\sim 15km$) three and sometimes all four quadrants of the Hall magnetic field were observed for each event.

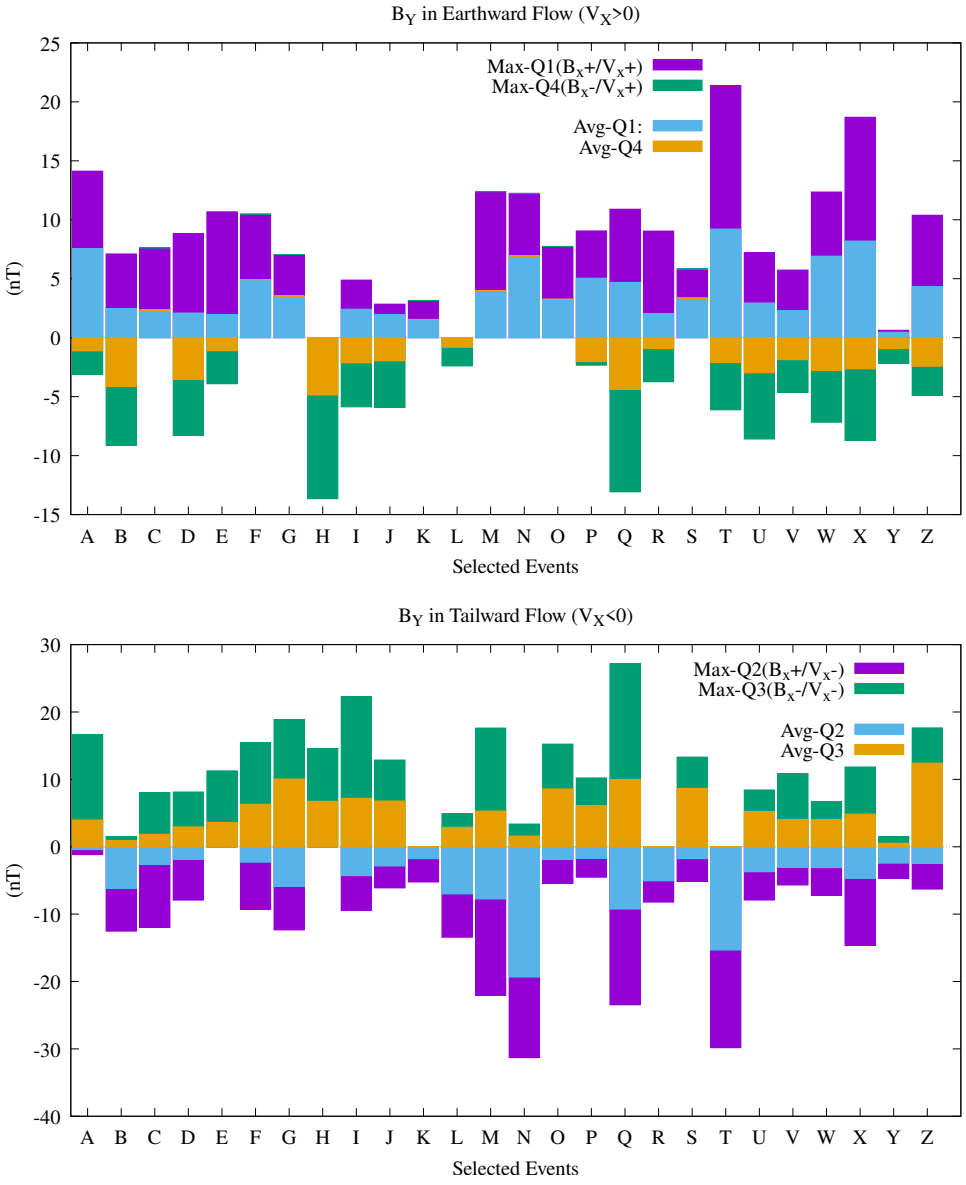

Figure 2.13: Out-of-plane (Hall) magnetic fields as approximated by B_y with Earthward ion flow (upper graph) and with tailward ion flow (lower graph). Detection of at least two quadrants of the quadrupolar Hall magnetic field is part of the algorithm's Stage 2 requirements. Quadrants are organized and labelled after Figure 1.6. Not all quadrants are observed for all events.

Regarding the distribution of IDRs in the magnetotail, Figure 2.14 shows the locations of the IDRs listed in Table 2.2 over an underlay of the dwell time from Figure 2.1. Figure 2.15 shows the total hours spent in the plasma sheet by MMS as a function of position in MLT. The event distribution shows a clear preference for the dusk region of the magnetotail. The mechanism for this distribution is discussed in more detail in Section 4.4.

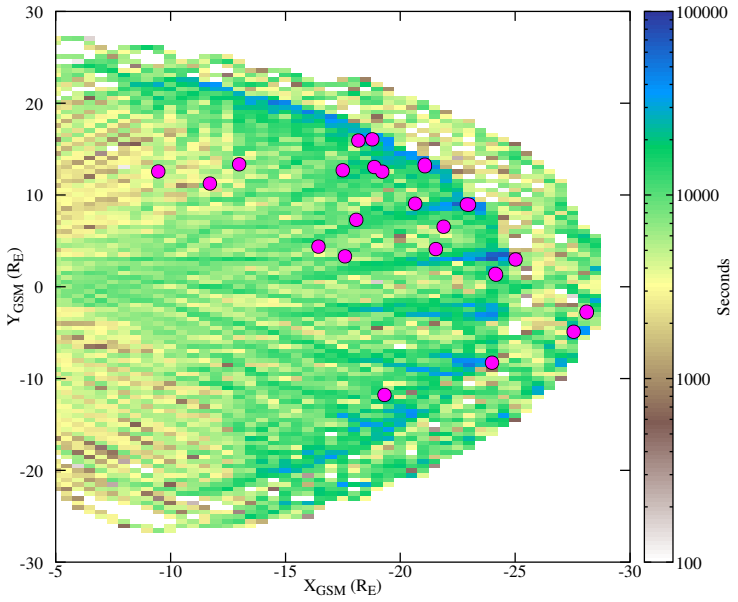

Figure 2.14: A plot of the time MMS spent in the tail plasma sheet as determined by ion density measured by the FPI instrument, after Figure 2.1. Magenta circles indicate the locations of IDRs identified using the algorithm described above and listed in Table 2.2.

2.6 Discussion

2.6.1 Mechanics and Limitations to the Algorithm

The criteria employed in this algorithm are, in most respects, highly conservative when attempting to identify IDRs. The adherence to considering only those IDRs which are well-aligned with the GSM coordinate system eliminates some otherwise strong candidates (see

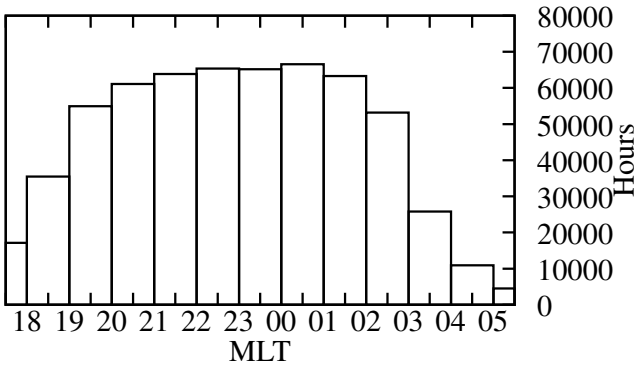

Figure 2.15: A histogram showing the same data as in Figure 2.1 but summed within the divisions of Magnetic Local Time (MLT) and converted to hours instead of seconds. The pre- and post-midnight dwell times across the MMS mission are shown to be reasonably even.

Section 3.1.1). Similarly, requiring the detection of an ion flow reversal is highly restrictive and eliminates events similar to the diffusion region encountered by Polar and described by Mozer et al. (2002). The observatory during that event (the Polar spacecraft [Acuna et al., 1995]) traversed the diffusion region normal to the reconnecting current sheet (the z-direction in Figure 1.6) and on only one side of the X-line, meaning that it only observed one reconnecting outflow jet and would, therefore, not have passed the first stage of the algorithm described here. Events with strongly bifurcated flow reversals such as event Q in Table 2.2 or that described by Runov et al. (2003) may also not be identified if the passage through the inflow region exceeds 180s.

The strong electric field requirement ($|\vec{E}| \geq 10mV/m$) also serves to limit detection of weaker or secondary reconnection diffusion regions such as that reported by Zhou et al. (2019), where the strong electric fields were present at some distance from the ion flow reversal. Events such as this often display weak but clear Hall electric and magnetic fields in the neighborhood surrounding a clear ion flow and normal magnetic field reversal, but are accompanied by only a small increase in the magnitude of the electric field overall. The criteria here, both in terms of the electric field magnitude and the timing of the correlated

ion flow and normal magnetic field reversal, were made intentionally restrictive so as to, hopefully, provide a collection of example IDR events which can be considered such beyond a reasonable doubt.

One noteworthy point regarding those flow reversals which do not display significant Hall fields is how common they are. There is a factor of five drop in the number of events satisfying Stage 1 to those also satisfying Stage 2. Several of the events which satisfied Stage 1 were identified as NAFR similar to those reported in Geotail observations [Nagai et al., 2013]. An example is given in Figure 2.16. Here we see a clear correlated reversal from Earthward ion flow and northward magnetic field to tailward ion flow and southward magnetic field. However, strong electric fields are missing from the region, nor is significant evidence of Hall electric or magnetic fields found (in fact E_Z points *oppositely* to the direction expected from a Hall electric field). The missing elements combined with a strong, steady B_X suggest passage of the observatory through a Plasma Sheet Boundary Layer (PSBL) or other benign phenomena.

Some events which satisfy the criteria of all three stages are still questionable examples of IDRs. One such is shown in Figure 2.17. Here a strong ion flow reverses slowly from -315 to $170 km/s$ in a moderately active magnetic field. There are numerous instances during this flow reversal of B_z crossing zero from negative to positive, but none appear to line up well with the flow reversal, the one closest in time as well as the most prominent preceding the flow reversal by $\sim 50s$. The Hall electric and magnetic fields are, likewise, indicated in places but are occasionally contradicted. Despite strong electric fields consistent with a Hall electric field at the center of the flow reversal, the electric fields elsewhere are less indicative of an IDR. The flow reversal itself is strongly bifurcated with $V_i \approx 0$ for approximately a minute between distinct tailward and Earthward flows. The strong and consistent value of B_x combined with a fairly weak plasma density raise the possibility that the observations were made in or near the PSBL and away from the possible reconnecting current sheet.

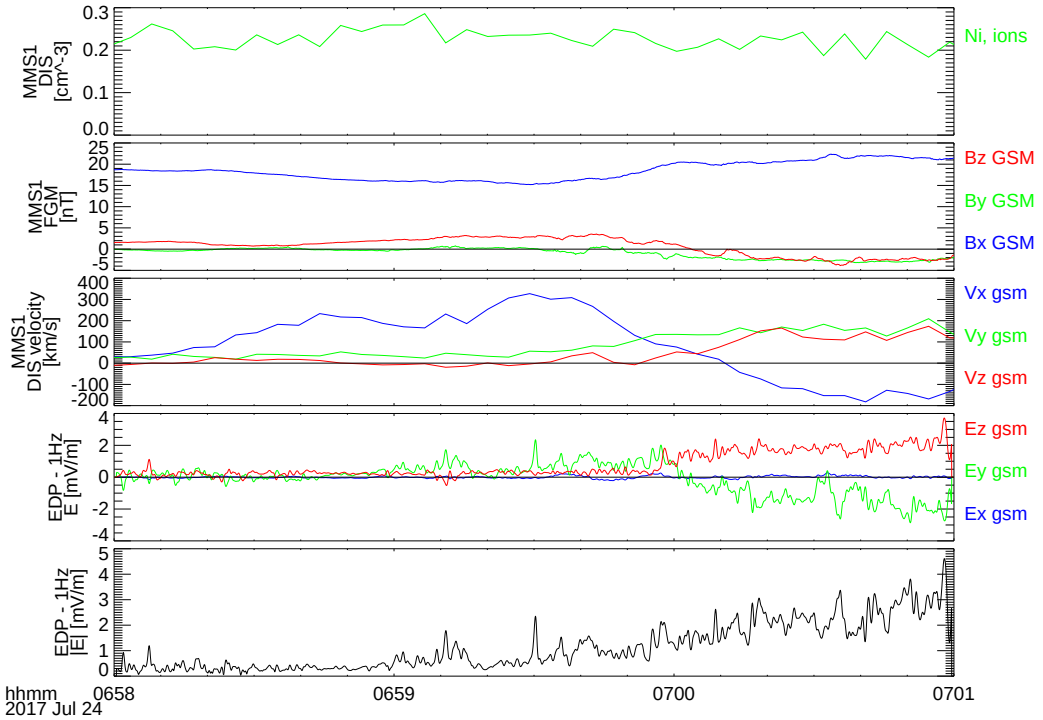

Figure 2.16: This shows an ion flow reversal from Earthward to tailward preceded by a correlated reversal of the Z_{GSM}-component of the magnetic field $\sim 10s$ before, satisfying the Stage 1 selection criteria. However, other indicators of an IDR are missing (Hall fields, strong $|\vec{E}|$). This is classified as nonactive flow reversal.

These reasons conspire to relegate this and similar events to being excluded from the list of confirmed IDRs, despite having passed all three stages of the algorithm.

The threshold ratio of B_y measurements of the correct polarity to indicate a Hall magnetic field used in this study may appear small when compared to what is expected from an idea 2-D reconnection picture such as shown in Figure 1.6. Indeed, many of the events reported in Table 2.2 have ratios greatly in excess of 0.5 or even 0.9 throughout the suspected IDR region. However, some clear IDR events do not have such large ratios in all quadrants. One example is event H (see Figure 2.4 where the Hall ratio for Quadrant 1 is 1.0 but only ~ 0.2 for Quadrant 2 while all other quadrants are entirely unrepresented. Similarly, a large Hall ratio does not guarantee clear identification as an IDR as is the case with the event shown in Figure 2.17. There the Hall ratio exceeds 0.8 for both quadrants where $B_x < 0$ throughout the region shown but, as discussed above, the totality of the evidence does not support the identification of the event as an IDR. The ratio of 0.1 used for this study represents the compromise chosen to require a strong indication of possible Hall magnetic fields while not eliminating those events which may not display textbook examples due to X-line motion or other effects.

2.6.2 Historical Considerations

The abundance of correlated magnetic field and ion flow reversals without significant electric fields or evidence of Hall fields calls into question a common assumption in the study of magnetic reconnection; that such correlated field and flow reversals are a sure indicator of a reconnection diffusion region. This assumption has existed and flourished as the foundational standard for observing reconnection for generations (*e.g.* Frank et al. [1976] and references therein). However, nonactive flow reversals such as that shown in Figure 2.16 represent a large portion of the total time-correlated field and flow reversals observed by MMS in the magnetotail, showing that identifying magnetic reconnection is a far more subtle art than has

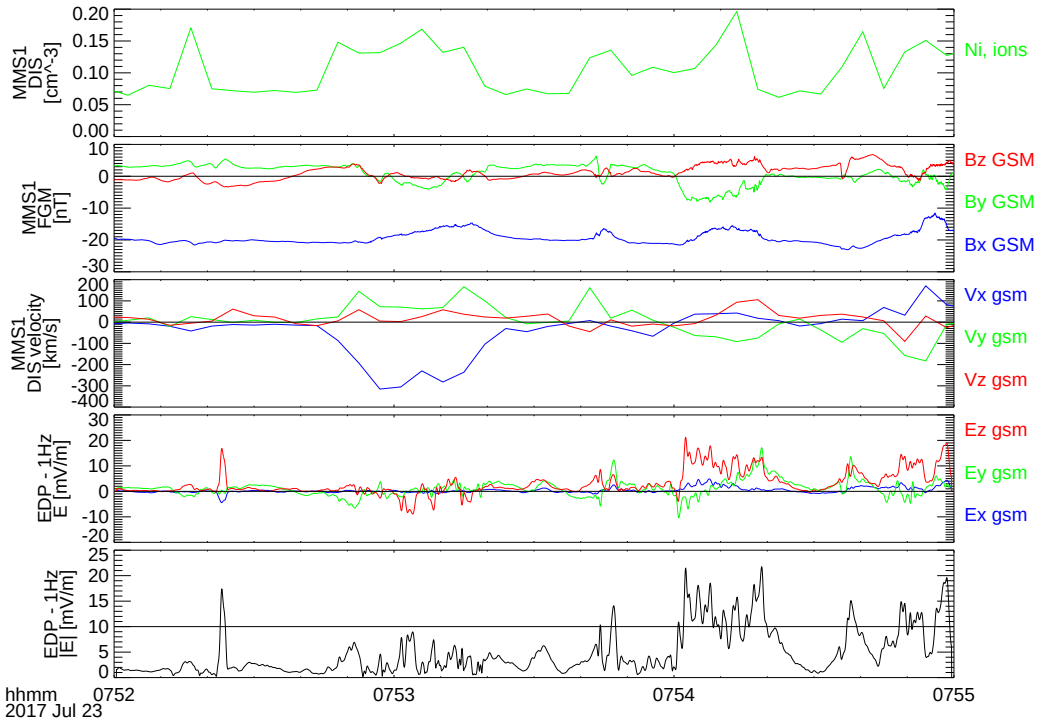

Figure 2.17: This is a plot of data for an event which passed all three stages of the algorithm but was found not to be an IDR on human review. Note the intermittent Hall electric and magnetic fields and uncertain reversal in B_z. Due to these conditions and despite the strong, if bifurcated, ion flow reversal, the event was determined to not be an IDR.

been previously assumed. The inclusion of additional criteria such as significant evidence of Hall electric and magnetic fields, greatly improves the likelihood of successful identification.

The observations of IDRs made by Eastwood et al. (2010) using Cluster were over a similar period of time (2001 – 2005) using a similar suite of instruments so it is reasonable to compare the results of this automated algorithm to those described there. All four quadrants of the Hall magnetic field structure are observed clearly in 13 of 26 events reported here with a typical spacecraft separation of $\sim 15km$ in a tetrahedron formation. The Cluster mission, with spacecraft separation between $200 - 2000km$ for all orbits reported by Eastwood et al., observed all four quadrant in 6 of 18 diffusion regions. In both studies at least two quadrants were observed for each event and typically more (see Figure 2.13). The average Hall electric field observed by MMS in this study was $3.28mV/m$ while south of the reconnecting current sheet and $-3.09mV/m$ while north of it; the comparable values for the Cluster study were somewhat greater in magnitude at $5.33mV/m$ and $-6.47mV/m$ respectively. The reason for the differences in Hall field observations are unclear but may be the differences in spacecraft separation. The difference in total observed IDRs can be most easily attributed to the greater range of radial distance from the Earth sampled by MMS relative to Cluster but may also have been influenced by differences in global driving conditions.

An interesting result of the observational statistics is this: the total number of IDRs reported in 2017 also conforms with predictions made by Genestreti et al. pre-launch [Genestreti et al., 2014]. They made a statistical analysis of the distribution of all IDRs observed by Cluster and Geotail and compared that distribution to the planned orbits of the first magnetotail science phase of MMS during the summer of 2017, predicting that MMS should encounter 11 ± 4 IDRs during that phase. As seen in Table 2.2, the algorithm described here identified 12 IDRs during that season which were confirmed by human review; comfortably within the number expected by Genestreti et al. The spatial distribution of events strongly favors the duskside ($Y_{GSM} > 0$), as seen in Figure 2.14, even more so than was predicted by

Genestreti et al. This is discussed more in Chapter 4.

2.7 Summary and Remarks

I developed an algorithm to identify IDRs using a step-wise series of boolean conditions and applied it to MMS *in situ* observations in the geomagnetic tail over four consecutive tail seasons ($\sim$ 550days). The steps test for specific topological parameters in the magnetic and electric field as well as the bulk ion flow to allow a reasonable degree of confidence in the regions identified by the code. Using this method, I identified a total of 26 IDRs during the 2017–2020 tail seasons and showed some statistics of those events related to the selection criteria. These events also bear statistical similarity to those reported by Eastwood et al. (2010) granting even more confidence in the methodology used. While far from perfect, this algorithm has proven useful in data reduction by identifying candidate IDR events for human review and has led to a library of reconnection events in the tail which can be used for statistical and other studies [Rogers et al., 2021]. The algorithm itself and the initial results of the 2017 tail season were published in the Journal of Geophysical Research: Space Physics in 2019 [Rogers et al., 2019a] and citations indicate it has proven useful to others in the field.

Most interestingly, however, the analysis of the distribution of identified IDRs compared with the observed tail plasma sheet shows that while MMS has only a slight orbital dusk-dawn bias (see Figure 2.15) there is a very strong asymmetry in the distribution of IDRs (see Figure 2.14). The disparity in these distributions implies that the dawn-dusk asymmetry in IDR location is not due to simple observation bias, *i.e.* not due to MMS spending more of its time looking on the duskside than the dawnside, but is instead a result of underlying physical processes. An exploration of what these underlying processes might be is the subject of the following chapters.

CHAPTER 3

IDR Phenomenology Using Scalar Parameters

3.1 The Problem With Vector Parameters

The dependence of the algorithm described in Chapter 2 on the GSM coordinate system stems from the usage of vector parameters which depend on the direction they point, as well as their magnitude. Both Stages 1 and 2 depend on both the magnitude of various parameters as well as their direction relative to each other (*e.g.* V_x and B_z reversals; see Section 2.2). All of these directional relationships are drawn from expectations derived from the basic picture of Hall reconnection (Figure 1.6) where various plasma flow, electric field, and magnetic field variations relative to the reconnecting current sheet are organized in a self-consistent coordinate system. In the geomagnetic tail, the central current sheet, between tail lobes and nominally parallel to the solar system ecliptic, is the source region for localized thin current sheets which may support reconnection. The geometry of the tail and the central current sheet is nominally reasonably well-aligned with the GSM coordinate system, allowing the axes of Hall reconnection from Figure 1.6 to generally match those of the GSM system (similar arguments can also be made for the GSE and other coordinate systems, but we will ignore those for the moment).

This happy circumstance does not always obtain, however. The tail current sheet is frequently *not* static, flapping and twisting in response to changes in solar wind plasma flow perpendicular to the ecliptic [Sergeev et al., 2008] as well as plasma flow and IMF changes parallel to the ecliptic and tangential to the Earth's orbital path [Zhang et al.,

2002a]. These conditions can lead to the central tail current sheet to temporarily be no longer even notionally aligned with the GSM or any similar coordinate system. As the inherent orientation of Hall reconnection is related to the reconnecting current sheet, the variations in parameters familiar to the Hall picture will be relatively unchanged, but the axes of those variations, the boundary normal coordinate system of tail reconnection, will no longer bear any similarity to the GSM coordinate system.

Several methods have been suggested for finding a boundary normal coordinate system, the most common being that found using Minimum Variance Analysis (MVA) on the time series magnetic field vector data as the observatory crosses the current sheet or other topological boundary. This method is essentially finding the eigenvectors and values of a covariance matrix of the relevant magnetic field data, the eigenvectors forming a rotation matrix from the starting coordinate system to one with one axis along the direction of maximum variance in the magnetic field (commonly referred to as the $\hat{L}$-direction), another axis normal to the first in the direction of minimum variance (the $\hat{N}$-direction), and the third normal to both of the first two to make a right-handed coordinate system (the $\hat{M}$-direction) [Sonnerup and Cahill, 1967]. This or any other boundary normal coordinate system is often referred to as an LMN coordinate system, with axes organized as described above.

However, this and other methods have been shown to be of inconsistent reliability, often disagreeing by significant degrees [Genestreti et al., 2018]. The inherent uncertainty in LMN methods is exacerbated during periods of particularly active IMF and solar wind activity when the tail current sheet may be flapping, twisting, or both during an ongoing reconnection event Cowley [1981]. An example of this is Event F in Table 2.2 and described in Subsection 2.3.2. The strong Y_{GSM}-component ion flows and electric field indicate that the tail current sheet is at least moderately tilted during this event (Zhang et al. [2002b] and references therein). The rapid, sinusoidal oscillations in the X_{GSM}-component of the magnetic field indicate that the tail was also flapping up and down relative to the ecliptic. Performing

MVA analysis on the five current sheet crossings (identified by $B_x = 0$) closest to the ion flow reversal give a variation of almost 30° in the $\hat{N}$ and $\hat{M}$ directions. Fortunately, there remained sufficient variation in these parameters when projected onto GSM coordinates for the algorithm to identify this event. Other examples are not so fortunate.

3.1.1 June 17, 2017

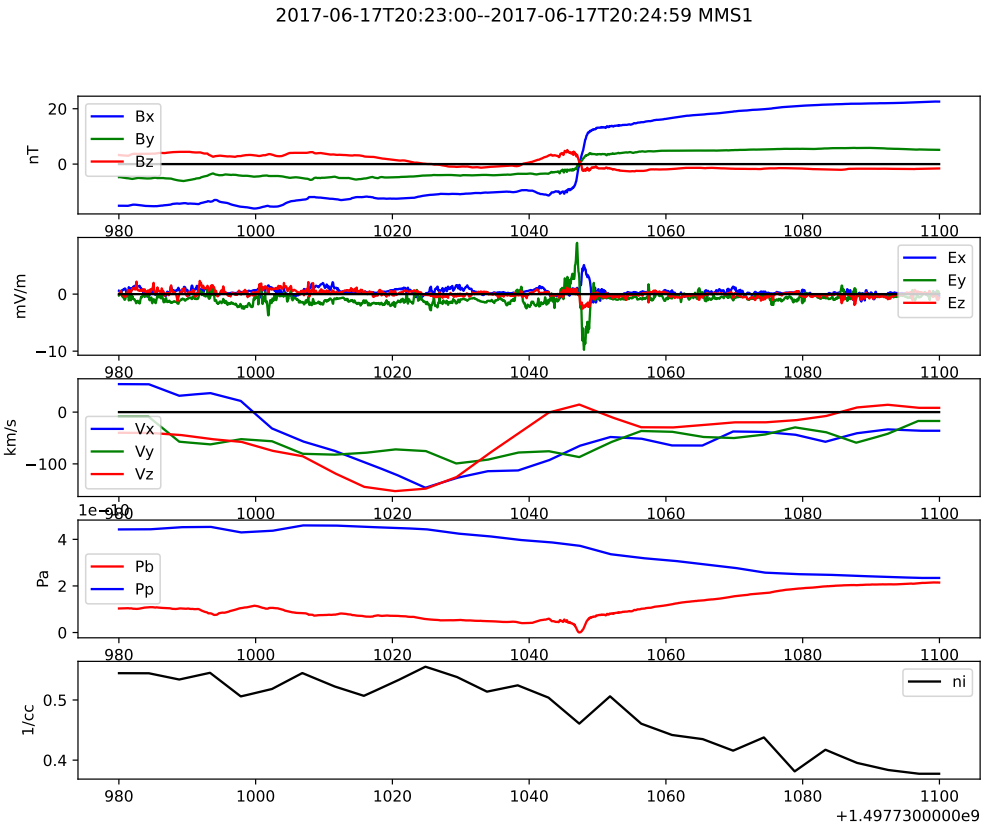

Figure 3.1: The key IDR selection parameters as described in Ch. 2 as measured by MMS1 in GSM coordinates. See text for details.

A reconnection event which was not sufficiently projected into GSM coordinates for the algorithm to identify it occurred on June 17, 2017, the nominal vector selection parameters of which, as defined in Section 2.2 are shown in Figure 3.1. The top panel shows the vector magnetic field with a clear, clean current sheet crossing just after 2024 UTC. The ion flow

velocity shown in the third panel does show a flow reversal in V_x which is nominally correlated with the B_z magnetic field reversal at the current sheet crossing, but the flow speeds are very weak (see the discussion in Section 3.4.1). The electric field vector, shown in the second panel is also of lower magnitude than might be expected, and the expected Hall electric field in E_z is all but absent. For all of these reasons, this event was not selected by the algorithm described in Chapter 2.

This event was initially identified as a point of secondary reconnection (*i.e.* reconnection between adjacent discrete flux tubes generated by a primary reconnection site and then cast off, typically tailward, of the X-line) by Huwang et al. (2018). As Electron jets were observed but, on cursory inspection, there does not seem to be any significant ion involvement in the energy conversion (*i.e.* lack of obvious Hall fields, low ion speeds), this was initially classified as an instance of electron-only reconnection [Huang et al., 2018]. However, Farrugia et al. (2021) argued that the mesoscale tail flapping which this event was a part of (see Figure 3.2) introduced different dynamics into the situation, specifically that the current sheet was not parallel to the ecliptic as is typical in the quiet magnetotail, but was twisted nearly 90°, and identified Hall signatures indicative of ion demagnetization and energization when viewed in the twisted frame [Farrugia et al., 2021].

3.1.2 A Scalar Solution

As one cannot be sure if the system used for determining the LMN system is correctly aligned with the reconnecting current sheet, the identification methods used in Chapter 2, even modified to be applied to an LMN coordinate system, become liable to miss likely sites of reconnection. One solution to this conundrum would be to use identifying criteria which were not dependant on any spatial coordinate system. Such scalar parameters would, in theory, be applicable regardless of tail current sheet orientation or even in very different reconnection environments such as the magnetopause and elsewhere. If successful, identifying

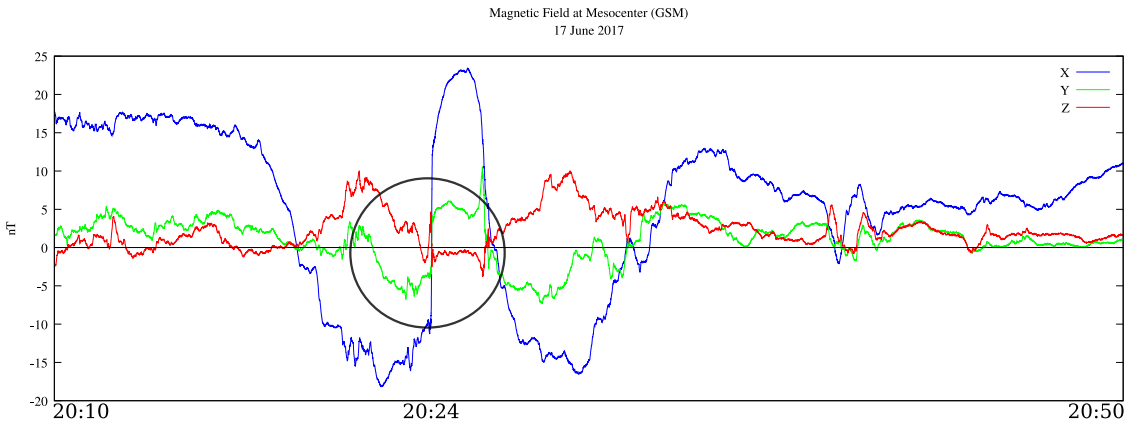

Figure 3.2: A context view of the magnetic field vector for June 17, 2017. The event shown in Figure 3.1 is in the region indicated by the black circle. Note the nearly sinusoidal oscillation of the B_x component of the magnetic field across the 40 minute window; this is an indication of the tail flapping or waving perpendicular to the ecliptic. The more subtle sinusoidal motion of the B_y component is indicative of possible twisting of the tail along the Earth–Sun axis.

the temporal location of a reconnecting current sheet in *in situ* data would provide additional information which could improve the quality of a boundary normal coordinate system applied for further study. Regardless, scalar parameters would provide a method of analysis and comparison between reconnection events without the otherwise necessary debate over the relative alignment of the coordinate systems used.

Several scalar parameters have been suggested and explored using both *in situ* data and simulations in attempts to elucidate the electron diffusion region (EDR) and reconnection in general. In point of fact, nearly all scalar parameters which have been discussed in literature (since the end of the 20th century, certainly) have been designed to identify the EDR from single-spacecraft data. Upon even cursory investigation, however, those parameters which purport to apply to electrons can be easily adapted to search for ion diffusion regions. A few of the most promising scalar parameters will now be described and discussed for utility as IDR identifiers.

3.2 A Selection of Scalar Parameters

3.2.1 Ion Bulk Speed: $|\vec{V_i}|$

One of the earliest scalar parameters used to identify possible sites of reconnection was the bulk plasma (or bulk ion) speed $|V_i|$. Some of the earliest *in situ* observations of reconnection both in the magnetotail (*e.g.* Frank et al. 1976) and at the magnetopause (*e.g.* Sönnerup et al. 1981) used the magnitude of the bulk ion flow as an indicator that a reconnecting X-line was near. Given that a result of Hall reconnection is a high-speed outflow of plasma parallel to and away from the reconnecting current sheet, this seems a reasonable expectation that an observer is near, if not on top of, a reconnecting X-line.

3.2.2 The Kappa Parameter: K_i

Büchner and Zelenyi [1987] derived another scalar parameter directly comparing plasma parameters with the local magnetic field topology. Taking a kinetic approach from first principals, they state that if either the plasma is sufficiently accelerated perpendicular to the local magnetic field, or if the topology of the local magnetic field has a large enough gradient, then the plasma will cease to be adiabatically tied to the magnetic field or even become totally demagnetized. In either case they conclude that this will lead to charge separation in any heterogeneous plasma and thus electric fields and net currents; essentially the mechanism by which the Hall fields predicted by Dungey, Vasyliunas, and Sönnerup are formed. The scalar parameter by which they indicate this process is $K^2 = R_C/\rho$ where R_C is the radius of magnetic field line curvature and ρ is the plasma gyroradius. Non-adiabatic or chaotic behavior can begin at $K \approx 3$ with partial demagnetization beginning at $K = 1$ and total demagnetization at $K \leq 0.2$ [Büchner and Zelenyi, 1987, 1989]. By choosing what gyroradius is to be compared, the chaotic behavior of different plasma populations can be investigated.

The calculation of the radius of magnetic field line curvature $R_C = \left((\hat{b} \cdot \nabla)\hat{b}\right)^{-1}$ is a fairly simple vector calculus problem when the magnetic field $\hat{b} = \vec{B}/|\vec{B}|$ can be treated analytically. It is a more significant challenge when attempting to approximate it from discrete measurements of the four MMS observatories. Specifically, the calculation of the gradient of a vector field (in this case $\nabla\hat{b}$) from discrete data is an exercise in both applied mathematics to theorize and drive, and programming skill to implement. Two different mathematical methods were developed in preparation of the Cluster mission, one founded on the mathematical conceit of least-squares minimization [Harvey, 1998], the other on the more geometric method of reciprocal vectors [Chanteur and Harvey, 1998]. Each of these has its own characteristic benefits and limitations, but equivalent in their results calculated to the accuracy possible in computer floating point calculations. Due to its greater computation efficacy as I've implemented each method, the method of reciprocal vectors is used as the foundation for calculating both the $\nabla\hat{b}$ used for the K parameter, as well as $\nabla\vec{B}$ used for the current density $|j|$.

Understanding and implementing each method was no small part of the work done for this thesis, however the details and minutia of this development work is outside the scope of the discussion of the science implications of the results here. A summary of the methods and their implementation are found in Appendix A.

3.2.3 Agyrotropy: $\sqrt{Q}$

A more direct means of testing the first adiabatic invariant ($\mu = \frac{mv_\perp}{2B}$ =a constant) can be made by investigating off-diagonal terms of the pressure tensor derived from the plasma energy distribution function. Several means of quantifying plasma agyrotropy have been suggested along similar lines. $A\emptyset$ [Scudder and Daughton, 2008] uses a ratio of eigenvectors of the pressure or temperature tensor; AG [Che et al., 2018] uses the difference in determinants of the full and ideal portion of the pressure tensor; and $\sqrt{Q}$ [Swisdak, 2016] is the ratio

of the quadratic sum of the off-diagonal components of the pressure tensor to that of the diagonal components. The agyrotropy of different species of plasma can be investigated using any of these techniques by way of using the appropriate pressure tensor derived from that species' distribution function. Work presented at the AGU Fall Meeting showed that $\sqrt{Q}_i$ displayed the best discrimination between active and non-active regions when applied to ion data [Rogers et al., 2019b].

For a Pressure tensor $\overline{\overline{P}}$ such that:

$$\overline{\overline{P}} = \begin{vmatrix} P_{\parallel} & P_a & P_b \\ P_a & P_{\perp} & P_c \\ P_b & P_c & P_{\perp} \end{vmatrix} \tag{3.1}$$

$$\sqrt{Q} = \sqrt{\frac{P_a^2 + P_b^2 + P_c^2}{P_{\perp}^2 + 2P_{\perp}P_{\parallel}}}$$

3.2.4 Parallel Electric Field: $\vec{E}_{\parallel}$

A non-zero electric field component parallel to the local magnetic field has been an ideal signifier of magnetic reconnection since the concept's formalization [Dungey, 1958]. The canonical MHD electric field is a product of plasma convection $\vec{E} = -\vec{V} \times \vec{B}$ in a collisionless plasma, requiring an anomalous resistivity, modification of MHD for a compressible plasma fluid, or outright contraindication of MHD in favor of a kinetic description in the event of a parallel electric field. Given the difficulty of obtaining accurate electric field measurements *in situ*, it was many years before any observational indications of a parallel electric field ($E_{\parallel}$) were recorded [Mozer et al., 1979], and still more until it was clearly observed at the magnetopause [Scudder et al., 2002].

3.2.5 Energy Conversion Rate: $\vec{j} \cdot \vec{E}$

The same limitations outlined for the observation of $E_{\parallel}$ inhibited the measurement of the energy conversion rate $\vec{j} \cdot \vec{E}$ before [Mozer et al., 1979]. $\vec{j} \cdot \vec{E}$ should be at or near zero in a well-behaved frozen into the magnetic field; a non-zero value indicates energy transfer between the plasma and electric and magnetic fields, requiring non-convective electric fields with the attendant considerations. A positive value of $\vec{j} \cdot \vec{E}$ is generally interpreted as a transfer of energy from the magnetic field to the plasma, while a negative value is interpreted as the reverse [Payne et al., 2021].

3.2.6 Current Density Magnitude: $|\vec{j}|$

An increase in the local current density $|\vec{j}|$ is another logical consequence of Hall reconnection. Hall currents will travel along the separatricies as well as in the out-of-plane direction along the reconnecting X-line ($\hat{y}$-direction in Figure 1.6). While benign currents totally unrelated to reconnection (*e.g.* gradient drift and curvature drift currents) can and do occur, their magnitudes tend to be dwarfed by those associated with a reconnecting current sheet. Therefore a significant (*i.e.* an order of magnitude or greater) increase in the current density is a reasonable indicator that further investigation is justified.

3.2.7 Electric Field Magnitude: $|\vec{E}|$

An argument similar to that used in favor of $|\vec{j}|$ can be made for using a strong electric field magnitude $|\vec{E}|$ as an indicator for reconnection. While convective electric fields are common throughout space and astrophysical plasmas, they are typically not stronger than a few millivolts per meter. Charge separation in the neighborhood of any ion-scale current sheet will produce Hall electric fields which increase in magnitude rapidly as the current sheet thins further. A reconnection electric field along the reconnecting X-line, while typically small,

will also contribute to increase the magnitude of the electric field in the neighborhood of a reconnecting current sheet beyond typical convective electric field magnitudes. Eastwood et al. argued that $|\vec{E}|$ is a critical identifier of ion diffusion regions in Cluster studies [Eastwood et al., 2010]. These arguments were considered sufficient to include electric field magnitude as the Stage 3 selection criteria for the IDR identification algorithm described in Chapter 2 [Rogers et al., 2019a].

3.2.8 Lorentz Ratio: Γ

A more subtle means of quantifying the relative influence of the electric field on plasma behavior comes from measuring the ratio of influence of the electric and magnetic field components of the Lorentz force. This so-called Lorentz ratio [Scudder and Mozer, 2005, Scudder et al., 2008] depends on the components of the electric field and plasma motion perpendicular to the magnetic field, complementing measurements of $E_{\parallel}$. The relative effect of each field on different plasma species can be tested by choosing the appropriate convective electric field component and perpendicular temperature, allowing for separate investigations of ion and electron diffusion regions.

$$\Gamma_i = \frac{|\vec{E}_{\perp} + \vec{V}_i \times \vec{B}|}{w_{\perp,i}|\vec{B}|}$$
$$\text{Where } w_{\perp,i} \equiv \sqrt{\frac{2k_B T_{\perp,i}}{m_i}} \tag{3.2}$$
$$\text{is the perpendicular thermal ion velocity}$$

For values of $\Gamma > 1.0$ $F_{E,\perp} > F_{B,\perp}$ with an assumed breakdown of the 1st adiabatic invariant and implies that non-convective electric fields are strong in the region, or that the magnetic field is too weak to dominate the plasma behavior. In either event, or in cases where both are true, the demagnetization and energization of the plasma is certain.

3.2.9 Ion Temperature

One of the most fundamental consequences of magnetic reconnection as theorized since its conception is energy diffusion by heating of the plasma. Plasma heating and acceleration have been constant expectations since the earliest exploration of the Sweet-Parker model [Parker, 1957]; while the $|V_i|$ parameter addresses one half of these expectations, the total ion temperature $T_i = \frac{1}{3}(T_\parallel + 2T_\perp \propto \frac{1}{3}\,\mathrm{Tr}(\overline{\overline{P}}))$ addresses the other. Unlike the ion agyrotropy, the ion temperature deals strictly with the trace of the field-aligned pressure tensor. The interior of the Ion Diffusion Region (IDR) should, by definition, contain ions with a higher temperature than those outside of the IDR. And as the magnetic field will be weakened in the interior of the IDR the temperature anisotropy (*i.e.* the difference between the parallel and perpendicular components of the trace of the temperature tensor) should be close to zero at the same time the total temperature is elevated.

3.3 The Behavior of Ion Scalar Parameters Near an IDR

In order to identify new IDRs using scalar parameters, it would be useful to first analyze how these parameters behave in the neighborhood of known IDRs. This accomplishes several valuable objectives. First, it provides a ready laboratory to compare the values measured near ion demagnetization and energization with those which the theoretical formulation of the scalar parameters would lead us to expect. Second, by comparing the values of scalar parameters measured in known active regions to those in nearby regions which are certainly not inside an IDR threshold values can be derived which would mark the transition into an IDR. Third, such analysis may provide further insight into the behavior and structure of IDRs beyond the simple Hall reconnection picture used in Chapter 2.

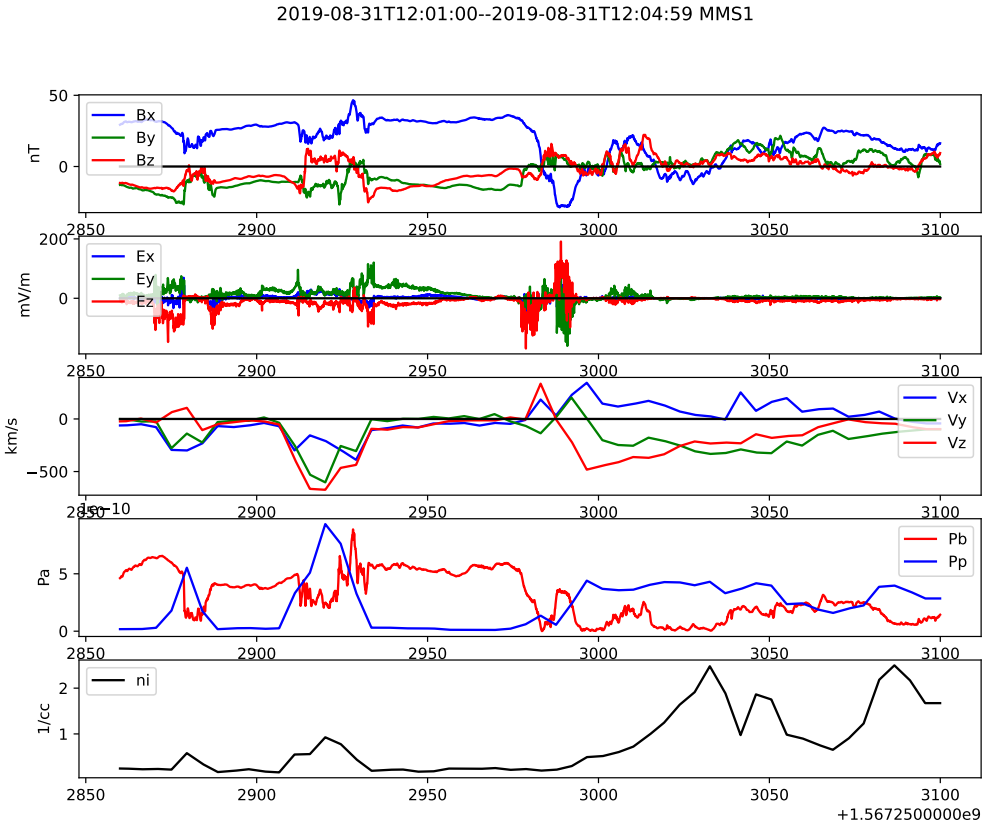

Figure 3.3: The key vector parameters of event 'T' from Table 2.2. From top to bottom: Magnetic field vector, Electric field vector, Ion bulk velocity vector, Magnetic (red) and plasma (blue) pressure, and ion number density. Note the Hall electric fields near current sheet crossing (B_x reversal) at 12:03:05 (2985s) and the correlated V_x (blue) and B_z (red) reversals.

3.3.1 August 31, 2019

We begin with a detailed look at a single event, previously identified as an IDR. Figure 3.3 shows four minutes roughly centered on IDR 'T' from Table 2.2. The top panel shows the magnetic field vector; the current sheet encounter is clearly seen, represented as a sharp reversal from positive to negative B_x (blue line). At the same time, the normal component of the magnetic field (B_z, red line) also reverses from negative (open to the IMF) to positive (closed to the terrestrial magnetosphere). The third panel down shows the ion bulk flow vector and a moderately strong reversal in V_x (blue line) from negative to positive correlates reasonably well with the B_z reversal. The second panel from the top shows the electric field vector components; a strong ($> 50mV/m$) Hall electric field ($\sim E_z$, red line) can be seen near the current sheet crossing. On inspection, the out-of-plane magnetic field (B_y, green line, top panel) is of the expected sign for a Hall magnetic field for much of the interval shown. Based on these characteristics, the event was selected as an IDR candidate by the algorithm described in Chapter 2 and confirmed on human review.

Figure 3.4 shows the same event and the same time interval using the scalar parameters outlined previously, all testing ion characteristics utilizing FPI ion moments. The K_i parameter, is shown first and displays values small enough for non-adiabatic motion ($K_i < 3$) in most areas near the plasma sheet (small B_x magnitude) and indicates complete ion demagnetization ($K_i < 0.2$) at the primary current sheet crossing at the center of the interval. The same regions also show enhanced values of $\sqrt{Q}$ (third panel), which indicate agyrotropic motion of the ions as determined by the ion pressure tensor. The Lorentz ratio (Γ, fourth panel) exceeds unity in the same locations and peaks greater than 10 at the primary current sheet crossing, indicating that the electric field is a stronger influence on the motion of ions in those regions than the magnetic field. The same locations, unsurprisingly at this point, also show moderate to strong energy conversion as indicated by non-zero $\vec{J} \cdot \vec{E}$ (fifth panel).

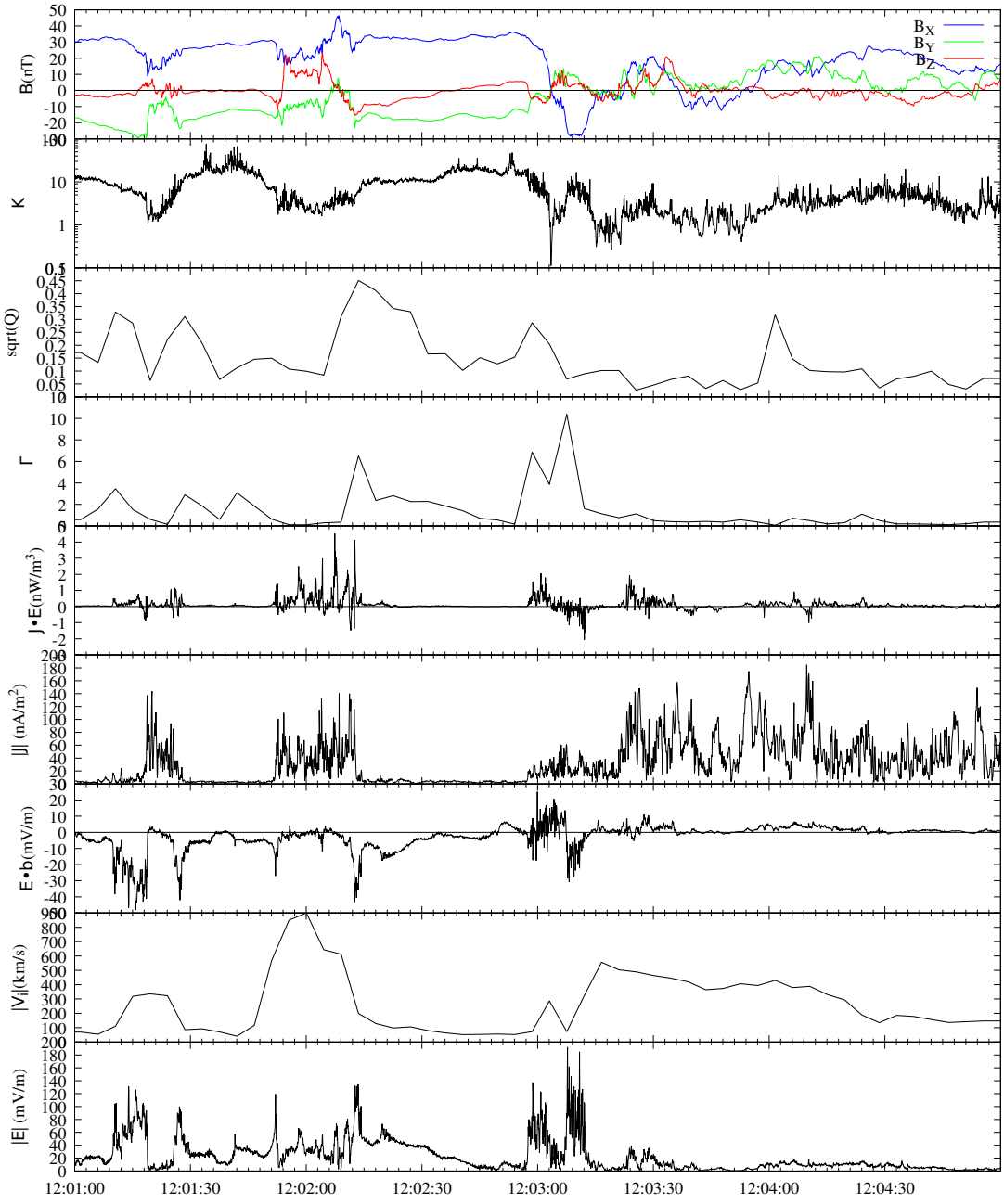

Figure 3.4: Event 'T' shown in selected scalar parameters. The magnetic field vector is included in the top panel for reference. Note that the Lorentz Ratio is labeled here as Γ and the Parallel electric field is labeled as $\vec{E} \cdot \hat{b}$.

The extended region of negative $\vec{J} \cdot \vec{E}$ just after the primary current sheet crossing may indicate a generator region, typically located in the outer EDR [Payne et al., 2021].

The current density ($|\vec{j}|$, sixth panel) and electric field ($|\vec{E}|$, bottom panel) magnitudes both show enhancements orders of magnitude greater than the typical quiet tail plasma sheet [Baumjohann, 1993]. The parallel electric field (shown here as $\vec{E} \cdot \hat{b}$, seventh panel) shows very strong DC values throughout this region, adding further evidence to the interpretation that ions and electrons are behaving very differently, and that a great deal of energy is being exchanged in much of this region. The bulk ion speed (eighth panel) shows that some of that energy is going into accelerating ions on either side of the primary current sheet crossing. The final scalar parameter is the ion temperature, shown in Figure 3.5, which indicates that the ions are being heated as well as accelerated during this event.

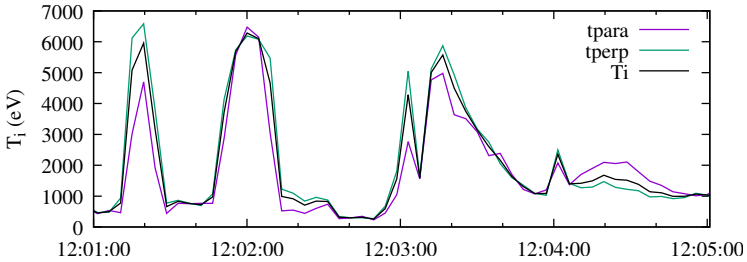

Figure 3.5: The ion temperature diagonal components for the event 'T'.

3.4 Statistical Phenomenology of Scalar Parameters near IDRs

Having shown that scalar parameters applied to ion data of a known IDR behave as predicted from their theoretical basis, the next logical step is to compare each scalar parameter's behavior over *all* identified IDRs and determine what behavior is typical. This has the added benefit of moving towards the second objective from Section 3.3 in showing what range of values are obtained for each parameter across all IDRs and what patterns may be common. By looking at the statistical behavior in time surrounding IDRs, we may also gain

some insight into the relative boundaries identified by each parameter, thus contributing to the third objective as well.

The methodology used is to perform Superposed Epoch Analysis (SEA) of the values of each scalar parameter over a ten-minute period centered on the local minimum in the total magnetic field magnitude associated with each IDR. This epoch was chosen based on the symmetric reconnection assumption that the magnitude of the magnetic field is inversely proportional to the distance from the center of the reconnecting current sheet. The median and mean values for each time step in this interval across all 26 IDRs identified and listed in Table 2.2 are calculated, as well as a 95% ($\approx 2\sigma$) interval about the median, for each parameter and discussed below.

3.4.1 Statistical Phenomenology of $|\vec{V}_i|$

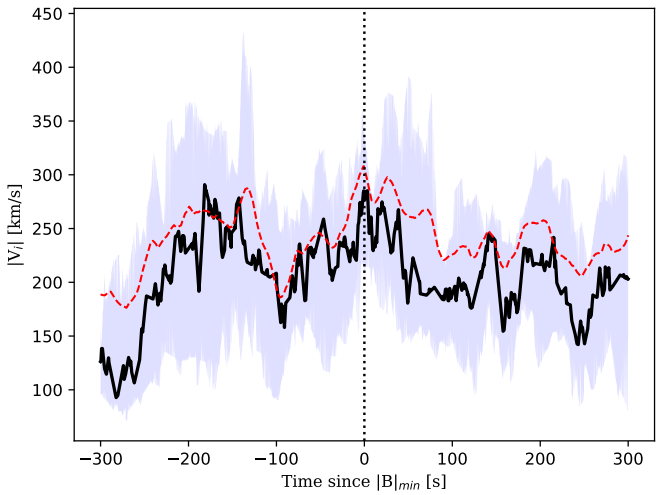

Figure 3.6: The superposed epoch analysis of the bulk ion speed for all IDRs listed in Table 2.2, covering the five minutes before and after the minimum magnetic field magnitude associated with each event. The black solid line is the median value and the red dashed line is the mean value across all events at that time step away from $|B|_{min}$. The gray background fill is the 95% confidence interval ($\approx 2\sigma$) about the median values.

The statistical values of the bulk ion speed for 10 minutes surrounding each listed IDR are

shown in Figure 3.6. Mean values are almost always higher than median values throughout the range, and at times the mean exceeds the 2σ range away from the median. This indicates that while typical ion speeds in these locations are more moderate, closer to the median values, occasional events occur which display *much* larger ion flow speeds either before the magnetic field minimum, after it, or both.

In comparison to previous studies (*e.g.* those using Cluster or Geotail data) the most striking feature of this figure may be the small scale of the values. Ion speeds of $\sim 1000 km/s$ are routinely reported from Geotail observations near reconnection sites [Nagai et al., 1998, 2001, 2005, 2013] while the maximum to be expected from MMS observations according to this figure would be at least a factor of two less than that. One possible explanation for this lies in the relative energy ranges sampled by the ion instruments on each mission. The Comprehensive Plasma Instrumentation (CPI) onboard Geotail is capable of resolving the bulk velocity of protons (the overwhelming majority of tail ions) up to energies of $48 keV$ [Nishida, 1994], while the FPI instrument onboard MMS from which these measurements are taken can only resolve proton moments to $\sim 30 keV$ [Pollock et al., 2016], leading to a difference in the range of the distribution function measured by each. Thus it is certainly possible that MMS cannot actually resolve the full ion energy distribution well enough to provide accurate bulk velocity measurements for energetic ion populations. This would have the result of under-reporting the bulk velocity by potentially significant amounts, especially in regions where ions have been heated and accelerated such as is expected in the neighborhood of an IDR.

Another interesting characteristic shown in Figure 3.6 is the peak at the epoch center. The simple picture of Hall reconnection shown in Figure 1.6 would suggest that the flow reversal, and thus lowest flow speed or stagnation point, should be co-located with the X-line at or near the magnetic field minimum. In this figure, however, that location has the highest mean and (nearly) highest median values. Instead, minimums appear within $100 s$

on either side of the $|B|_{min}$ epoch, indicating that the stagnation point is typically offset from the magnetic field minimum. As the outflow jets are likely the dominant source of ion flow near an IDR in the tail, an offset stagnation point, especially when in combination with asymmetric outflow speeds, would suggest that the X-line itself is in motion parallel to the direction of outflow, *i.e.* towards or away from the Earth.

3.4.2 Statistical Phenomenology of K_i

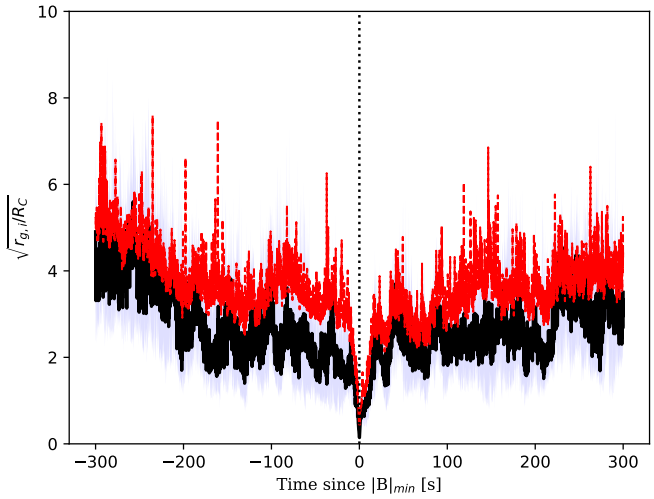

Figure 3.7: The superposed epoch analysis of the parameter $K_i = \sqrt{R_C/\rho_i}$ for all IDRs listed in Table 2.2 except Event 'B', in the style of Figure 3.6.

The statistical values of the Kappa parameter [Büchner and Zelenyi, 1987] for 10 minutes surrounding all the IDRs listed previously are shown in Figure 3.7, with the exception of Event 'B'. Event 'B' was excluded as only three of the four observatories were in operation during this event, making the full magnetic field gradient impossible to calculate. The noise in both the median and mean values for K make the 2σ ranges difficult to distinguish, but offer an idea of the range of variability in their own right. The median values indicate that the ions typically do not begin to strain the first adiabatic invariant until within approximately 3.5 minutes of the magnetic field minimum when values drop below $K_i \approx 3$. Full

demagnetization, implied by $K_i < 0.2$, does not occur until within seconds of the minimum, implying that full demagnetization of ions only occurs at the heart of the IDR, near the transition to the EDR.

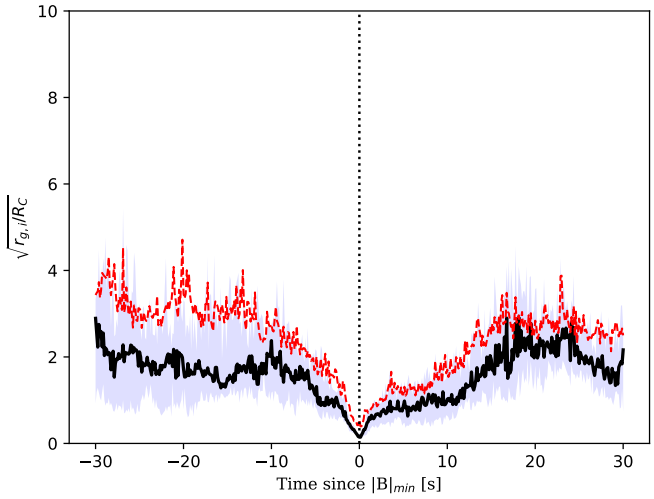

Figure 3.8: A detail of Figure 3.7 showing the central 60s

Both the mean and median curves have their minimums at (or very near) the magnetic field minimum (see Figure 3.8). This is expected, as the radius of curvature of magnetic field lines tends to scale with magnetic field magnitude in the magnetotail, meaning that the value of R_C, and thus K_i should be at a minimum in the neighborhood of $|B|_{min}$. Less expected is that the mean K_i is significantly greater than the median value across nearly the entire span. As the higher mean ion speed implied that occasional outlier events with much higher ion speeds occurred, likewise the higher mean K_i implies that occasional outlier events have much higher K_i and pull the overall average up. This suggests that at least one and possibly more events have a uniformly large K_i value that contradicts their identification as an IDR. One such event is discussed later.

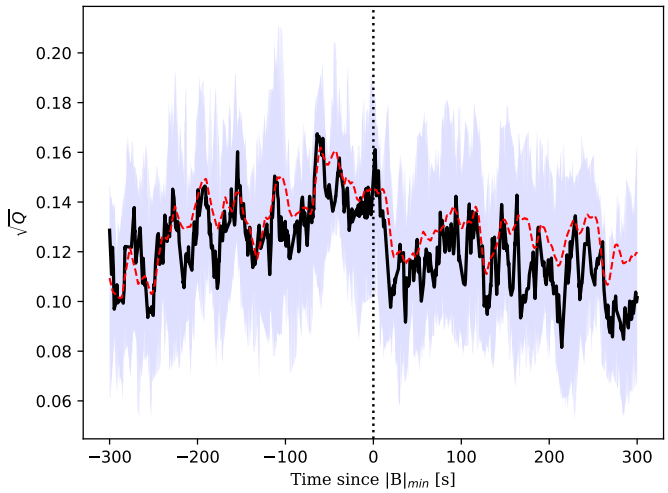

Figure 3.9: The superposed epoch analysis of the agyrotropy parameter $\sqrt{Q}$ for all IDRs listed in Table 2.2, in the style of Figure 3.6.

3.4.3 Statistical Phenomenology of $\sqrt{Q}$

The statistical values of ion agyrotropy as calculated using $\sqrt{Q}$ [Swisdak, 2016] for 10 minutes surrounding the IDRs listed previously are shown in Figure 3.9. Two characteristics are apparent which differ from the previous SEA plots shown: First, that the value is fairly constant across the span, the median varying only by a factor of two. This implies that there is a very narrow band of values over which $\sqrt{Q}$ varies within the plasma sheet and that even small variations may be significant, but perhaps difficult to distinguish. That the median and mean values are closely matched across the span (the mean being only slightly higher in places) reinforces this notion. The second clear characteristic is that there is a uniform drop in the value after $|B|_{min}$ in every respect. This is harder to interpret and, as of yet, no clear meaning has surfaced, although the influence of X-line motion is discussed later.

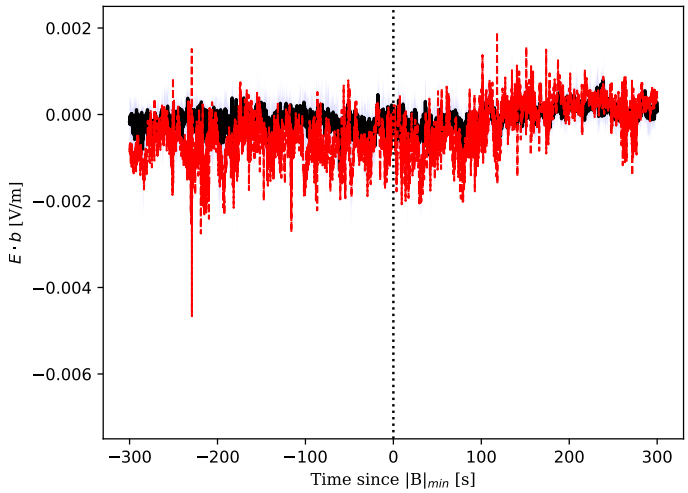

Figure 3.10: The superposed epoch analysis of the component of the electric field parallel to the magnetic field for all IDRs listed in Table 2.2, in the style of Figure 3.6.

3.4.4 Statistical Phenomenology of $E_{\parallel}$

The statistical values of $E_{\parallel}$ for 10 minutes surrounding the IDRs listed in Chapter 2 are shown in Figure 3.10. While plotting methods cause the median to be somewhat obscured by the lines of the mean parallel electric field, it is still reasonably obvious that the noise in both is greater than their DC values. Both show a roughly bipolar tendency, being more negative before the minimum magnetic field and more positive after, but little else can be derived. Like the sudden drop in $\sqrt{Q}$ at the magnetic field minimum, the reason for this broad tendency is not clear but may be related to the motion of reconnecting X-lines being tailward in the majority of IDRs observed by both MMS [Rogers et al., 2019a] and Cluster [Eastwood et al., 2010].

That both the median and mean values of $E_{\parallel}$ are close to zero could indicate that MMS did not observe any significant parallel electric field for a significant number of the IDRs identified in Chapter 2. One possible explanation for this is that parallel electric fields are only large in and near the EDR, but this seems unlikely in the face of observations like those

shown in Figure 3.4. Here strong DC parallel electric fields were present but the K value and even simple inspection of the magnetic field vector seem to contradict any possibility of being in or even near the EDR (see ∼12:01:15 UTC, Figure 3.4).

Instead, it is possible that $E_{\parallel}$ is being observed along the separatricies of the reconnection region. Electron streaming along the separatricies has been noted in both observations and simulations of Hall reconnection while similar ion streaming is much less pronounced [Øieroset et al., 2001, Cheng et al., 2016, Liu et al., 2019]. Charge separation will generate an electric field along the path of streaming electrons which, by nature of the separatrix, will be mostly parallel to the local magnetic field. This implies that while it could not be considered unreasonable that $E_{\parallel}$ is observed in the neighborhood of or inside an IDR, neither its presence nor its absence can be considered definitive for IDR identification.

3.4.5 Statistical Phenomenology of $\vec{j} \cdot \vec{E}$

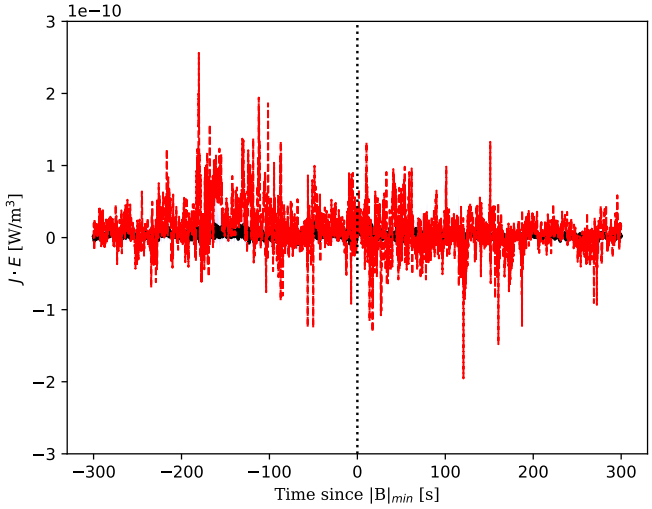

Figure 3.11: The superposed epoch analysis of the energy conversion rate $\vec{j} \cdot \vec{E}$ for all IDRs listed in Table 2.2, in the style of Figure 3.6.

The statistical values of the energy conversion rate are shown in Figure 3.11. As with the parallel electric field SEA, the median values of $\vec{j} \cdot \vec{E}$ are close to zero with any DC values

dwarfed by the noise-based uncertainty associated with it. The average value is somewhat different with DC values in excess of the noise both before and after the magnetic field minimum. As before, a bipolar asymmetry is weakly present with a trend towards positive $\vec{j} \cdot \vec{E}$ before $|B|_{min}$ and a neutral or slightly negative trend after. Due to the nature of the mean value, this trend may be attributable to a small number of IDRs or event a single event with large values. Again, as with $E_{\|}$, while a useful parameter for studying the physics and mechanics of a given event, neither the presence nor absence of $\vec{j} \cdot \vec{E}$ can be considered definitive for the purposes of identifying an IDR.

3.4.6 Statistical Phenomenology of $|\vec{j}|$

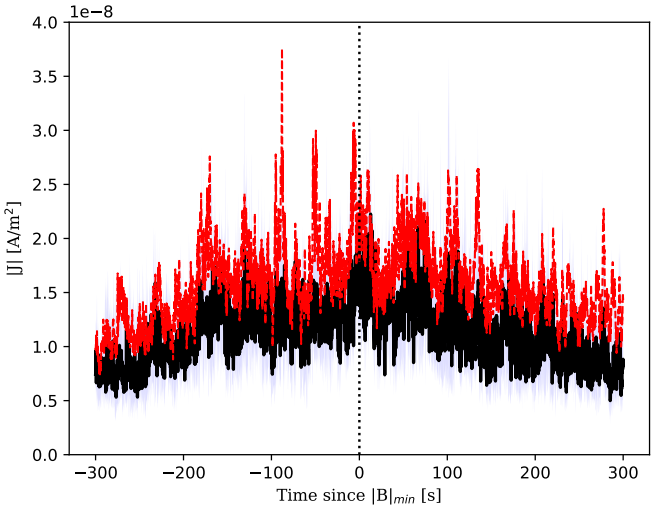

Figure 3.12: The superposed epoch analysis of the current density magnitude for all IDRs listed in Table 2.2 except Event 'B', in the style of Figure 3.6.

The statistical values of current density magnitude for all IDRs listed in Table 2.2, with the exception of Event 'B', are shown in Figure 3.12. As with Section 3.4.2, Event 'B' has been excluded as one of the four MMS observatories was not operational during this event, making calculation of the full gradient of the magnetic field impossible. As the current density used throughout this work is calculated by applying the Levi-Civita rotation tensor

to the magnetic field gradient tensor $\vec{j} = \epsilon_{ijk}(\nabla \vec{B})_{jk}$, essentially the curlometer technique, no current density suitable for statistical comparison in this fashion was available for event 'B'.

Unsurprisingly, the magnitude of the current density has a peak at the magnetic field minimum and generally drops off symmetrically to either side of that epoch. As $\vec{j} = \mu_0^{-1} \nabla \times \vec{B} = \mu_0^{-1} \epsilon_{ijk} \nabla \vec{B}$ the current density is expected to increase with the gradient of the magnetic field, which should itself find a maximum in the neighborhood of the $|B|_{min}$. The difference in median and mean values across the span is again easily understood as a small number of events with particularly strong current density. That the mean and median values behave essentially the same with only a fairly constant magnitude offset implies that either is reasonably representative of the behavior of the ensemble.

3.4.7 Statistical Phenomenology of $|\vec{E}|$

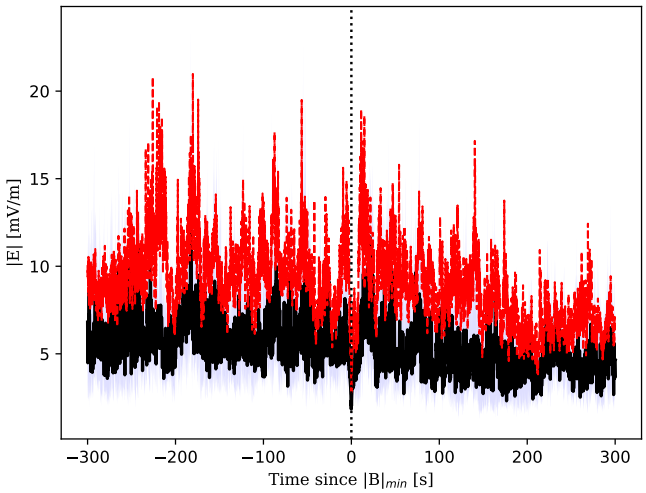

Figure 3.13: The superposed epoch analysis of the electric field magnitude for all IDRs listed in Table 2.2, in the style of Figure 3.6.

Statistical values of the electric field magnitude for all IDRs listed in Table 2.2 are show in Figure 3.13. Although noisy, the approximate values of both the mean and median $|E|$ are

fairly consistent across the span. As in most of the other parameters, the mean values tend to be larger than the median, representing occasional events with much larger magnitudes. The 2σ range of the median extending much further above the median than below reinforces this interpretation. Also as in other parameters, there is an asymmetry in values before and after the $|B|_{min}$ epoch with pre-epoch values generally higher than those post-epoch.

The most striking observation of these statistics, when viewed in light of the arguments made in Chapter 2 and those in the conclusions of Eastwood et al. (2010), is that the smoothed values of both the mean and median are not greatly in excess of $10mV/m$ across the span. This can be accounted for, however, by looking at examples of the events analyzed. While the algorithm requires that the electric field magnitude exceed $10mV/m$ in the neighborhood of the correlated field and flow reversal (being defined as within 90s), the precise location is not considered. As seen in Figure 3.4, the electric field enhancements are distributed across the region containing the IDR. While strong $|E|$ is found near the field and flow reversal in this example, it is also seen at other plasma sheet encounters previous to the primary current sheet crossing. In fact, many particularly large spikes in $|E|$ are found at crossings of the Plasma Sheet Boundary Layer (PSBL) where high speed ion flows and electric field enhancements have been observed without other evidence for nearby reconnection [Birn et al., 2020]. Given the large variability in the median and mean values across the span, the most likely explanation for the lower-than-expected smoothed value is that each event displays the large $|E|$ enhancements at very different locations in relation to the observed $|B|_{min}$, with the varying temporal locations of such observations being due, primarily, to the dynamic motion of the tail current sheet during most observed IDRs, rather than any intrinsic structural properties of the IDR itself.

Another interesting feature is the minimum of $|E|$ at $|B|_{min}$ (see Figure 3.14). This is most easily explained by consideration of the dominant source of the total electric field near the reconnecting current sheet. While the reconnection electric field parallel to the X-line

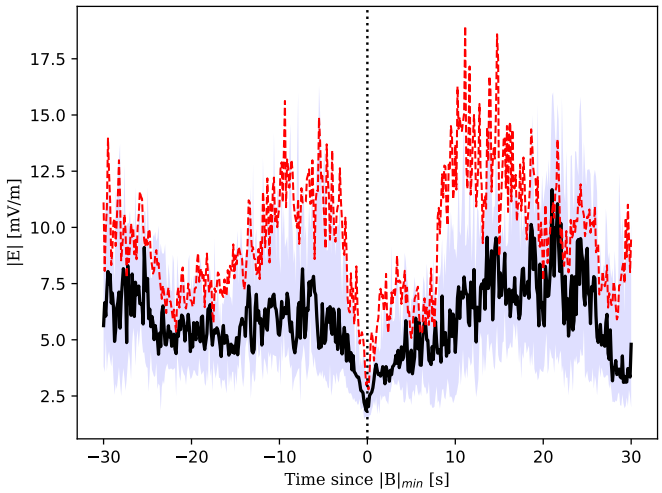

Figure 3.14: A detail of Figure 3.13 showing the central 60s.

tends to be of greatest interest due to it's relationship to the total energy conversion of the reconnecting current sheet or reconnection rate, the dominant component of the electric field in the IDR and EDR tends to be from the Hall effect; Hall electric fields typically dominate other electric field components by an order of magnitude or more in and near IDRs. However, as the measured Hall electric field reverses sign on opposing side of the current sheet, its contribution tends towards zero as the observer approaches the current sheet and its associated minimum in the magnetic field strength. The remaining electric field magnitude at $|B|_{min}$ of $\sim 2mV/m$ will be the statistically typical remaining total electric field without the Hall contribution. As a single anecdotal example, Genestreti et al. [2018] determined the reconnection electric field to be $3.2 \pm 0.6mV/m$ for event 'E' on Table 2.2, suggesting the reconnection electric field (perpendicular to the Hall electric field in the out-of-plane direction) is likely a significant source of the remaining $|E|$ at the magnetic field minimum.

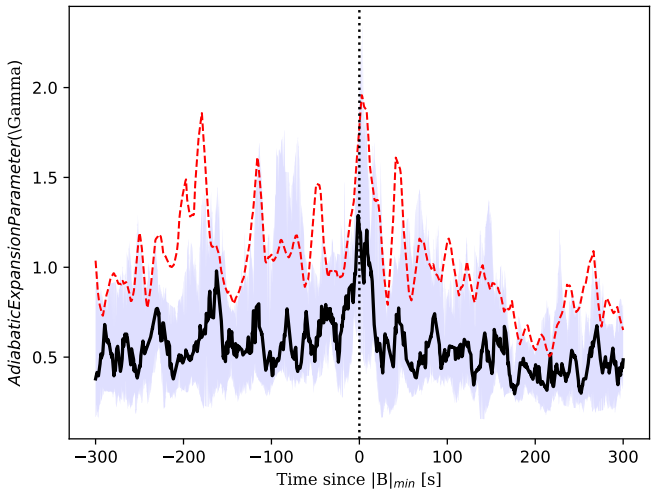

Figure 3.15: The superposed epoch analysis of the Lorentz ratio for all IDRs listed in Table 2.2, in the style of Figure 3.6.

3.4.8 Statistical Phenomenology of Γ

Statistical values of the Lorentz Ratio Γ for all IDRs listed in Table 2.2 are shown in Figure 3.15. As the Lorentz Ratio is inversely proportional to $|B|$ it is unsurprising that the maximum value of both the median and mean values is at the $|B|_{min}$. The significantly higher mean value of Γ relative to the median is easily explained, as with other parameters, as there being some small number of events which have an overall much higher value, thus drawing up the mean. There is again an asymmetry before and after the $|B|_{min}$ with higher mean and median values before than after. Also, as has been noted with some other parameters, there is a spike in values at $\sim$ 3.5minutes before the common epoch. Encounters with the separatrix such as those noted in Event 'T' occurring at approximately the same distance from the magnetic minimum is one plausible explanation, as parallel electric fields along the separatricies may exert immediate local influence greater than the magnetic field. Additional investigation into this correlation is necessary before any conclusions regarding IDR structure can be made from this feature.

3.4.9 Statistical Phenomenology of T_i

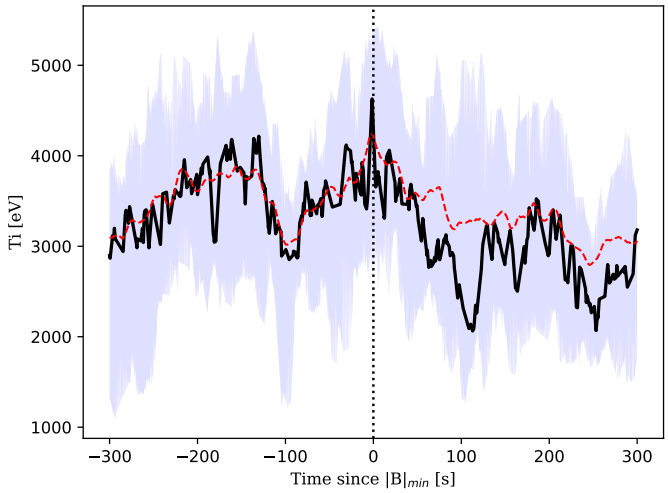

Figure 3.16: The superposed epoch analysis of the ion temperature for all IDRs listed in Table 2.2, in the style of Figure 3.6.

Statistical values of the ion temperature T_i as derived from the trace of the temperature tensor for all IDRs listed in Table 2.2 are shown in Figure 3.16. The mean and median values are in much better agreement across the span for this parameter than for many of the others analysed here. It is somewhat surprising that both the median and mean values are approximately the value expected for the tail central plasma sheet in general of $4200eV$ [Kivelson and Russell, 1995] and do not show any outstanding signs of ion heating from that baseline. However, as with the discussion of bulk ion speed, this may be in part due to the limitations of the FPI instrument not sufficiently sampling the full ion energy distribution. When compared to the average tail plasma sheet ion temperature of $\sim 1800eV$ measured by MMS over the 2017–2020 tail seasons, the case for ion heating having been observed by MMS becomes much stronger.

The occasional very low excursions in both the median and 2σ range are another sign of frequent dynamic motion of the tail current sheet during IDR events; they likely represent

excursions to the PSBL or even tail lobe regions by the MMS observatories as the tail current sheet flaps and twists during times of geomagnetic activity.

3.4.10 Summary: Viability of Scalar Parameters for IDR Identification

Looking at the statistical behavior of the various proposed scalar parameters near known IDRs, while keeping in mind the currently limited data set, a sense can be formed for each parameter's utility in possible identification of as-yet unknown IDRs. The theoretical threshold values of the K_i and Γ parameters of below or above unity respectively appear to be very valid for identification, and especially for identifying which current sheet crossings are most likely to be encounters with a reconnecting current sheet. Increases in the electric field magnitude as suggested by Eastwood et al. appear to be reasonable but are less selective than K or Γ. The same can be said of $\sqrt{Q}$ where the value near reconnection sites is certainly enhanced above the tail average of ~ 0.04 but, much like an enhanced current density or ion temperature, is only an indication that ion energization is somewhere nearby without greater specificity. The parallel electric field and energy conversion rate $\vec{j} \cdot \vec{E}$ are both of limited utility in screening for reconnection, in no small part because the statistical noise in measurement is so close to the values of a meaningful signal. While valuable, they should be reserved for the careful analysis which follows identification.

Ion velocity is a different case than the others. Due to the difficulties in calculating accurate moments of the ion energy distribution, precise thresholds relating to theoretical parameters such as the Walen relation are of dubious dependability in IDR identification. However, the analysis here shows that ion bulk velocities are typically in excess of $200 km/s$, at least a factor of two higher than the average ion speed measured by MMS in the tail of $\sim 100 km/s$. That said, ions in the tail often travel significant distances away from the X-line in the form of Bursty Bulk Flows and dipolarization fronts [Runov et al., 2012], making enhanced ion speed perhaps a common, but certainly insufficient parameter for IDR

identification.

On the basis of this analysis, the most promising parameters for IDR identification are K_i and Γ_i with agyrotropy in the form of $\sqrt{Q_i}$, current density magnitude, electric field magnitude, and ion temperature possibly providing supporting evidence. $\vec{j} \cdot \vec{E}$, $E_{\parallel}$, and ion speed are probably not to be trusted for identification, although they are useful parameters for investigating the physics and structure of individual events.

3.5 One That Got Away: June 17, 2017

The primary motivation for investigating scalar parameters has been to find a means of identifying an IDR without depending on the correct identification of the boundary normal coordinate system. In Figure 3.17 we can see how our chosen scalar parameters might fare at identifying an event which was missed by the algorithm method of Chapter 2. Here we see the K_i and Γ_i parameters peak strongly at the relevant current sheet crossing, both with values which satisfy the theoretical criteria associated with each, as well as exceeding the typical values shown in Section 3.4 for an IDR. The electric field magnitude is larger than the background level, although still comfortably in the range of most other IDRs. Similarly the ion temperature and flow speeds are in excess of the expected background levels, based on MMS measurements, indicating ion heating and acceleration, but not by an extraordinary amount and offset from the current sheet crossing itself. Still, the totality of the ion-specific scalar parameters provides ample evidence of ion demagnetization and energization, indicative of the Ion Diffusion region [Farrugia et al., 2021].

Looking at the additional parameters for the sake of completeness, $|\vec{j}|$ is very large, likely due to the strong twisting occurring in the magnetic field at the current sheet. $\vec{j} \cdot \vec{E}$ and $E_{\parallel}$ are both very large for this event and, being large at the current sheet, support the interpretation that MMS encountered the EDR at the current sheet crossing [Huang et al., 2018, Farrugia et al., 2021]. These parameters, as stated before, are invaluable for analyzing

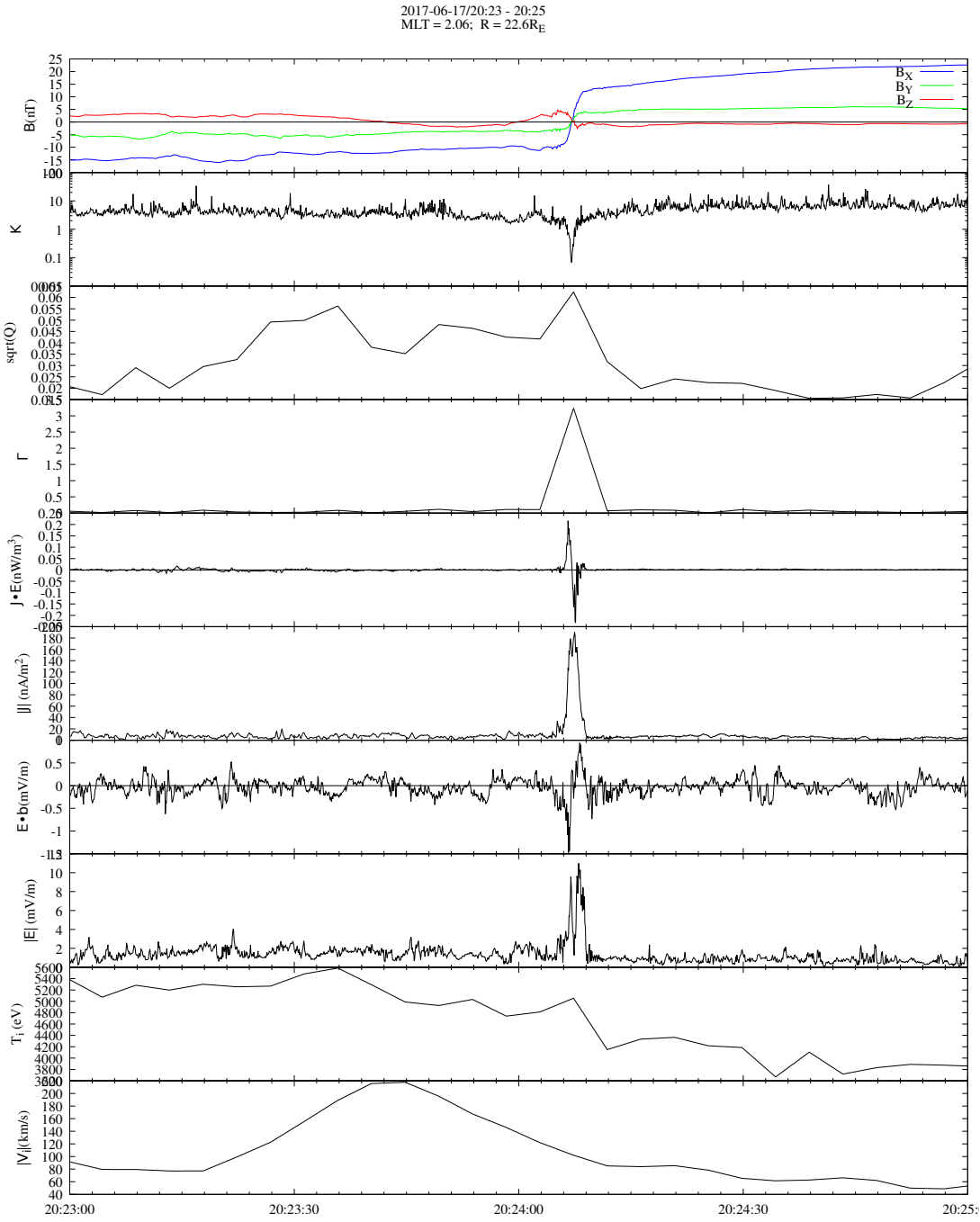

Figure 3.17: The scalar parameters discussed in this chapter calculated for the June 17, 2017 event in the style of Figure 3.4. See text for details.

and characterizing the event as a specific example, but were not critical for the identification as a likely IDR.

Based on the SEA shown in Section 3.4, it is somewhat surprising that the scalar parameters have so clearly indicated that this event is, indeed, an IDR and localized so precisely on the current sheet crossing at 20:24 UTC. Even looking at the previous example of known IDR 'T' there was significantly more 'signal', so to speak, at each of the PSBL and current sheet encounters on either side of the X-line. But perhaps those other nearby current sheet encounters are the answer. Many of the IDRs identified in Chapter 2 are located within very active current sheets where MMS observes several encounters with the central tail current sheet in the neighborhood of the X-line (see Section 2.3). This event is an example of a fleeting encounter with the central current sheet during a period of intense tail flapping, allowing only the one, fortuitous look at the reconnection region before global tail motion and the typical tailward convection of an X-line moved it beyond the ability of MMS to observe it. By only having a single, relatively clean current sheet encounter which happened to coincide with an active X-line, the relative signal-to-noise ratio was increased, making identification certain.

3.6 Putting It Together

Having looked at the behavior and relative usefulness of various scalar parameters on a known, previously identified IDR, at the statistical behavior across many IDRs, and on a additional IDR which had not been identified in the same manner as the others, the next step is to try to identify new IDRs using the scalar parameters. In Section 3.4.10 the parameters suggested as most likely to locate an IDR (or at least the current sheet crossing within an IDR) were K_i and Γ_i. These were applied to the 2017 tail season data in an initial effort find new IDRs [Rogers et al., 2019b]. Threshold values for the parameters below were selected based on a combination of the theoretical boundary envisioned in each parameter's

formulation as well as the statistical behavior discussed previously. In each case the threshold value was intended to be stringent enough to exclude quiet, non-active regions while allowing sufficient grace to reasonably contain the median and mean values across the known IDRs.

3.6.1 K_i in 2017

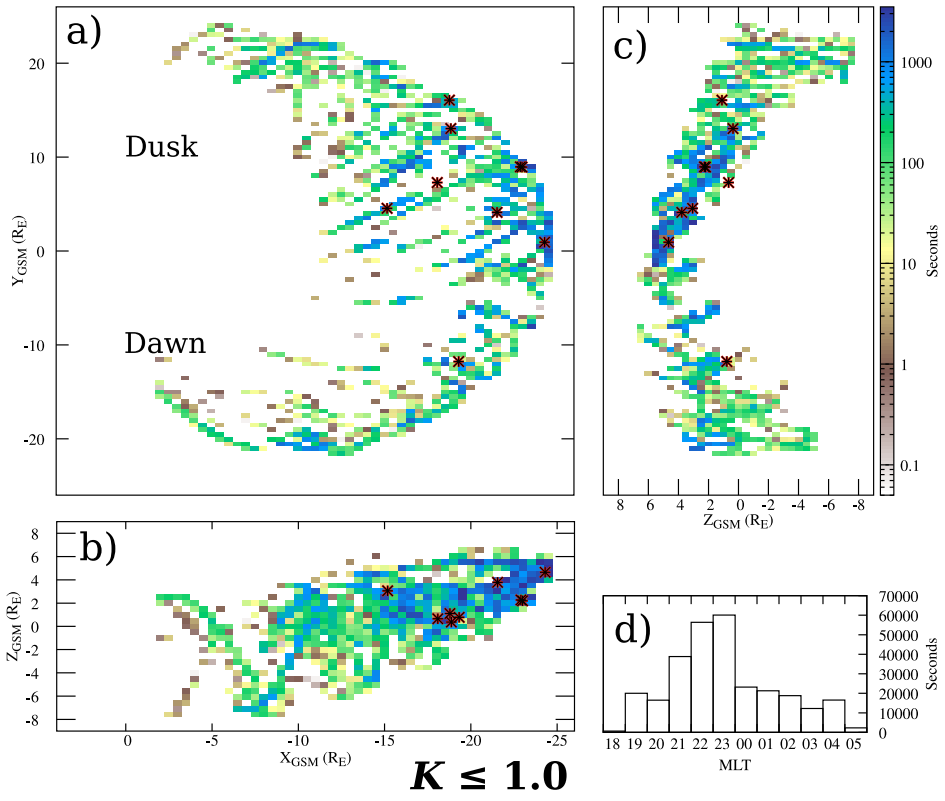

Figure 3.18: A map of the amount of time MMS spent in regions where $K_i \leq 1$. The amount of time MMS spent in such a condition is given by the color bar. *a)* shows a $X - Y_{GSM}$ projection of the data; *b)* shows a $X - Z_{GSM}$ projection; *c)* shows a $Z - Y_{GSM}$ projection. *d)* shows the distribution of MMS dwell time with $K_i \leq 1$ in MLT. Stars show the positions of IDRs identified during the 2017 tail season.

First, looking only at the K_i parameter in Figure 3.18, a large spatial section of the tail on the dawn-side of midnight is apparently devoid of possible IDRs. This is supported by the distribution of IDRs identified previously in Chapter 2, which showed a very strong dusk-side preference. The significant dwell time present along the outer rim of the figure

is most easily explained by orbital mechanics; that is, the MMS observatories were at their lowest velocities and consequently spent the most time at the apogee (*i.e.* most distant point from the Earth) of each orbit, as shown in Figure 2.1. That said, there still remain dozens of hours worth of data which, only considering K_i, may contain an IDR. Perhaps Γ_i will do better.

3.6.2 Γ_i in 2017

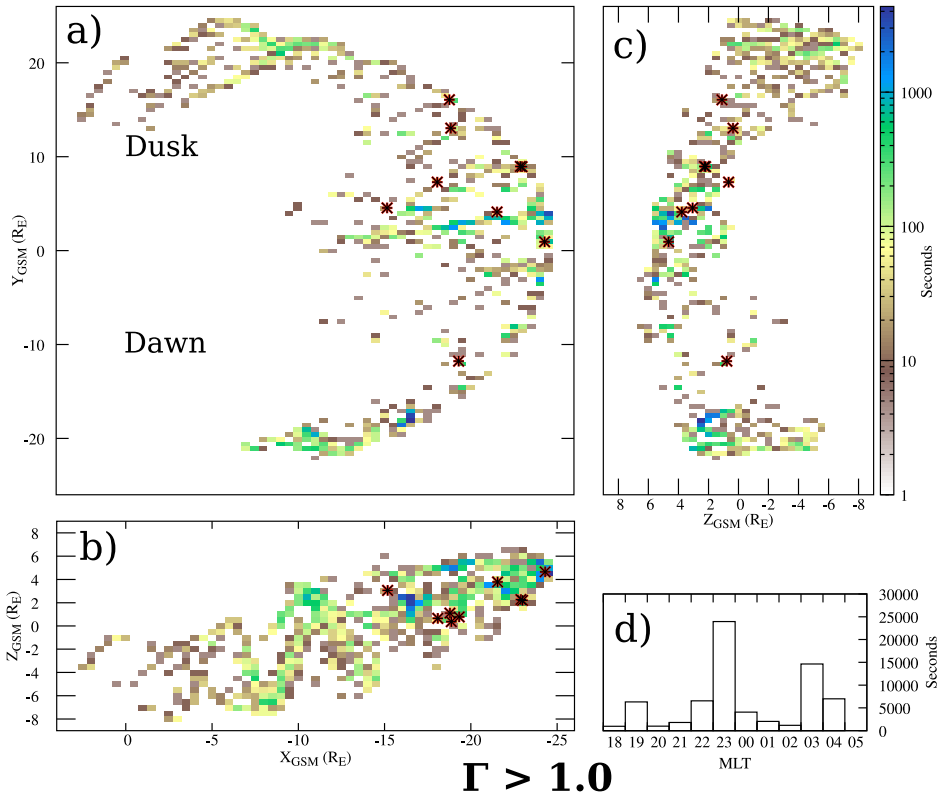

Figure 3.19: A map of the amount of time MMS spent in regions where $\Gamma_i > 1$ in the style of Figure 3.18.

The Γ_i parameter, shown in Figure 3.19, appears to be much more selective at first glance. Similar biases towards the apogee of each orbit are still present, as expected, but the total amount of data indicated here is only on the order of 10 hours. Interestingly, there seems to

be a strong concentration of likely candidates along the midnight line. Possible explanations for this are discussed in Chapter 4.

So far these two parameters have done a reasonable job of limiting the time spans and locations where IDRs might be expected. However, even combined they still leave several hours of possibilities. An additional parameter, perhaps one focused more on the particle moments than K_i and Γ_i, may provide better selectivity.

3.6.3 $\sqrt{Q}$ in 2017

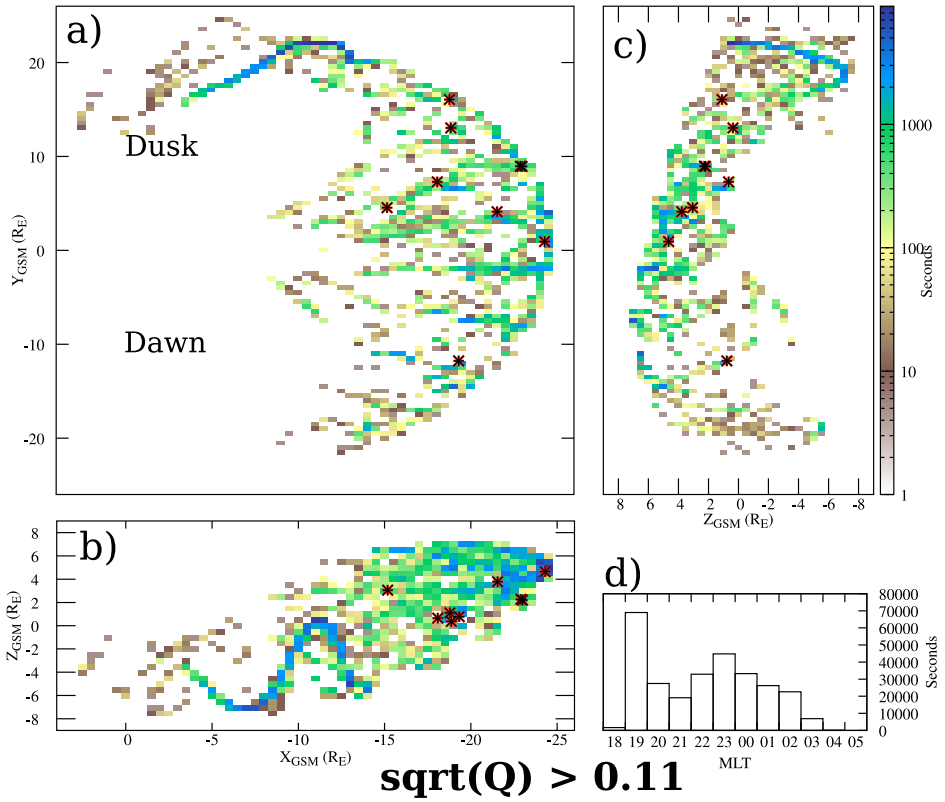

Figure 3.20: A map of the amount of time MMS spent in regions where $\sqrt{Q_i} > 0.11$ in the style of Figure 3.18.

On inspection, the $\sqrt{Q_i}$ map appears to be a middle ground of selectivity between K_i and Γ_i. A strong feature visible on the dusk flank is the result of a single orbit, discussed

later. Excluding that orbit, $\sqrt{Q_i}$ appears of greater selectivity in terms of extent but greater 'saturation;' that is, the threshold value is met in fewer locations than, for example K_i, but for longer periods of time in each location. This is not surprising in view of the behavior of $\sqrt{Q_i}$ across the known IDRs shown in Section 3.4.3, but it alone would still implicate dozens of hours of data.

3.6.4 A Combined Filter

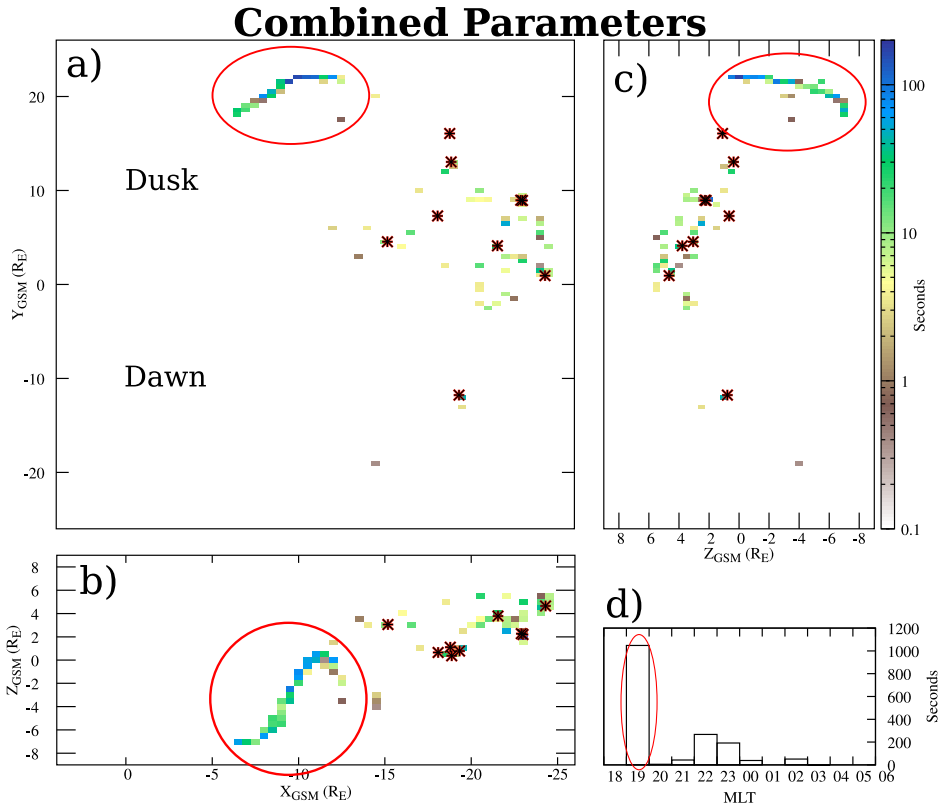

Figure 3.21: A map of the time MMS spent in regions which satisfied all the conditions $K_i \leq 1.0$, $\Gamma_i > 1.0$, and $\sqrt{Q_i} > 0.11$ after the style of Figure 3.18.

By requiring all three conditions be true, the map becomes very selective indeed. The single orbit mentioned in Section 3.6.3 is part of a nearly six hour flank magnetopause encounter during a CME encounter with strong indications of Kelvin-Helholtz (KH) waves

present, which often support reconnection both between KH waves and to the IMF and solar wind. Excluding this orbit, only a few minutes worth of data remain for investigation. That said, those few minutes represent several dozen separate events, as there are typically only a few seconds in each event where all three criteria are satisfied. When this analysis is extended across the four tail seasons from 2017–2020 a total of 578 possible events are found. While clearly a victory for data reduction, it is not yet sufficient for practical analysis by eye.

The magnetopause encounter mentioned above reinforces a key benefit of using scalar parameters for identification and analysis: That they are equally applicable to the different regimes in and near the magnetosphere where reconnection may be found. Additional parameters may be used to limit the regions sampled by this technique such as location or plasma density. Even reconnection events from different regions and initial conditions, once analyzed using scalar parameters, can be easily compared to highlight differences and commonalities caused by differing contexts and initial conditions.

Also a point worth reiteration is the value which each parameter may alone contribute to analysis in a broader scope. The K parameter, for example, is fundamentally a ratio of the length scales of the particle distribution and magnetic field topology, both broad and powerful conceptual frameworks which are distilled into a scalar comparison. With careful application, K can be used to probe either the magnetic field topology, the morphology of the plasma distribution, or both. An example of this sort of application and the broader physical context it illuminates is the subject of Chapter 4.

CHAPTER 4

Thin Current Sheet and IDR Distribution in the Magnetotail

4.1 Introduction

The Ion Diffusion Region (IDR) distribution of Chapter 2 was not the first instance of observed dawn-dusk asymmetries related to magnetic reconnection in the tail. Related phenomena such as auroral substorms, dipolarization fronts, and bursty-bulk flows (BBFs) have historically also shown a strong asymmetry in their dawn-dusk distribution, in all cases being more common on the dusk-side of midnight by significant margins [Nagai et al., 1998, 2001, Posch et al., 2007, Xiao et al., 2017]. A statistical study of active tail current sheet phenomena using data from the THEMIS mission [Sibeck and Angelopoulos, 2008] was performed by Imber et al. (2011) and showed that 81% of magnetic flux ropes and travelling compression regions associated with the distant outflow of reconnection in the tail were found in the dusk sector. This is in addition to MMS observations discussed in Chapter 2 where 21 out of 26 IDRs encountered by MMS were on the dusk-side of midnight while only 5 were dawnward of midnight, despite nearly equal time spent in or near the central plasma sheet on either side of midnight. This all combines to suggest that the observed asymmetries in reconnection-related phenomena are due to the underlying physical processes and not observational bias.

The common thread throughout all theories of magnetic reconnection is an initial condition of a thin current sheet between opposing magnetic fields (see Figures 1.5 and 1.6). Various simulations have suggested the maximum current sheet thickness which would sup-

port reconnection onset is between several ion inertial lengths [Birn, 1980] and two electron inertial lengths [Liu et al., 2020] depending on the exact instability which instigates reconnection onset. Despite the continuing debate over the precise onset mechanism, it would seem that a central current sheet of thickness in the range of the ion gyroradius or smaller is a necessary precondition for magnetic reconnection in the tail. Thus the distribution of ion-scale current sheets within the central tail plasma sheet is pertinent to the question of reconnection location in the tail by way of identifying where reconnection is even possible.

Attempts to estimate the thickness of the tail current sheet have occasionally been made using single-spacecraft measurement techniques (*e.g.* [Artemyev et al., 2011, Lu et al., 2019]). Many of these techniques relied on a ratio of measurements of the magnetic field and particle current density; often with a significant time separation between these two measurements. This assumes that the current sheet being measured is essentially a quiet, Harris-type current sheet [Harris, 1962], *i.e.* an infinitely long current sheet with uniform thickness and geometry, throughout the measurement period. However, reconnection and related substorm phenomena often occur during times of a disturbed geomagnetic field, violating the Harris current sheet assumption.

Rong et al. (2011) utilized the four spacecraft of the Cluster mission in tetrahedral formation to calculate the radius of curvature (R_C) of the magnetic field at the barycentre of the fleet:

$$R_C = \frac{1}{|(\hat{b} \cdot \nabla)\hat{b}|} \tag{4.1}$$

where $\hat{b}$ is the unit vector $\vec{B}/|\vec{B}|$ (see Chapter 3). They then estimated the half-thickness of the neutral sheet by scaling the radius of curvature by the current sheet tilt angle $h = R_C \cos(\theta)$ where $\theta \approx \arctan(B_y/B_z)$, implying that $2R_C$ measured within the plasma sheet is a maximum estimate for the thickness of the neutral sheet [Shen et al., 2008, Rong et al., 2010,

2011]. This method was superior to previous estimates using single-spacecraft techniques. A statistically significant dawn-dusk asymmetry in current sheets thinner than $1000km$ ($\sim$ an ion gyroradius in the tail plasma sheet) was found, with thinner current sheets more common duskward of midnight. However, due to the nature of its near-polar orbit, Cluster only sampled the current sheet at a radial distance of approximately 20 Earth Radii (R_E) from the Earth within a narrow band $\approx 2R_E$ wide. Current sheet thickness in the geomagnetic tail has not been explored using such robust techniques at other radial distances before Rogers et al. (2022).

The mechanism for current sheet thinning has also been explored in simulations. Hybrid and Particle-In-Cell (PIC) simulations [Lu et al., 2016, 2018] suggest that external drivers cause a global compression of the tail current sheet to approximately ion scales, at which point partial demagnetization of ions drives charge separation from the still frozen-in electrons, leading to Hall electric fields, although not necessarily reconnection. These demagnetized particles then move dawnward under $\vec{E} \times \vec{B}$ drifting (see Figure 4.1), partially evacuating ions from the duskside and leading to even greater dawnward flow under diamagentic drift. This has the effect of progressive thinning of the current sheet pre-midnight towards the dusk flank. These simulations suggest the asymmetric thinning should be robust across a broad range of radial distances.

I utilized a technique particularly suited to the capabilities of MMS and tailored to identify current sheets which may be preferentially thinned as suggested by simulations. As discussed in Section 3.2.2, Büchner and Zelenyi (1986,1989) describe a mechanism for demagnetizing charged particles near a strong gradient in the magnetic field by testing violations of the first adiabatic invariant. They offer the ratio of particle gyroradius to magnetic field line curvature as a scalar indicator of non-adiabatic motion of particles, and

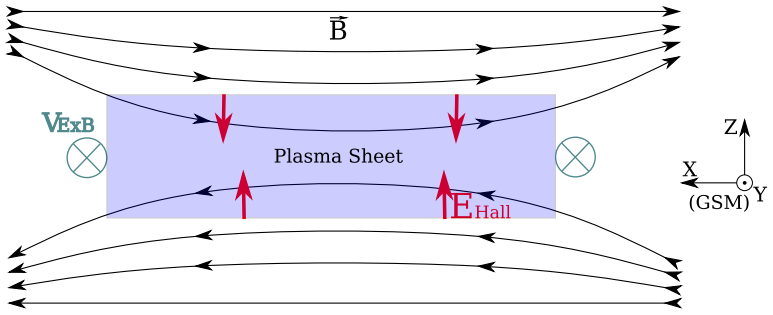

Figure 4.1: A schematic of a section of tail current sheet with thickness of ion-scale aligned with GSM coordinates. Heavy and super-thermal ions may demagnetize even when the bulk of the plasma population remains frozen-in. Once demagnetized, they will cause a weak Hall electric field due to charge separation from the electron population (red arrows). The $\vec{E} \times \vec{B}$ drift will accelerate the demagnetized particles (and the bulk plasma to a lesser extent) in the $-\hat{y}$ direction (*i.e.* dawnward, sea-green).

thus an indicator of demagnetization of charged particles. Applying this ratio K to ions:

$$K_i = \sqrt{\frac{R_C}{\rho_{g,i}}} \quad (4.2)$$

where $\rho_{g,i} = \frac{\sqrt{2m_i T_{\perp,i} k_b}}{q_i |\vec{B}|}$ is the thermal ion gyroradius. Where $K_i < 1$ the gyroradius of the thermal average ion is larger than the radius of curvature of the local magnetic field, implying that the majority of ions will encounter multiple guiding centers during a single gyroperiod, incompatible with adiabatic motion. The degree of chaotic motion increases with decreasing values of K until ions become functionally demagnetized for values of $K_i < 0.2$ [Büchner and Zelenyi, 1989]. Any degree of non-adiabatic motion ($K_i < 3$) will lead to charge separation and the formation of Hall electric fields and the process described by Lu et al.

The same $K_i < 1$ condition, indicating that the thermal mean gyroradius is smaller

than the half-thickness of the tail current sheet, is also indicative of a reasonable maximum current sheet thickness that might support magnetic reconnection. Therefore a map of the geomagnetic tail indicating regions where $K_i < 1$ will show what regions are most likely to support reconnection. Using data from the 2017–2020 MMS tail seasons and leveraging the regular tetrahedral formation of MMS along with the high-resolution magnetometers on board, the radius of curvature of magnetic field lines can be calculated and compared to the ion thermal gyroradius to calculate K_i throughout the tail central plasma sheet (see Figure 2.1).

4.2 Methodology and Software

The high-resolution plasma (FPI) and magnetic field (FGM) instruments on board MMS [Pollock et al., 2016, Russell et al., 2016] allow for the calculation of K at high time cadence. The ion thermal gyroradius $\rho_{g,i}$ is easily calculated using the mean values of $T_\perp$ and $|\vec{B}|$ across all four spacecraft of the MMS fleet. The calculation of R_C is less straightforward and was accomplished using the `mms-curvature` python library [Rogers and Rogers, 2022]. The development of this library is discussed more in Chapter 3 and Appendix A. Analysis was completed using automated scripts written in python and run on a server generously provided by Zach Dykstra.

4.3 Observations and Analysis

Figure 4.2 shows the distribution of ion-scale thin current sheets as measured by MMS over the combined 2017–2020 tail seasons where data from all four MMS spacecraft were available ($\approx$ 550 days of data). Colors represent the amount of time which MMS spent in each region with a value of $K_i < 1.0$, *i.e.* the dwell time of MMS in a current sheet thinner than an ion gyroradius at the time. The effects of orbital or observational bias on these dwell time

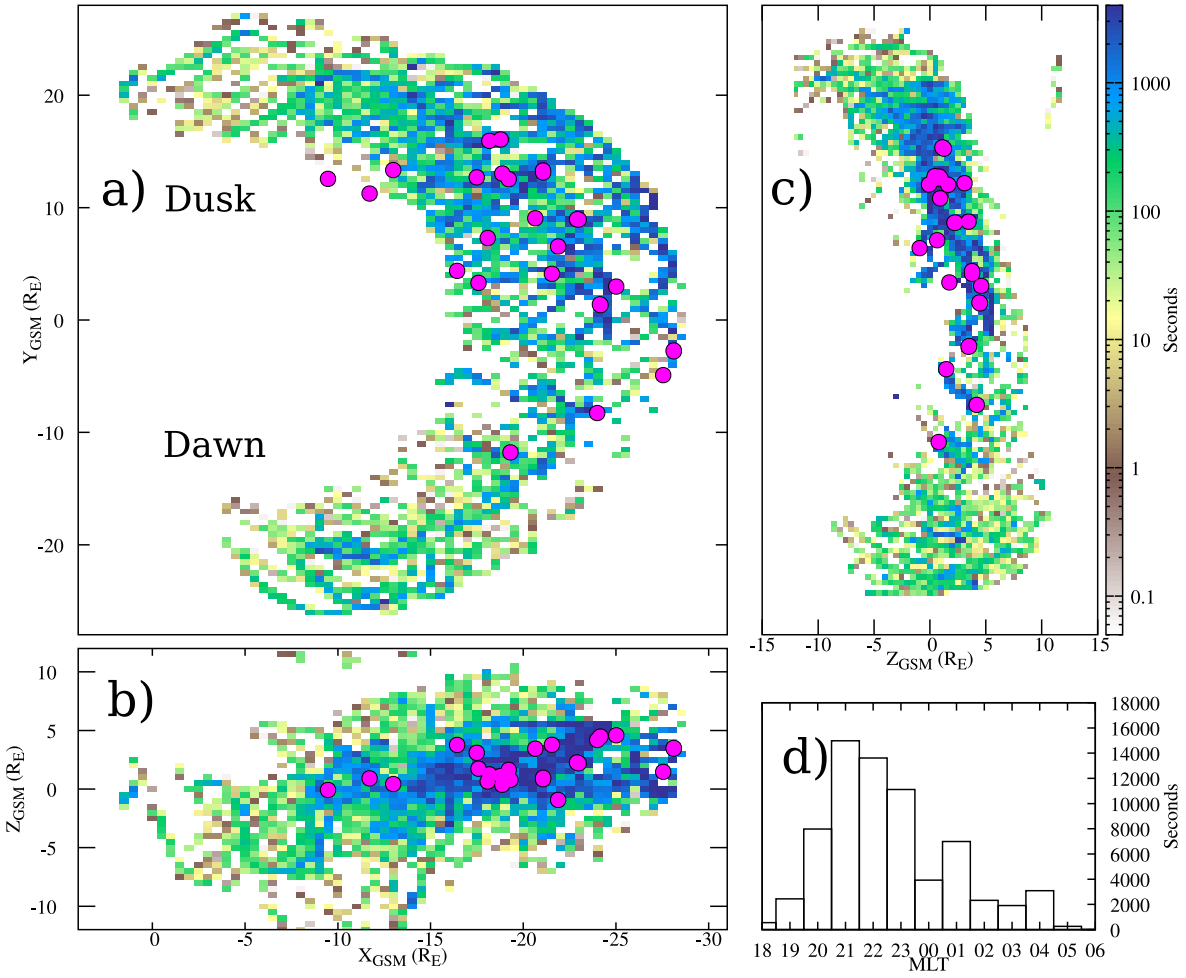

Figure 4.2: The total amount of time in seconds spent by MMS in a TCS, under conditions outlined in the text, in sectors of dimension $0.5R_E \times 0.5R_E$ (*a, b, c*) and Magnetic Local Time (MLT) (*d*). *a)* Distribution of TCS dwell times in the GSM X–Y plane, with times summed over the GSM Z axis. *b)* TCS dwell times in the GSM X –Z plane, with times summed over the GSM Y axis. *c)* TCS dwell times in the GSM Z – Y plane, with times summed over the GSM X axis. *d)* TCS dwell times across all radial distances by MLT location. Magenta circles represent Ion Diffusion Region locations (see text)

measurements are small as MMS spent approximately equal time in the central plasma sheet on either side of midnight (51.7% pre-midnight, 48.3% post-midnight) as discussed in Section 2.5 and shown in Figure 2.15. IDRs identified in Chapter 2 are also shown as an overlay of magenta circles on the thin current sheet (TCS) distribution in Figure 4.2. It should be noted that some IDR markers in Figure 4.2 and following figures totally obscure the dwell time indicator for the region where they are located.

Figure 4.2*d* shows the total TCS dwell time as a function of Magnetic Local Time (MLT). This subfigure is comparable with similar plots showing the global MLT distribution of other substorm-related phenomena such as Pi1B pulsations [Posch et al., 2007] and dipolarization fronts [Xiao et al., 2017], all of which show a strong preference for activity duskward of midnight.

Figure 4.3 shows the same TCS data derived from the parameter K_i but here normalized by the total dwell time MMS spent in the tail plasma sheet, as indicated by the measured ion number density $n_i > 0.05cc^{-1}$ (see Section 2.2). As expected, the majority of time spent by MMS in the tail plasma sheet was not near an ion-scale TCS, as indicated by the bulk of the distribution showing a ratio of TCS dwell time to plasma sheet dwell time of much less than one. The distribution of IDRs is again laid over the normalized dwell time map as it was in Figure 4.2.

The total time spent in a TCS is significantly higher on the pre-midnight side of the tail (187hrs) than the post-midnight (77.68hrs) as shown in Figure 4.2d. While MMS spend an approximately equal amount of time in the plasma sheet in both the pre- and post-midnight sectors (51.7%/48.3%), this contrasts with the *un*even amount of time spent in a TCS by MMS; 70.7% of total time in TCSs was in the pre-midnight sector versus 29.3% post-midnight; *i.e.* far greater time was spent in a TCS on the duskside of midnight than the dawnside. The same calculations using the much more restrictive threshold of $K_i < 0.2$ [Büchner and Zelenyi, 1989] show qualitatively similar results with 78.9% of total TCS dwell

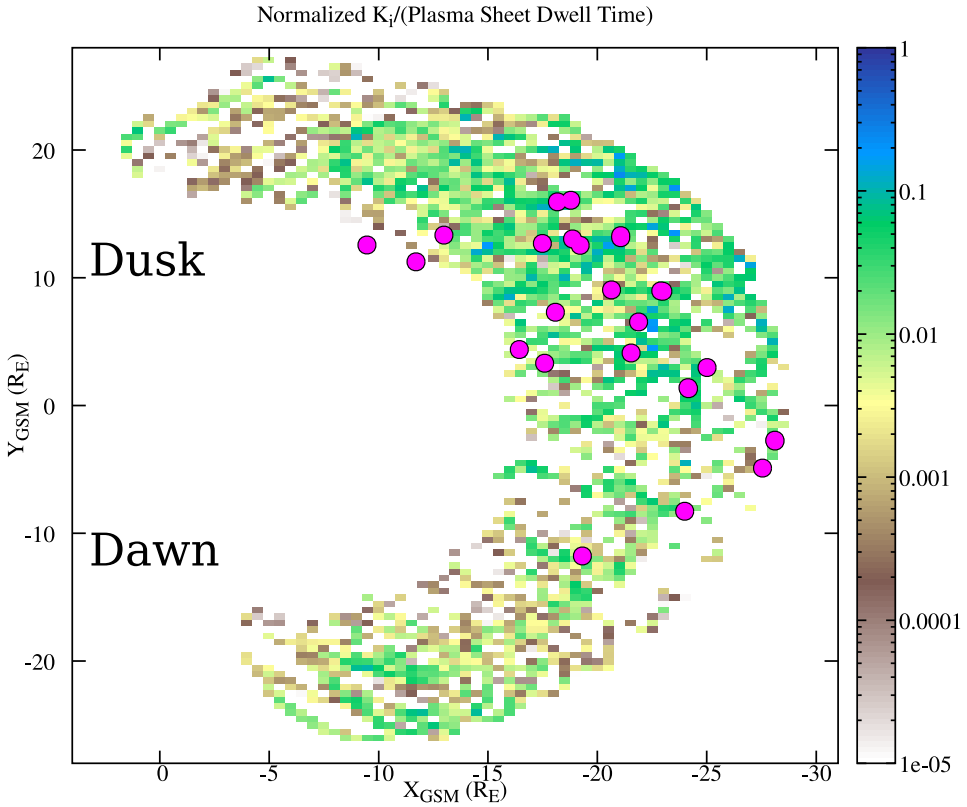

Figure 4.3: Dwell time MMS spent in a TCS normalized by the amount of time MMS spent in the plasma sheet. Regions and projection are in the style of Figure 4.2.

time duskward of midnight and 21.1% dawnward of midnight and similar extent in radial distance (see Figure 4.4).

The majority of time spent in a TCS on the post-midnight side is found near apogee across all seasons (see Figure 4.2) where spacecraft velocity was the lowest and the bulk of dwell time was spent each orbit regardless of other factors. The distribution of time spent in a TCS pre-midnight is far more varied in radial distance and is not confined to the apogee of each orbit. Figure 4.5 shows the TCS dwell time of MMS as a function of MLT in bands of radial distance from the Earth, each $2R_E$ wide. The center of the relative TCS dwell time at smaller radial distances (Figure 4.5*a,b*) is substantially duskward of midnight at $\sim$ 21MLT. The distribution broadens towards midnight as radial distance increases (Figure 4.5*c,d*), although the peak remains near 21MLT. Large relative TCS dwell times at the dawn and dusk flanks are interpreted as encounters with the flank magnetopause where current sheets and increased ion density are expected. Figure 4.5c represents the approximate region of the geomagnetic tail sampled by Cluster as in Rong et al. (2011).

The asymmetry in the locations of IDRs (magenta circles Figures 4.2 and 4.3) associated with magnetic reconnection is even more pronounced than that of relative TCS dwell time. 21 IDRs were confidently identified across all four tail seasons analyzed on the dusk-side of midnight, while only five were observed on the dawn-side, equating to 80.8% of reconnection event observed duskward of midnight and 19.2% dawnward. In Figure 4.3 we see that the majority of identified IDRs lie not only in areas where MMS spent a great deal of time in ion-scale TCSs, but also where the ration of TCS dwell time to total plasma sheet dwell time was the greatest. This supports the intuitive interpretation that an ion-scale or thinner current sheet is more likely to support reconnection, and that reconnection is more likely where thin current sheets are more common (see also [Liu et al., 2014, 2019]). However, the long periods of time spent in both the plasma sheet and thin current sheet where no reconnection was observed, such as $-16R_E\hat{x}, 11R_E\hat{y}$ in Figure 4.3, indicate that an ion-scale

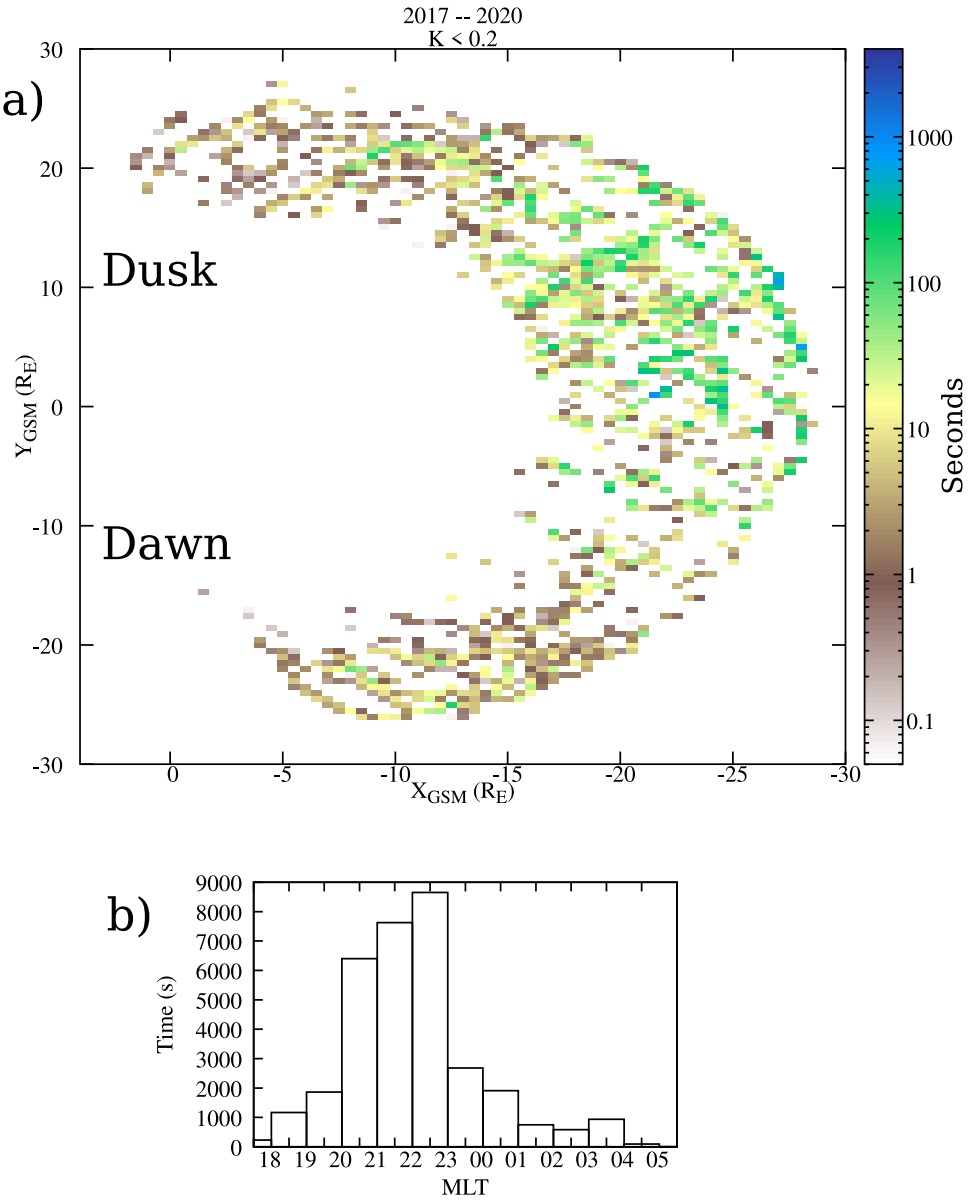

Figure 4.4: *a)* TCS distribution where $K_i < 0.2$ in the style of Figure 4.2a. *b)* The same distribution displayed as a function of MLT in the style of Figure 4.2d. While a more restrictive condition, the distribution does not qualitatively differ from that where $K_i < 1.0$.

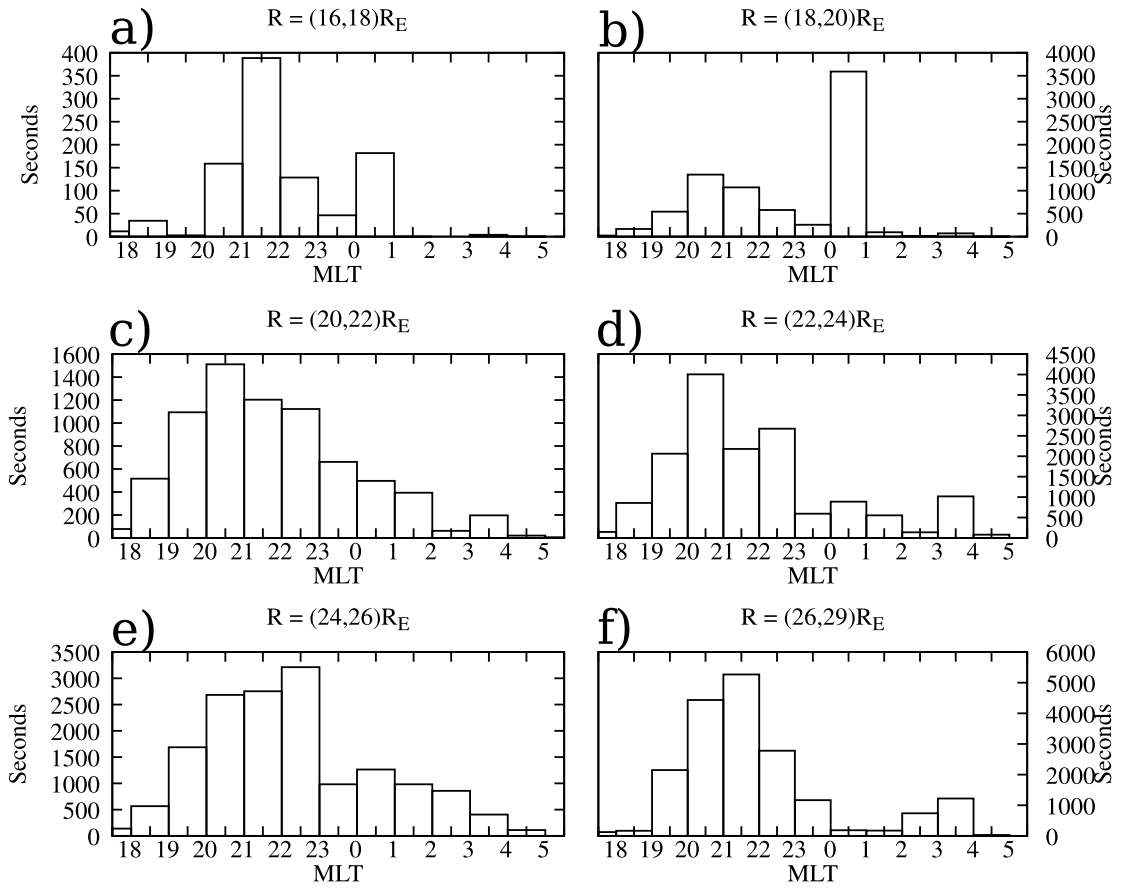

Figure 4.5: Dwell time MMS spent in a TCS by MLT for narrow ($2R_E$ wide) bands across the geomagnetic tail, normalized by the total amount of time MMS spent in the plasma sheet in that same MLT × R sector. *e)* Is the approximate region which has been studied by the Cluster mission [Rong et al., 2011].

TCS is an insufficient condition for reconnection.

4.4 Discussion

A feature of reconnection which stands out in observations is that IDRs and related phenomena occur preferentially in the pre-midnight sector [Eastwood et al., 2010, Nagai et al., 2013, Genestreti et al., 2014]. The explanation for this has been glossed over somewhat since the question of observational bias due to orbital variations was not often addressed (see discussion in Imber et al. 2013). If an observatory spends more time near dusk then one supposes its chances of seeing IDRs or other phenomena is increased relative to other regions, all other things being equal. Thus while studies based on previous missions showed a dawn-dusk asymmetry in observed reconnection-related features, we as a field could not be sure it was not due to an observational bias without rigorously including orbital statistics, something not often done in the literature. This question was addressed in Chapter 2 which confirmed that the asymmetric distribution of IDRs by MMS was not a function of observational bias, but is a result of magnetotail physics.

The strong asymmetry in typical current sheet thickness is not entirely surprising. In addition to previous studies which observed a similar asymmetry but were more limited in extent [Rong et al., 2011] or utilized more indirect methods for calculating current sheet thickness [Lu et al., 2019], mechanisms for the source of this asymmetry have also been mooted. Lu et al. (2018) and Pritchett and Lu (2018) have hypothesized that the cause of this dusk-side preference was preferential thinning on the pre-midnight region of the tail due to an externally-driven convective electric field and enhanced by Hall electric fields (normal to the central current sheet) which formed as the current sheet approached ion scales. Comparing our observations to this model we find the ratio of dwell time in an ion-scale TCS (70.7% pre-midnight to 29.3% post-midnight $\approx 2:1$) qualitatively supports the model of Lu et al. A comparison of Figure 4.3 and Figure 2 in Lu et al. (2018) is even more

encouraging as the radial variations in our observations are qualitatively similar to those shown in the PIC simulations.

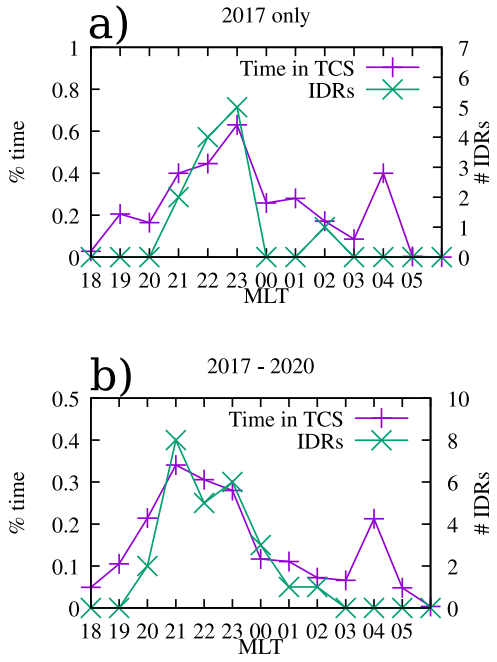

Figure 4.6: Plots of the proportion of the time MMS spent in a TCS relative to total time spent in the plasma sheet as well as the location of identified IDRs, both as a function of MLT, for the 2017 tail season (a) and the combined 2017–2020 tail seasons (b).

We can also see the pre-/post-midnight TCS asymmetry clearly in Figure 4.6 which plots the time MMS spent in a TCS as a percentage of the total time spent in the plasma sheet, along with the number of IDRs identified in each MLT division. Simulations [Lu et al., 2016, 2018, Pritchett and Lu, 2018, Liu et al., 2019] show that current sheet thinning precedes reconnection onset, generally followed by a rapid thickening. No effort has been made here to directly correlate any particular TCS encounter with a specific IDR encounter, or to determine conclusively that any or all TCSs encountered lead to reconnection. It is, however, unsurprising that the number of IDRs identified in a region of the magnetotail increases with the greater proportional time spent in a TCS. Less expected is the greater duskward extent of the TCS than observed IDRs.

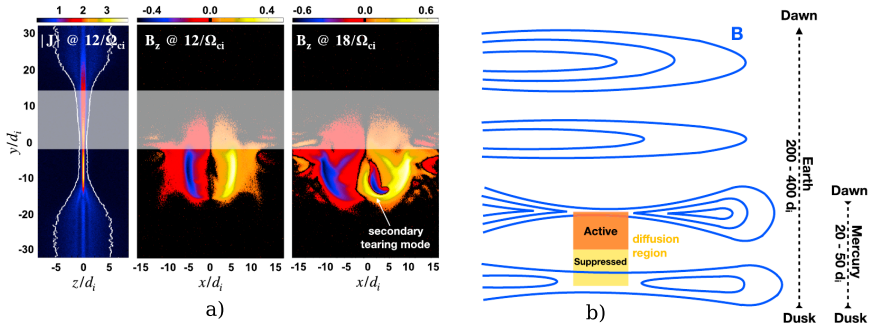

Figure 4.7: Key results from 3D PIC simulations published by Liu et al. (2019). *a)* (Liu et al. (2019) Figure 7) A slice through an ion-scale thin current sheet showing the competing influences of the Hall-driven dawnward drift creating the TCS and the global duskward cross-tail current. *b)* (Liu et al. (2019) Figure 9) This leads to the tail central current sheet being typically thinner on the duskside of midnight than the dawnside due to $\vec{E}_{Hall} \times \vec{B}$ drift, but with the constant cross-tail current suppressing reconnection onset on the duskside of those TCSs. Liu et al. [2019]

Recent 3D PIC simulations [Liu et al., 2019] suggest that the near-midnight preference of observed reconnection may be due to the effects of Hall reconnection in three dimensions. Liu et al. show that reconnection on a given thin current sheet will be suppressed on the side of the current sheet opposite the direction of net current flow for a region on the scale of 10s of ion inertial lengths (see Figure 4.7*a*, adapted from Liu et al. 2019). In the geomagnetic tail, with a net dawnward current flow, this would lead to suppression of reconnection onset in the duskward side of an existing thin current sheet. As shown above, ion-scale TCSs capable of supporting possible reconnection are twice as likely to be found on dusk-side of midnight as on the dawn-side. Thus while reconnection is more likely to occur pre-midnight in the tail due to ion-scale TCSs occurring more frequently there, it is more likely to be suppressed as the TCS extends further duskward away from midnight (see Figure 4.7*b*, adapted from Liu et al. 2019). This would have the practical effect of concentrating reconnection onset in the region at and near midnight in the pre-midnight region. The location of nearly half of all identified IDRs is within the region of 22-24 MLT, supporting this hypothesis.

Also of note is the duskward expansion of both TCS and IDR locations over the four tail

seasons analyzed here. 2017–2019 were in the declining phase of solar cycle 24, while the 2020 tail season was in the minimum between cycles, or the beginning of cycle 25. Figure 4.6a shows the distribution of proportional time in a TCS as well as IDR distribution in MLT for the 2017 tail season with a 2017 annual average Dst of $-8.09nT$. Figure 4.6b shows the same distributions for the full four seasons studied here, during which time the Dst eased to an annual average of $-5.14nT$ in 2019 and averaged only $-5.54nT$ for the whole of 2018–2020 [Nose et al., 2015]. This implies not only that the process of plasma sheet compression is a global process dependant on solar activity, consistent with the Dungey cycle [Dungey, 1963], but that the mesoscale process of asymmetric TCS distribution is also a function of solar driving, as suggested by simulation [Liu et al., 2014, Pritchett and Lu, 2018].

4.5 Remarks

The work presented in this chapter was submitted for publication in the *Journal of Geophysical Research: Space Physics* and is under review at the time of this writing [Rogers et al., 2021].

CHAPTER 5

Conclusion

Utilizing a systematic approach with historical pedigree, I developed an automated algorithm for IDR detection and used it to identify more than two dozen reconnection regions in Chapter 2. As an alternative to this process, various scalar parameters were explored for use in the identification and analysis of IDRs in Chapter 3. One of these parameters, the Kappa parameter K, was then used to probe the structure of the magnetotail current sheet to an extent not previously accomplished. By doing so, recent theories regarding the evolution of tail current sheet thinning were tested and qualitatively confirmed, leading to an explanation for the asymmetric distribution of reconnecting current sheets in the geomagnetic tail in Chapter 4.

By doing so, reconnecting current sheets in the tail, and IDRs in particular, have been characterized using *in situ* data in a statistical fashion not previous found in literature. Just as important, the context for reconnection onset in terms of global magnetotail conditions has also been explored to a greater degree than has previously been attempted using *in situ* data. This work has been published in peer-reviewed journals Rogers et al. [2019a, 2021] and discussed at conference Rogers et al. [2019b] to enable future work to be built upon it, just as this work has been built upon the assembled knowledge and understanding of those who came before. A humble addition to an awe-inspiring field.

CHAPTER A

$\nabla\vec{B}$ From *in situ* Data

A.1 Introduction

Magnetic reconnection is, fundamentally, the process by which magnetic field topology changes causing a transfer of energy from the magnetic field into the surrounding plasma. This energy transfer is the initial link in a great many chains of interest to the space science and space weather communities. As such, understanding the geometry and topology of the magnetic field in and around regions of reconnection is an important topic of research

The gradient of the magnetic field is a key parameter for understanding this geometry. The flight formation of MMS allows for multipoint measurements of the magnetic field vector at the vertices of a roughly regular tetrahedron lattice. The following describes the mathematics and programming techniques used to calculate an estimate of the magnetic field gradient from these regular observations.

The magnetic field is ideally represented by a function $\vec{B}(\vec{r})$ which is continuously differentiable. As such the gradient of the magnetic field:

$$grad(\vec{B}) = \nabla\vec{B} = \partial_i B_j = \overline{\overline{G}}_{ij}$$

or

$$\vec{g}_{ij} = \partial_i b_j$$

where $b_j = \hat{b}$

using the Einstein summation convention for the index notation. All of which works very well on paper.

In our case, however, we do not know the full magnetic field function and instead only have four measurements of the value of the magnetic field at roughly equidistant points of a (usually, almost) ideal tetrahedron. This will require some extra hoops to jump through in order to interpolate the values of the magnetic field in the area of each observatory and then apply discrete estimation techniques to approximate the gradient of the interpolated field.

There are two methods for doing so that I will discuss here:

1. Calculating the spatial gradient operator using the Reciprocal Vector Lattice to the basis formed by the position vectors of the observatories

2. Solving for the gradient tensor using a Least-Squares Minimization of the gradient operator definition

These techniques were described in a collection of white papers on multi-spacecraft analysis edited by Paschmann in preparation of the Cluster mission [Paschmann and Daly, 1998]. While the derivations of each method are technically complete, they lack context and explanatory notes which make them unintelligible to the uninitiated. For that reason, each is fully re-derived here with additional steps, context, and explanations which I required for my own understanding of each. In both cases I will limit myself to linear interpolation and estimation of the magnetic field and gradient. Higher order interpolation schemes may be investigated at a later date.

A.2 The Reciprocal Vector Method

A.2.1 The Setup

The method of reciprocal vectors has its roots in the direct and reciprocal lattice bases from from crystallography and associated applied mathematics. In terms of geometrical objects,

which are typically defined by their edges and vertices in relation to external reference points, the reciprocal basis is instead determined by the faces of the object and is in relation to the object itself or internal reference points. Thus a change in the reciprocal basis will be the change relative to attributes of the object itself. When applied to the lattice of spatial locations of the vertices, the reciprocal will then give the change in positions from one point in the lattice to another.

This method is described in Chanteur (1998) and the derivation there, while mathematically complete, leaves a great deal to be desired in terms of explanation. In the following derivation I have endeavoured to utilize the mathematical derivation of the necessary terms to illuminate the physical interpretation which makes their application to this problem relevant. To begin, recall the definition of the magnetic field gradient:

$$\nabla \vec{B} = \overline{\overline{G}}_{ij} = \partial_i B_j$$

we can reframe this alternatively as:

$$dr_i \overline{\overline{G}}_{ij} = dB_j$$
$$\text{where } dr_i = d\vec{r} = \vec{r}_\alpha - \vec{r}_\beta$$
$$\Rightarrow \overline{\overline{G}}_{ij} = (dr)_i^{-1} dB_j$$

where Greek letters (excepting ∂) have been used to denote observatories of the MMS fleet and/or vertices of the tetrahedron formation where an observatory is located.

In this formulation, each unique permutation of $d\vec{r}_{\alpha\beta} = \vec{r}_\alpha - \vec{r}_\beta$ provides a set of three basis vectors with respect to an arbitrary vertex or observatory. (Note: for the remainder of our discussion of reciprocal vectors the terms 'observatory', 'spacecraft', and 'vertex' will be used interchangeably). A reciprocal basis can then be found, with each reciprocal basis vector normal to a face of the tetrahedron, through the volume, and passing through the

associated vertex opposite the originating face (see Figure A.1).

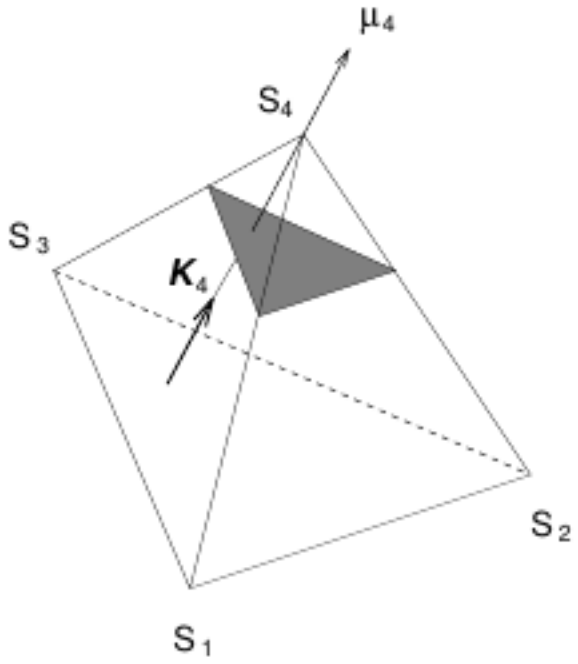

Figure A.1: An illustration of reciprocal vectors. The reciprocal vector $\vec{K}_4$ travels through and is perpendicular to the surface opposite the vertex S_4 formed by the vertices S_1, S_2, and S_3 [Chanteur and Harvey, 1998]

By taking some liberties with index notation, we can use $(dr)_i^{-1}$ to represent the reciprocal vector $\vec{K}$ associated with the vertex where B_j was measured. The reciprocal vector associated with the vertex β will be perpendicular to each basis vector which does not include β such that:

$$\vec{K}_\beta \cdot (\vec{r}_\alpha - \vec{r}_\gamma) = \delta_{\beta\alpha} - \delta_{\beta\gamma}$$

$$\Rightarrow \vec{K}_\beta \cdot \vec{r}_{\alpha\gamma} = \delta_{\beta\alpha} - \delta_{\beta\gamma}$$

$$\text{and } \vec{K}_\beta \cdot \vec{r}_{\alpha\epsilon} = \delta_{\beta\alpha} - \delta_{\beta\epsilon}$$

where δ is used here to represent the Kronecker delta function and I introduce the convention of $\vec{r}_{\alpha\gamma} = (\vec{r}_\alpha - \vec{r}_\gamma)$ and so on for all permutations of the vertices $\alpha, \beta, \gamma, \epsilon$.

This further implies a few more relations:

$$\begin{aligned} \vec{K}_\beta &= a(\vec{r}_{\alpha\gamma} \times \vec{r}_{\alpha\epsilon}) \text{ where } a \text{ is a scalar} \\ \text{and } \vec{K}_\beta \cdot \vec{r}_{\alpha\beta} &= 1 \\ \Rightarrow a(\vec{r}_{\alpha\gamma} \times \vec{r}_{\alpha\epsilon}) \cdot \vec{r}_{\alpha\beta} &= 1 \\ \Rightarrow a &= \frac{1}{(\vec{r}_{\alpha\gamma} \times \vec{r}_{\alpha\epsilon}) \cdot \vec{r}_{\alpha\beta}} \\ \therefore \vec{K}_\beta &= \frac{(\vec{r}_{\alpha\gamma} \times \vec{r}_{\alpha\epsilon})}{(\vec{r}_{\alpha\gamma} \times \vec{r}_{\alpha\epsilon}) \cdot \vec{r}_{\alpha\beta}} \end{aligned} \tag{A.1}$$

This expression can be used to find the reciprocal vector associated with each vertex by permutation through each index.

A.2.2 The Gradient

$$\vec{K}_\beta = \frac{(\vec{r}_{\alpha\gamma} \times \vec{r}_{\alpha\epsilon})}{(\vec{r}_{\alpha\gamma} \times \vec{r}_{\alpha\epsilon}) \cdot \vec{r}_{\alpha\beta}}$$

The reciprocal vector represents the inverse of the change with respect to position internally perpendicular to one face of the tetrahedron, through the volume of the lattice, and then through the vertex opposite the originating face. It is, essentially, the operator $\frac{\partial}{\partial r}$ along that reciprocal basis associated with the vertex it passes through. It has the (perhaps intuitive) property that $\sum_{\alpha=1}^{N=4} \vec{K}_\alpha = 0$. This is critical to its utility as the spatial differentiation operator.

A single reciprocal vector applied to a function (be it scalar or vector) would only include a contribution from that single vertex. The function or measurement at each vertex must be operated on by its associated reciprocal vector operator and then the resultant contributions from each reciprocal basis summed in order to not only include information from all the basis vectors, but also to cancel-out those components which are identical at multiple vertices.

Starting from our initial conjecture:

$$\begin{aligned} dr_i \overline{\overline{G}}_{ij} &= dB_j \\ \Rightarrow \overline{\overline{G}}_{ij} &= (dr)_i^{-1} dB_j \\ \text{recall } \vec{K}_\beta &\approx (d\vec{r})_\beta^{-1} \\ \Rightarrow (\overline{\overline{G}}_{ij})_\beta &= K_{\beta,i} B_{\beta,j} \\ \therefore \boxed{\overline{\overline{G}}_{ij} &= \sum_{\beta=1}^{4} K_{\beta,i} B_{\beta,j}} \end{aligned} \tag{A.2}$$

This is the gradient tensor estimated using reciprocal vectors in a linear approximation. The canonical 'Curlometer' technique is derived from this method of gradient estimation.

A.3 The Least-Squares Minimization Method

A.3.1 The Setup

An approach conceptually unique from the Reciprocal Vectors (RV) method is to minimize a cost function derived from the same initial conjecture. As stated in the introduction, the derivation of this technique as shown in Harvey (1998) is very efficient in its use of ink, but less useful or loquacious in terms of description either of motivation or meaning. I have included a greatly expanded discussion of both in my re-derivation here. We begin with the same initial conjecture as for the RV technique:

$$\begin{aligned} \overline{G}\, d\vec{r} &= d\vec{B} \\ \Rightarrow \overline{\overline{G}}\, d\vec{r} - d\vec{B} &= 0 \\ \text{where } d\vec{r} = (\vec{r}_\alpha - \vec{r}_\beta) &\text{ and } d\vec{B} = (\vec{B}_\alpha - \vec{B}_\beta) \\ \Rightarrow \sum_{\alpha=1}^{N} \sum_{\beta=1}^{N} \overline{G}(\vec{r}_\alpha - \vec{r}_\beta) - (\vec{B}_\alpha - \vec{B}_\beta) &= 0 \end{aligned}$$

where I again use the convention of Greek letter to represent vertices or observatories in the formation. Note that while a minimum of four vertices are required to satisfy this expression in three dimensions, it is inherently extensible to arbitrarily large fleets.

In order to solve the previous expression for $\overline{\overline{G}}$ we need to apply a constraint. By converting the expression into the kernel of a quadratic cost function S and solving for $\frac{\partial S}{\partial \overline{\overline{G}}} = 0$ we can retain the extensibility of the above formulation while determining the gradient tensor.

Convert to index notation

$$\sum_{\alpha=1}^{N}\sum_{\beta=1}^{N}\overline{\overline{G}}_{ij}(r_{\alpha,i} - r_{\beta}, i) - (B_{\alpha,j} - B_{\beta,j}) = 0$$

Create cost function

$$S = \sum_{\alpha=1}^{N}\sum_{\beta=1}^{N}\left[\overline{\overline{G}}_{ij}(r_{\alpha,i} - r_{\beta}, i) - (B_{\alpha,j} - B_{\beta,j})\right]^2$$

Solve for $\dfrac{\partial S}{\partial \overline{\overline{G}}_{ij}} = 0$

$$\Rightarrow \sum_{\alpha=1}^{N}\sum_{\beta=1}^{N}\left[\overline{\overline{G}}_{ij}(r_{\alpha,i} - r_{\beta}, i) - (B_{\alpha,j} - B_{\beta,j})\right](r_{\alpha,i} - r_{\beta,i}) = 0$$

$$\overline{\overline{G}}_{ij}\sum_{\alpha=1}^{N}\sum_{\beta=1}^{N}[(r_{\alpha,i} - r_{\beta}, i)(r_{\alpha,i} - r_{\beta,i})]$$

$$= \sum_{\alpha=1}^{N}\sum_{\beta=1}^{N}[(r_{\alpha,i} - r_{\beta}, i)(B_{\alpha,j} - B_{\beta,j})]$$

Reducing the left-hand side:

$$\overline{\overline{G}}_{ij}\sum_{\alpha=1}^{N}\sum_{\beta=1}^{N}[(r_{\alpha,i} - r_{\beta}, i)(r_{\alpha,i} - r_{\beta,i})] =$$

$$\overline{\overline{G}}_{ij}\sum_{\alpha=1}^{N}\sum_{\beta=1}^{N}[r_{\alpha,i}r_{\alpha,j} - (r_{\alpha,i}r_{\beta,j} + r_{\alpha,j}r_{\beta,i}) + r_{\beta,i}r_{\beta,j}]$$

This is already a bit of a mess, so I will introduce a lemma and a few definitions to simplify things. First, we need to address the cross-terms in the middle of the sum.

A.3.2 Lemma:

Assume all $\vec{r}_\alpha$ are in barycentric coordinates such that for $\vec{r}'_\alpha$ in arbitrary Cartesian coordinates (e.g. GSE, GSM, etc.):

$$\begin{aligned}\vec{r}_\alpha &= \vec{r}'_\alpha - \vec{r}_{bary} \\ &= \vec{r}_\alpha - \left(\sum_{\beta=1}^{N} \vec{r}'_\beta\right)\end{aligned}$$

This implies:

$$\sum_{\alpha=1}^{N} \vec{r}_\alpha = \sum_{\alpha}^{N} r_{\alpha,i} = 0$$

Returning to the left hand side of our minimization and applying the lemma shown, middle cross-terms are:

$$\begin{aligned}&\sum_{\alpha=1}^{N}\sum_{\beta=1}^{N}\left(r_{\alpha,i}r_{\beta,j} + r_{\alpha,j}r_{\beta,i}\right) \\ &\qquad = \left[\sum_{\alpha=1}^{N} r_{\alpha,i}\left(\sum_{\beta=1}^{N} r_{\beta,j}\right)\right] + \left[\sum_{\alpha=1}^{N} r_{\alpha,j}\left(\sum_{\beta=1}^{N} r_{\beta,i}\right)\right] \\ &\qquad = \sum_{\alpha=1}^{N} r_{\alpha,i}(0) + \sum_{\alpha=1}^{N} r_{\alpha,j}(0) \\ &\qquad = 0\end{aligned}$$

This removes the middle cross-terms from the left hand side.

Now the left hand side of the minimised function is:

$$\begin{aligned} L.H.S. &= \overline{\overline{G}}_{ij} \sum_{\alpha=1}^{N} \sum_{\beta=1}^{N} r_{\alpha,i} r_{\alpha,j} + r_{\beta,i} r_{\beta,j} \\ \text{Let } \sum_{\alpha=1}^{N} r_{\alpha,i} r_{\alpha,j} &\equiv N \overline{\overline{R}}_{ij} \\ \Rightarrow L.H.S. &= \overline{\overline{G}}_{ij} \sum_{\alpha=1}^{N} r_{\alpha,i} r_{\alpha,j} + \left(N \overline{\overline{R}}_{ij} \right) \\ &= 2N^2 \overline{\overline{G}}_{ij} \overline{\overline{R}}_{ij} \end{aligned}$$

where we have introduced $\overline{\overline{R}}_{ij}$ which Harvey calls the 'Volumetric Tensor.' For the purposes of this discussion, it is simply shorthand for the sum of the self-outer-products of the position vectors of each observatory.

Now we combine the 'simplified' left hand side of the minimization equation with the thus-far ignored right hand side:

$$\begin{aligned} 2N^2 \overline{\overline{G}}_{ij} \bar{R}_{ij} &= \sum_{\alpha=1}^{N} \sum_{\beta=1}^{N} [(r_{\alpha,i} - r_{\beta}, i)(B_{\alpha,j} - B_{\beta,j})] \\ \Rightarrow \boxed{\overline{\overline{G}}_{ij} = \frac{1}{2N^2} \sum_{\alpha=1}^{N} \sum_{\beta=1}^{N} [(r_{\alpha,i} - r_{\beta}, i)(B_{\alpha,j} - B_{\beta,j})] \, \overline{\overline{R}}_{ij}^{-1}} \end{aligned} \tag{A.3}$$

This is the gradient tensor estimated using least-squares minimization in a linear approximation.

A.3.3 Discussion of Least-Squares

The least-squares minimization (LSM) gradient definition has some notably different properties than the RV formulation. First, the $\partial \vec{B}$ aspect is more explicit in the $B_\alpha - B_\beta$ terms than in the RV formulation which buries it in the summation over all vertices. Second is the volumetric tensor ($\overline{\overline{R}}_{ij}$) which is, at first glance, an even harder conceptual nut to crack

than 'where is the $\partial\vec{B}$?' from RV. By recognizing it as shorthand for terms which fall out of the expansion of the minimized cost function I have found that the volumetric tensor loses much of its mystery.

That does bring up an additional hurdle, however. Least-squares minimization is familiar to any undergraduate physics major who has passed their senior lab course, but its application here is a leap I haven't been able to follow yet. Certainly, as a mathematical device, it functions well in providing a necessary constraint, but the conceptual implication of its application raises concerns. Specifically, the canonical usage for LSM is to 'fit' a function through scattered points, 'smoothing-out' extreme contributions from outliers to give a robust estimation for the overall behavior of the function with respect to the data fitted.

While that has not been observed in comparisons between RV and LSM calculations of the gradient in these implementations, it is a possibility to consider if the number of observatories/vertices is expanded beyond the four in the MMS mission. It may be that the RV method is the more robust for being the most straightforward.

A.4 Validation of Techniques and Implementations

A.4.1 Validation: Theoretical

One way to check that the calculated gradient tensors we've generated using either technique is to use the properties of the Levi-Civita rotation tensor combined with the commutativity of the partial differentiation operator. These properties are commonly seen in the well-known identity:

$$\nabla \times \nabla(A) = \epsilon_{ijk}\partial_j\partial_k A = \vec{0}$$

where A is a scalar. The rotation tensor causes reversed terms of the combined partial differentiation operators to cancel. We can apply the same properties to higher order variables:

$$\nabla \times (\nabla \vec{B}) = \epsilon_{ijk} \partial_i \bar{G}_{jk} = \epsilon_{ijk} \partial_i \partial_j \vec{B}_k = 0$$

This can be implemented in a straight-forward manner using the Reciprocal vectors technique, where each reciprocal vector $\vec{k}_\alpha$ represents the ∂_i operator for each vertex α. Using this definition, the operational form of our check will be:

$$\sum_{\alpha=1}^{4} \epsilon_{ijk} k_{\alpha i} k_{\alpha j} B_{\alpha k} = 0$$

In actual application with real data in numerical calculation we would expect to be very close to zero (near the floating-point uncertainty of the calculation engine used), or at least several orders of magnitude smaller than the magnitude of the gradient tensor $\overline{\overline{G}}_{ij}$.

A.4.2 Validation: Applying Data

For the test data we compare to a MMS event on 16 October 2015 first reported on by Burch et al. 2015 and further analyzed by Torbert et al. 2016. The period in question was 2015-10-16/13:05:35 to 2017-10-16/13:07:25 UTC, shown in Figure A.2.

During this time period, some statistics of the calculated values of $\epsilon_{ijk} \partial_i \partial_j \vec{B}_k$ were:

- Maximum: $3.12e-17$ $\frac{nT}{m^2}$
- Mean: $2.56e-18$ $\frac{nT}{m^2}$

These extremely small values, especially when compared to the mean value of $|\nabla \vec{B}|$ of $0.155 \frac{nT}{m^2}$, indicate a strong confidence in the calculation. Most, in fact, can be considered within the floating point calculation error of the computing engine.

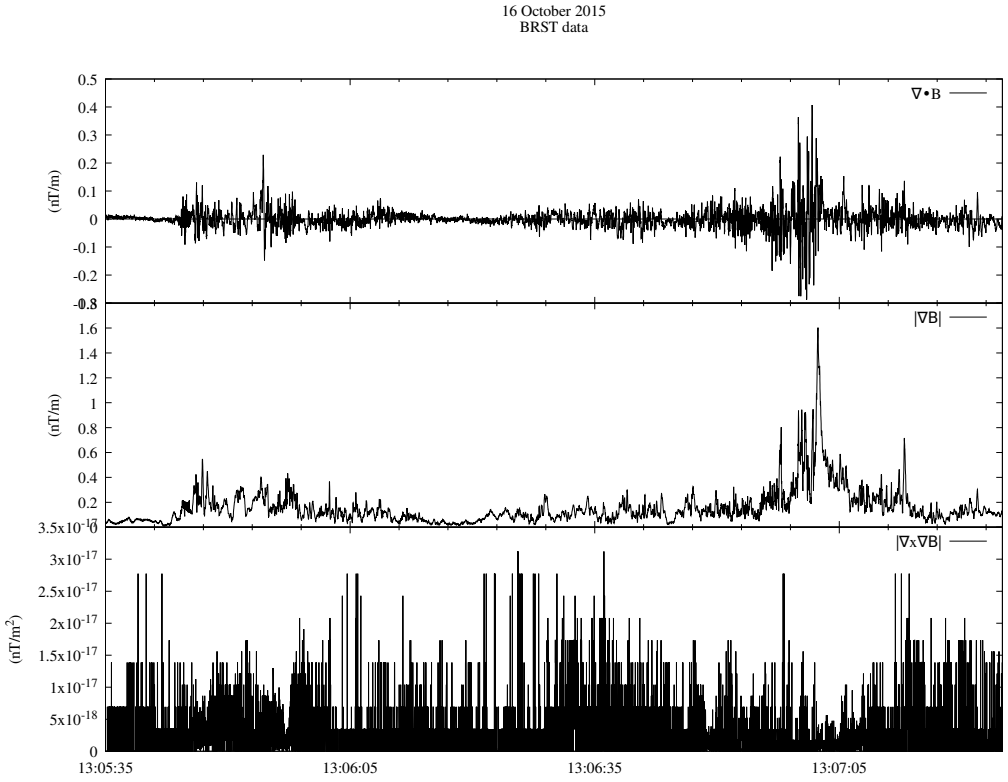

Figure A.2: The divergence (top panel) and gradient magnitude (middle panel) of the magnetic field for an example period of MMS data `2015-10-16/13:05:35 -- 2017-10-16/13:07:25 UTC`. The calculated values of $\epsilon_{ijk}\partial_i\partial_j\vec{B}_k$ are in the bottom panel.

A.5 Comparisons of Calculations

A.5.1 Current Density: LSM vs FPI

The following figures compare the current density calculated using the Least-Squares Minimization (LSM) gradient with that derived from the combined ion and electron moments from the FPI instrument. The LSM current density is calculated:

$$\vec{J}_{LSM} = J_i = \epsilon_{ijk}(\nabla B)_{jk}\mu_0^{-1}$$

while the FPI current density is defined as:

$$\vec{J}_{FPI} = q(n_{ion}\vec{v}_{ion} - n_{electron}\vec{v}_{electron})$$

The agreement is generally monotonic and appears to follow a smoothed verion of the values calculated using FPI moments, with significant deviations occuring primarily at local extrema values.

A.5.2 Current Density: Torbert vs RV

Figure A.4 shows Figure 3 from Torbert et al. [2016], showing the current densities provided by FPI at each individual observatory as well as the current density calculated by the RV curlometer method as coded and implemented by Roy Torbert. The agreement between the curlometer and individual FPI current densities qualitatively appears similar to those shown in Figure A.3. The current density for this same event as calculated by applying $\mu_0^{-1}\epsilon_{ijk}$ to the $\overline{\overline{G}}_{jk}$ calculated using the RV code I developed as part of Rogers and Rogers [2022] is shown in Figure A.5. The agreement between the RV-based curlometer as implemented in Torbert et al. [2016] and that using my own code is excellent.

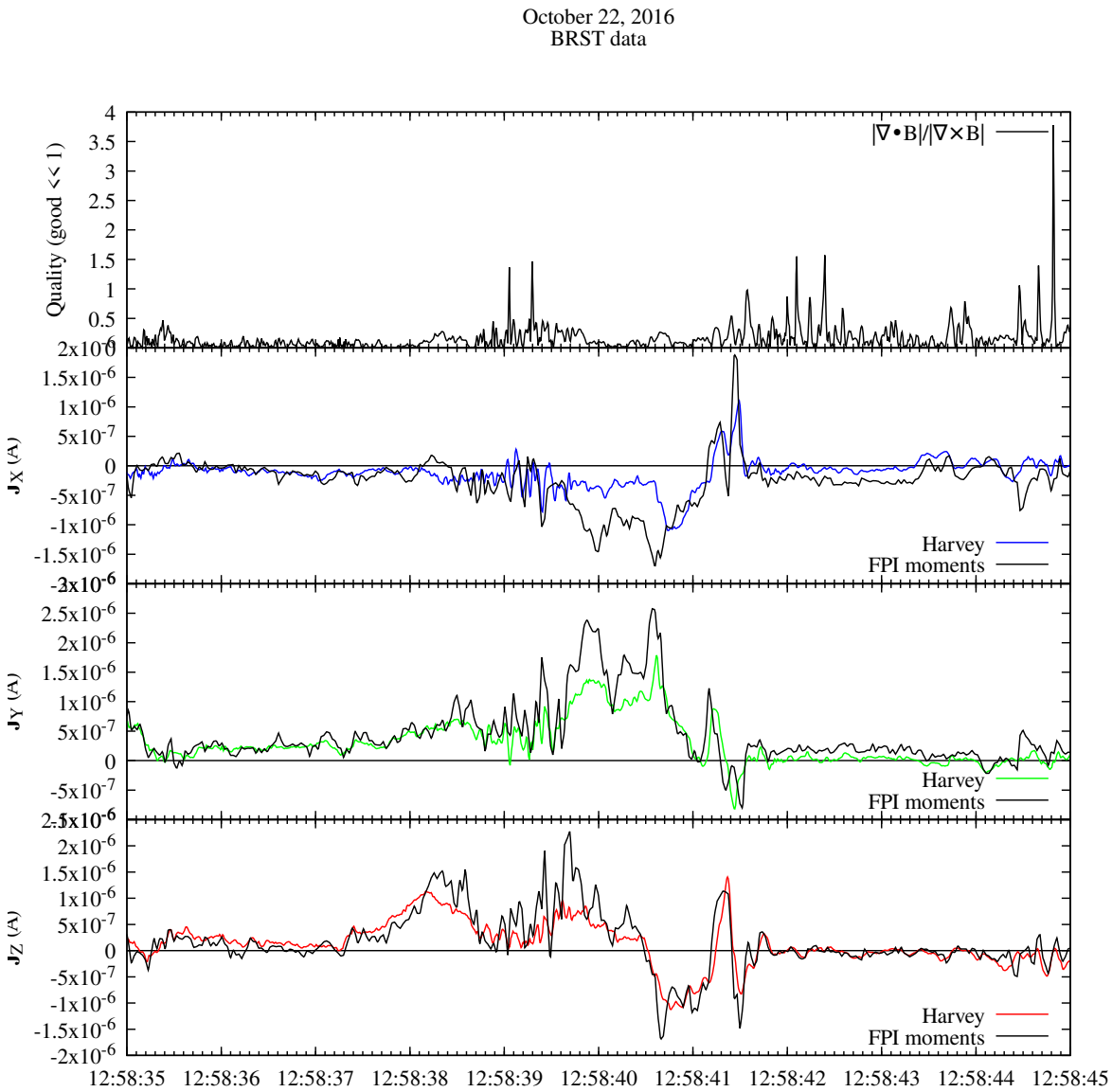

Figure A.3: The overall shape and behavior is in good agreement between both $\epsilon_{ijk}\overline{\overline{G}}_{ij}$ and $(n_i\vec{v}_i - n_e\vec{v}_e)$ from FPI. The primary differences come in the magnitude of each component at extrema in the FPI values.

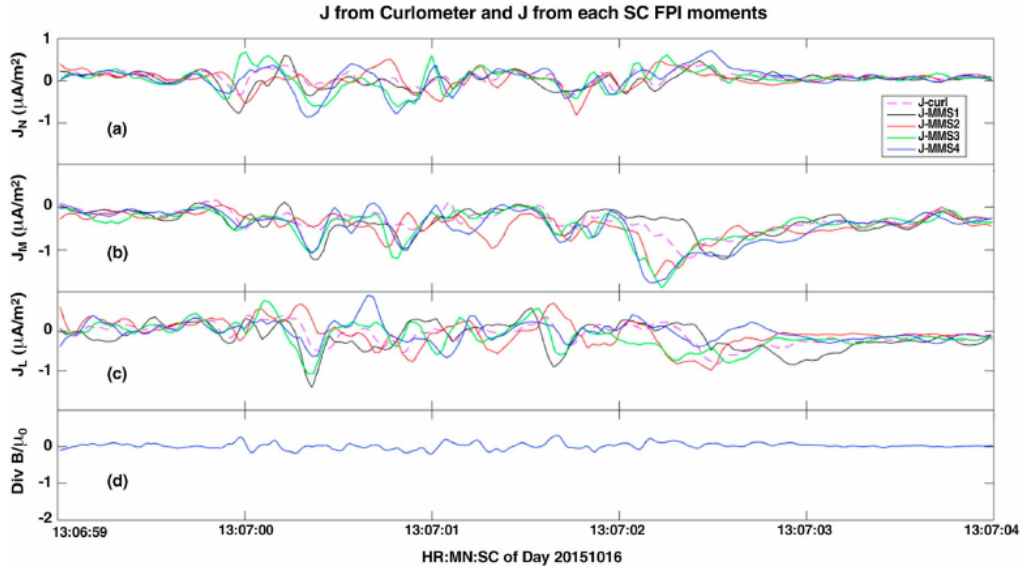

Figure A.4: This is Figure 3 from Torbert et al. 2016 showing the current density calculated by his own implementation of the curlometer technique (dashed lines)

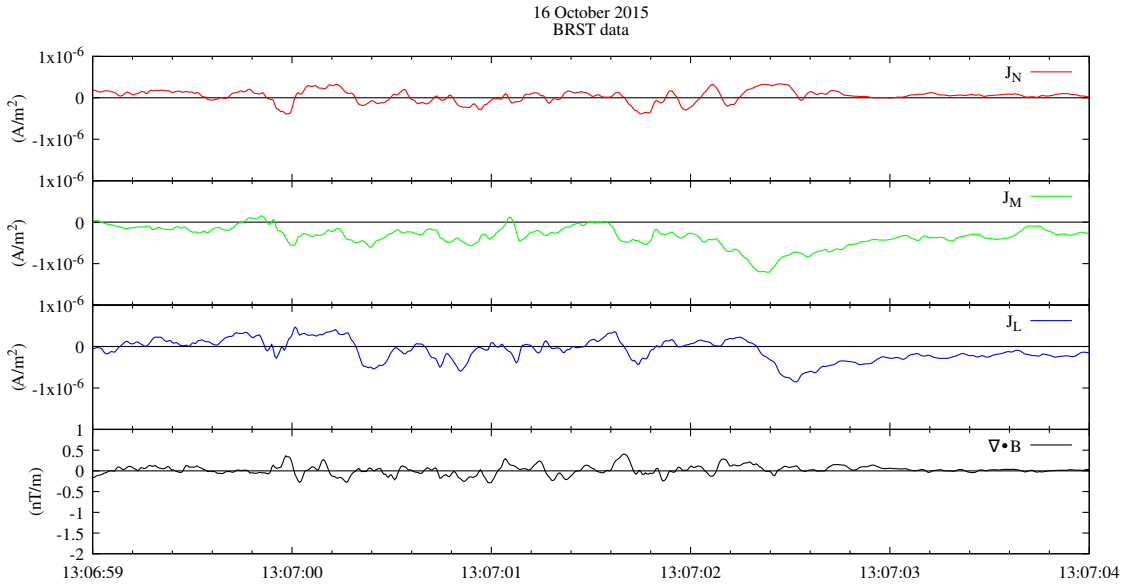

Figure A.5: Here are the same quantities as shown in Figure A.4, calculated with the RV implementation described previously. The agreement is excellent.

A.5.3 LSM Implementation Comparison

Another group at UCLA has also developed an implementation of the LSM gradient estimator. At my request, Yi Qi, a member of that group, was kind enough to calculate the curvature vectors of three comparison events for comparison with those calculated by my own implementation. I should emphasize that our codes were developed entirely independent of one another; neither of us realized the other was working on this approach until we met at a conference. Since then we have been scrupulous to avoid sharing actual code to preserve means of independent comparison.

Again, excellent agreement is visible in Figure A.6, with only small variations at isolated locations.

A.5.4 LSM vs Cluster (RV) Comparison

Runov et alia (2005) calculated an estimate of the magnetic field gradient using the Reciprocal Vectors method described above, as well as the field line curvature and current density based on that gradient for an event in 2001 using data from early in the Cluster mission. When I reached out to him, Runov was kind enough to provide the version of the data he used to calculate this gradient so that I might calculate it independently for comparison of our techniques.

As with comparisons with the FPI current density, Figure A.7 shows the LSM-derived curvature follows the behavior of the Runov RV-derived curvature monotonically in $\hat{x}$ and $\hat{y}$, and is recognizably similar in $\hat{z}$ across the bulk of the event. As before, the greatest differences lie in the magnitude of extrema which can be as much as a factor of two here. The differences in $\hat{z}$ are more puzzling and require investigation into the implementation by each party.

Investigation of the IDL code used by Runov et al. to calculate the curvature showed

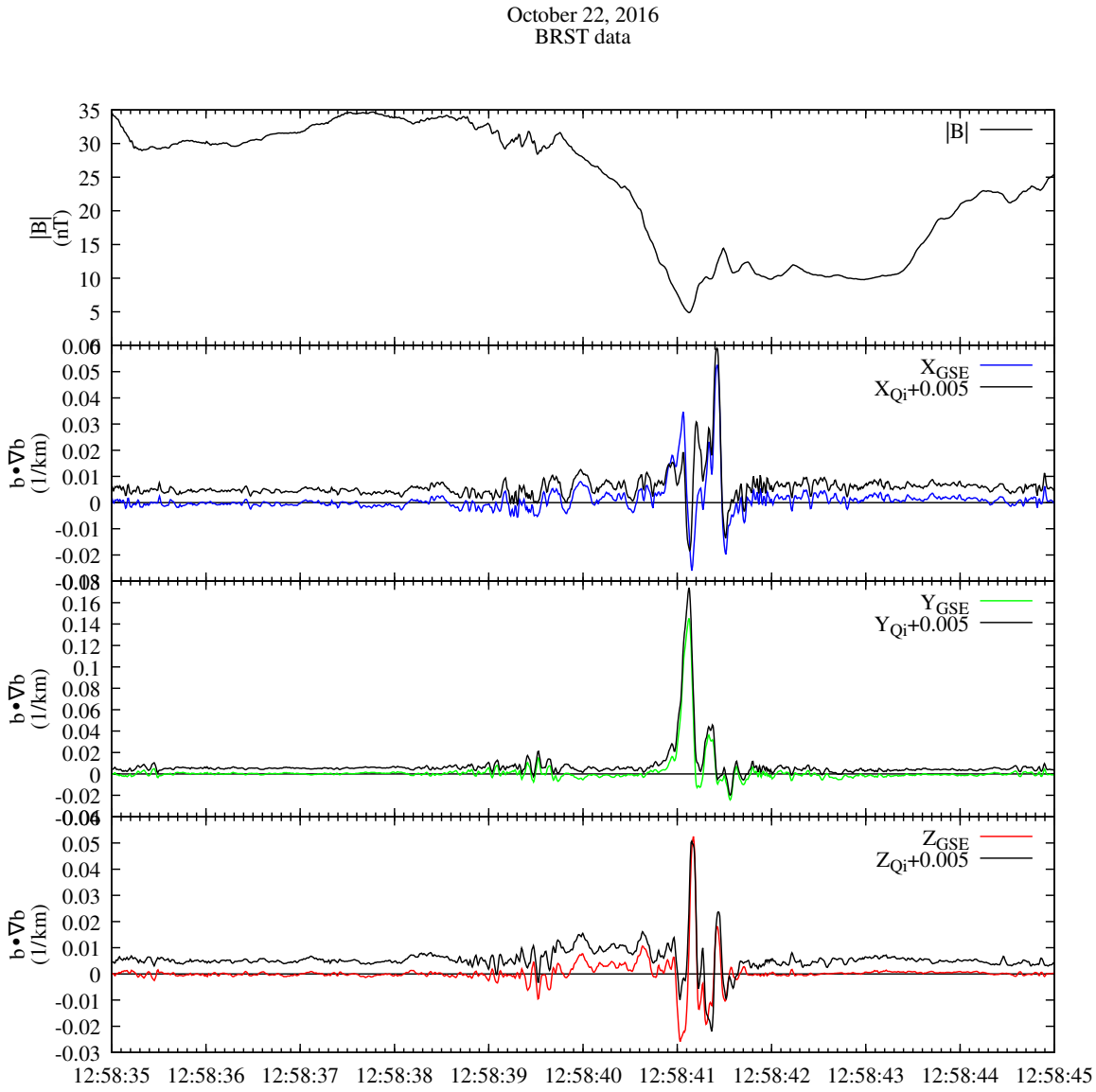

Figure A.6: Curvature vector comparison of the 2016-10-22 event with the same quantity calculated by Yi Qi. Excellent agreement with only small variations at isolated locations. Note that a DC offset has been included to the data from Yi Qi.

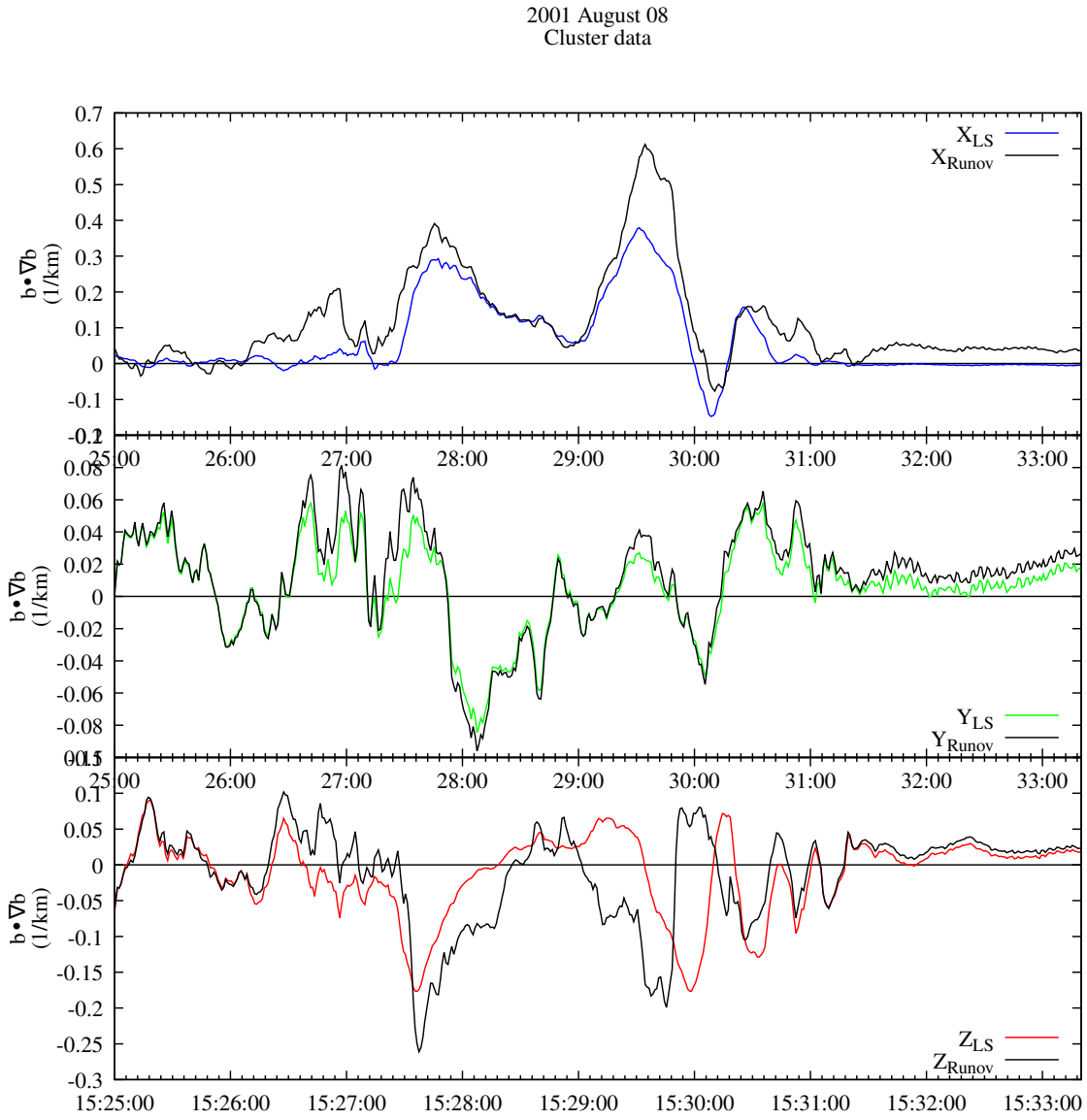

Figure A.7: A comparison of the curvature vector calculated by Runov et al. with that calculated using the LSM method. See text for details

their implementation did not normalize $\vec{B}$ before calculating the gradient for the purposes of curvature, instead scaling the entire $\vec{B} \cdot \nabla \vec{B}$ by B^{-2}. As $\frac{\nabla \vec{B}}{B} \neq \nabla \hat{b}$ where $\hat{b} = \vec{B}/B$ this introduces errors into the final calculation. It is of note that this formulation error is still present in the reference implementation of the magnetic field curvature IDL procedure included in the SPEDAS package. I have recreated that calculation error in Figure A.8. Agreement is now uniformly monotonic between the RV implementaion of Runov and my implementation of LSM.

A.6 RV Implementation and Practical Considerations

The LSM code as developed is likely a faithful implementation of the LSM technique described by Harvey (1998), as implied by comparisons with Qi. Similarly, the errors in the Runov implementation of the RV technique and the partial success in reproducing those errors is a good indication that the RV code is a faithful implementation of that technique as well. The current density derived from both the LSM and RV implementations as developed match each other to within the floating point computation errors expected from electronic computation in all calculations made throughout this work. The disagreement in magnitude in some regions of the derived current density compared to those derived by FPI moments remains something of a puzzle requiring further investigation.

Computationally, the RV technique is by far the superior. With a great deal of work and consultation with a professional software developer regarding computational efficacy, as well as improved proficiency with the programming language and numerical packages used, the RV method can be made to scale favorably with the number of computation threads available. The LSM method, however, is strongly limited in its computational efficacy by the fundamental necessity of an matrix inversion operation ($\overline{\overline{R}}_{ij}^{-1}$, Eq. A.3) which has, thus far, a best-possible computational complexity of $O(n^{2.4})$ with $n = 3$ for all cases under consideration. The RV method, on the other had, depends on linear vector manipulation with

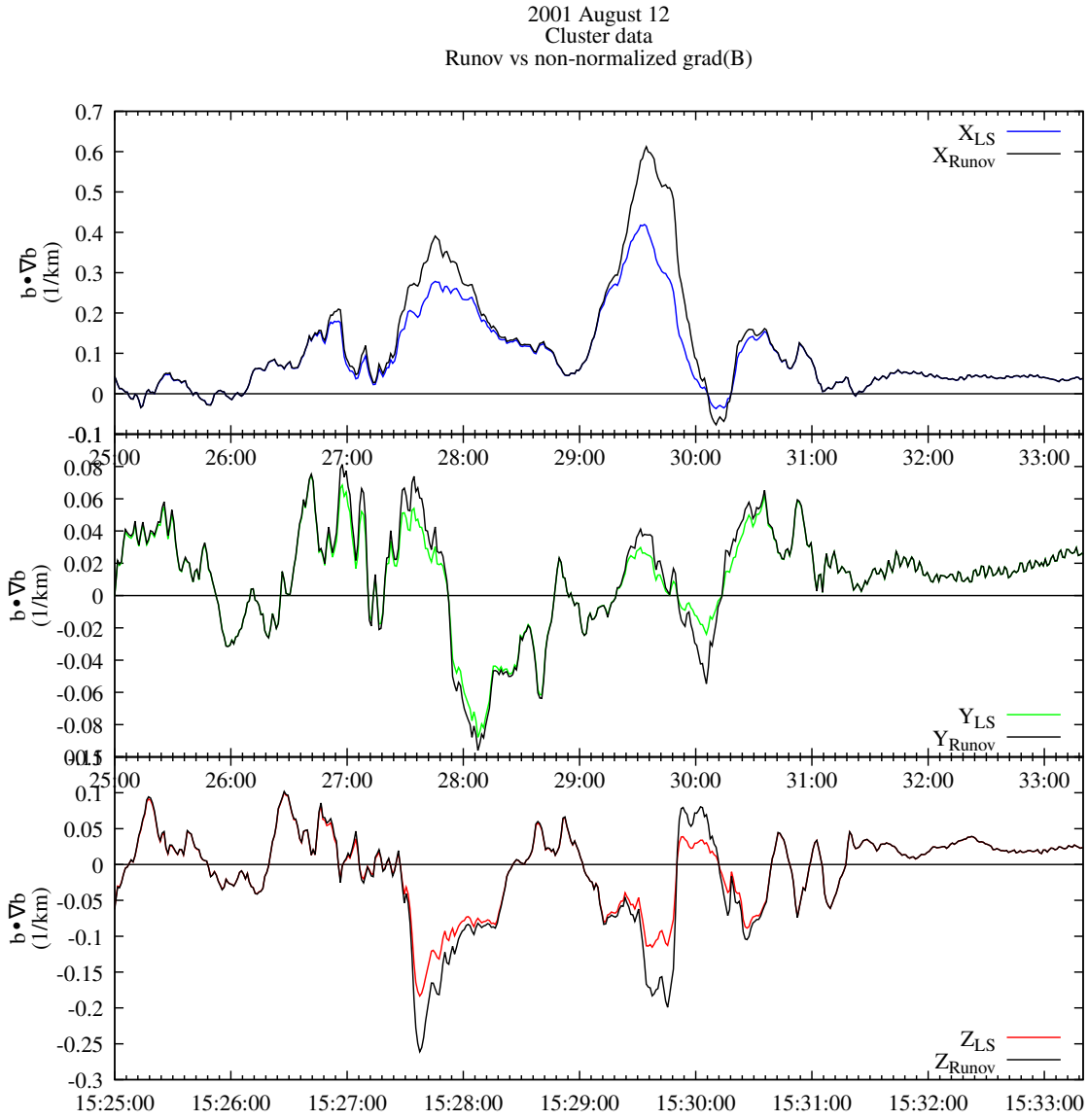

Figure A.8: Confirmation of the error in calculation of $\nabla \vec{B}$ by Runov et al. by recreation. LSM code was modified to duplicate the error.

$O(n \log n)$ complexity. Furthermore, the packages used, `python3.x` and `numpy`, use methods much closer to the ideal computational efficacy regarding linear array manipulation than they are regarding matrix inversion, further widening the practical difference in necessary computational time. The end result is an approximate factor of 3 difference in the computation time necessary for calculating $\nabla \vec{B}$ and related products using reciprocal vectors and least squares minimisation.

Looking to the future, the natural extensibility of the LSM method to larger formations with additional vertices such as HelioSwarm makes it very appealing on the surface. However, given the difference in computation time it will likely still be preferable to instead calculate several permutations of the RV method using different sets of vertices and find the statistical mean of them than use the LSM. This would also have the benefit of having already calculated the RVs of internal subdivisions of the total volume of the formation, meaning that the gradient could be calculated in several locations within the volume. This leads to more subtle topological analysis such as the gradient of the gradient of the magnetic fields and other quantities.

The code as utilized throughout this work is available from a publicly available repository [Rogers and Rogers, 2022]. While several of the functions provided in this package are constructed specifically for accessing and processing MMS data, the core functions which perform the mathematics described here are accessible independent of the data source and can be easily utilized with other data sets.

References

M. H. Acuna, K. W. Ogilvie, D. N. Baker, S. A. Curtis, D. H. Fairfield, and W. H. Mish. The Global Geospace Science Program and its investigations. *Space Science Reviews*, 71(1-4):5–21, Feb. 1995. ISSN 0038-6308, 1572-9672. doi: 10.1007/BF00751323.

S.-I. Akasofu. The development of the auroral substorm. *Planetary and Space Science*, 12 (4):273–282, Apr. 1964. ISSN 00320633. doi: 10.1016/0032-0633(64)90151-5.

H. Alfvén. On the Theory of Comet Tails. *Tellus*, 9(1):92–96, Feb. 1957. ISSN 00402826, 21533490. doi: 10.1111/j.2153-3490.1957.tb01855.x.

H. Alfven and B. Lindblad. Magneto-Hydrodynamic Waves and Sunspots. *Monthly Notices of the Royal Astronomical Society*, 105(1):3–16, Feb. 1945. ISSN 0035-8711, 1365-2966. doi: 10.1093/mnras/105.1.3.

V. Angelopoulos, P. Cruce, A. Drozdov, E. W. Grimes, N. Hatzigeorgiu, D. A. King, D. Larson, J. W. Lewis, J. M. McTiernan, D. A. Roberts, C. L. Russell, T. Hori, Y. Kasahara, A. Kumamoto, A. Matsuoka, Y. Miyashita, Y. Miyoshi, I. Shinohara, M. Teramoto, J. B. Faden, A. J. Halford, M. McCarthy, R. M. Millan, J. G. Sample, D. M. Smith, L. A. Woodger, A. Masson, A. A. Narock, K. Asamura, T. F. Chang, C.-Y. Chiang, Y. Kazama, K. Keika, S. Matsuda, T. Segawa, K. Seki, M. Shoji, S. W. Y. Tam, N. Umemura, B.-J. Wang, S.-Y. Wang, R. Redmon, J. V. Rodriguez, H. J. Singer, J. Vandegriff, S. Abe, M. Nose, A. Shinbori, Y.-M. Tanaka, S. UeNo, L. Andersson, P. Dunn, C. Fowler, J. S. Halekas, T. Hara, Y. Harada, C. O. Lee, R. Lillis, D. L. Mitchell, M. R. Argall, K. Bromund, J. L. Burch, I. J. Cohen, M. Galloy, B. Giles, A. N. Jaynes, O. Le Contel, M. Oka, T. D. Phan, B. M. Walsh, J. Westlake, F. D. Wilder, S. D. Bale, R. Livi, M. Pulupa, P. Whittlesey, A. DeWolfe, B. Harter, E. Lucas, U. Auster, J. W. Bonnell, C. M. Cully, E. Donovan, R. E. Ergun, H. U. Frey, B. Jackel, A. Keiling, H. Korth, J. P. McFadden, Y. Nishimura, F. Plaschke, P. Robert, D. L. Turner, J. M. Weygand, R. M. Candey, R. C. Johnson, T. Kovalick, M. H. Liu, R. E. McGuire, A. Breneman, K. Kersten, and P. Schroeder. The Space Physics Environment Data Analysis System (SPEDAS). *Space Science Reviews*, 215(1):9, Feb. 2019. ISSN 0038-6308, 1572-9672. doi: 10.1007/s11214-018-0576-4.

A. V. Artemyev, A. A. Petrukovich, R. Nakamura, and L. M. Zelenyi. Cluster statistics of thin current sheets in the Earth magnetotail: Specifics of the dawn flank, proton

temperature profiles and electrostatic effects. *J. Geophys. Res. Sp. Phys.*, 116(9):1–9, 2011. ISSN 21699402. doi: 10.1029/2011JA016801.

M. P. Aubry, C. T. Russell, and M. G. Kivelson. Inward motion of the magnetopause before a substorm. *Journal of Geophysical Research*, 75(34):7018–7031, Dec. 1970. ISSN 01480227. doi: 10.1029/JA075i034p07018.

W. Baumjohann. The near-Earth plasma sheet: An AMPTE/IRM perspective. *Space Science Reviews*, 64(1-2):141–163, 1993. ISSN 0038-6308, 1572-9672. doi: 10.1007/BF00819660.

W. Baumjohann, T. Nagai, A. Petrukovich, T. Mukai, T. Yamamoto, and S. Kokubun. Substorm signatures between 10 and 30 earth radii. *Advances in Space Research*, 25 (7-8):1663–1666, Jan. 2000. ISSN 02731177. doi: 10.1016/S0273-1177(99)00681-X.

J. Birn. Computer studies of the dynamic evolution of the geomagnetic tail. *Journal of Geophysical Research: Space Physics*, 85(A3):1214–1222, Mar. 1980. ISSN 01480227. doi: 10.1029/JA085iA03p01214.

J. Birn, M. Chandler, and R. Nakamura. Ion Beams in the Plasma Sheet Boundary Layer: MMS Observations and Test Particle Simulations. *J. Geophys. Res. Sp. Phys.*, 125(2): 1–14, 2020. ISSN 2169-9380. doi: 10.1029/2019ja027113.

A. L. Borg, M. Øieroset, T. D. Phan, F. S. Mozer, A. Pedersen, C. Mouikis, J. P. McFadden, C. Twitty, A. Balogh, and H. Rème. Cluster encounter of a magnetic reconnection diffusion region in the near-Earth magnetotail on September 19, 2003. *Geophys. Res. Lett.*, 32(L19105), 2005. ISSN 00948276. doi: 10.1029/2005GL023794.

J. BÜCHNER. On Spontaneous Reconnection in the Earth's Magnetotail. *J. Geomagn. Geoelectr.*, 43:223–231, 1991. ISSN 0022-1392. doi: 10.5636/jgg.43.supplement1_223.

J. Büchner and L. M. Zelenyi. Chaotization of the electron motion as the cause of an internal magnetotail instability and substorm onset. *J. Geophys. Res.*, 92(A12):13456–13466, 1987. ISSN 0148-0227. doi: 10.1029/ja092ia12p13456.

J. Büchner and L. M. Zelenyi. Regular and chaotic charged particle motion in magnetotaillike field reversals: 1. Basic theory of trapped motion. *J. Geophys. Res.*, 94(A9):11821–11842, 1989. ISSN 0148-0227. doi: 10.1029/ja094ia09p11821.

J. L. Burch, T. E. Moore, R. B. Torbert, and B. L. Giles. Magnetospheric Multiscale Overview and Science Objectives. *Space Science Reviews*, 199(1-4):5–21, Mar. 2016a. ISSN 0038-6308, 1572-9672. doi: 10.1007/s11214-015-0164-9.

J. L. Burch, R. B. Torbert, T. D. Phan, L. J. Chen, T. E. Moore, R. E. Ergun, J. P. Eastwood, D. J. Gershman, P. A. Cassak, M. R. Argall, S. Wang, M. Hesse, C. J. Pollock, B. L. Giles, R. Nakamura, B. H. Mauk, S. A. Fuselier, C. T. Russell, R. J. Strangeway, J. F.

Drake, M. A. Shay, Y. V. Khotyaintsev, P. A. Lindqvist, G. Marklund, F. D. Wilder, D. T. Young, K. Torkar, J. Goldstein, J. C. Dorelli, L. A. Avanov, M. Oka, D. N. Baker, A. N. Jaynes, K. A. Goodrich, I. J. Cohen, D. L. Turner, J. F. Fennell, J. B. Blake, J. Clemmons, M. Goldman, D. Newman, S. M. Petrinec, K. J. Trattner, B. Lavraud, P. H. Reiff, W. Baumjohann, W. Magnes, M. Steller, W. Lewis, Y. Saito, V. Coffey, and M. Chandler. Electron-scale measurements of magnetic reconnection in space. *Science (80-.).*, 352(6290), 2016b. ISSN 10959203. doi: 10.1126/science.aaf2939.

G. Chanteur and C. C. Harvey. Spatial Interpolation for Four Spacecraft: Application to Magnetic Gradients. *ISSI Scientific Reports Series*, 1:371–394, Jan. 1998.

S. Chapman and V. C. A. Ferraro. A new theory of magnetic storms. *Journal of Geophysical Research*, 36(2):77, 1931. ISSN 0148-0227. doi: 10.1029/TE036i002p00077.

H. Che, C. Schiff, G. Le, J. C. Dorelli, B. L. Giles, and T. E. Moore. Quantifying the effect of non-Larmor motion of electrons on the pressure tensor. *Physics of Plasmas*, 25(3): 032101, Mar. 2018. ISSN 1070-664X, 1089-7674. doi: 10.1063/1.5016853.

C. Cheng, S. Inoue, Y. Ono, and R. Horiuchi. Decoupling of Electron and Ion Dynamics in Driven Magnetic Reconnection in Collisionless Plasmas. *Plasma and Fusion Research*, 11(0):1401081–1401081, 2016. ISSN 1880-6821. doi: 10.1585/pfr.11.1401081.

F. V. Coroniti and C. F. Kennel. Changes in magnetospheric configuration during the substorm growth phase. *Journal of Geophysical Research*, 77(19):3361–3370, July 1972. ISSN 01480227. doi: 10.1029/JA077i019p03361.

S. Cowley. Magnetospheric asymmetries associated with the y-component of the IMF. *Planetary and Space Science*, 29(1):79–96, Jan. 1981. ISSN 00320633. doi: 10.1016/0032-0633(81)90141-0.

J. Dungey. *Cosmic Electrodynamics*. Cambridge Monographs on Mechanics and Applied Mathematics. Cambridge University Press, 1958. ISBN 978-1-316-60187-7.

J. Dungey. Interactions of solar plasma with the geomagnetic field. *Planetary and Space Science*, 10:233–237, Jan. 1963. ISSN 00320633. doi: 10.1016/0032-0633(63)90020-5.

J. W. Dungey. Interplanetary magnetic field and the auroral zones. *Phys. Rev. Lett.*, 6(2): 47–48, 1961. ISSN 00319007. doi: 10.1103/PhysRevLett.6.47.

J. W. Dungey. The length of the magnetospheric tail. *Journal of Geophysical Research*, 70 (7):1753–1753, Apr. 1965. ISSN 01480227. doi: 10.1029/JZ070i007p01753.

J. P. Eastwood, T. D. Phan, M. Øieroset, and M. A. Shay. Average properties of the magnetic reconnection ion diffusion region in the Earth's magnetotail: The 2001-2005 Cluster observations and comparison with simulations. *J. Geophys. Res. Sp. Phys.*, 115 (A08215), 2010. ISSN 21699402. doi: 10.1029/2009JA014962.

C. P. Escoubet, M. Fehringer, and M. Goldstein. The Cluster mission. *Annales Geophysicae*, 19(10/12):1197–1200, Sept. 2001. ISSN 1432-0576. doi: 10.5194/angeo-19-1197-2001.

D. H. Fairfield and L. J. Cahill. Transition region magnetic field and polar magnetic disturbances. *Journal of Geophysical Research*, 71(1):155–169, Jan. 1966. ISSN 01480227. doi: 10.1029/JZ071i001p00155.

C. J. Farrugia, D. J. Southwood, and S. W. Cowley. OBSERVATIONS OF FLUX TRANSFER EVENTS. *Adv. Sp. Res.*, 8(9):249–258, 1988. doi: 10.1016/0273-1177(88)90138-X.

C. J. Farrugia, A. J. Rogers, R. B. Torbert, K. J. Genestreti, T. K. M. Nakamura, B. Lavraud, P. Montag, J. Egedal, D. Payne, A. Keesee, N. Ahmadi, R. Ergun, P. Reiff, M. Argall, H. Matsui, L. B. Wilson, N. Lugaz, J. L. Burch, C. T. Russell, S. A. Fuselier, and I. Dors. An Encounter With the Ion and Electron Diffusion Regions at a Flapping and Twisted Tail Current Sheet. *Journal of Geophysical Research: Space Physics*, 126(3), Mar. 2021. ISSN 2169-9380, 2169-9402. doi: 10.1029/2020JA028903.

T. G. Forbes, E. W. Hones, S. J. Bame, J. R. Asbridge, G. Paschmann, N. Sckopke, and C. T. Russell. Evidence for the tailward retreat of a magnetic neutral line in the magnetotail during substorm recovery. *Geophysical Research Letters*, 8(3):261–264, 1981. doi: 10.1029/GL008i003p00261.

L. A. Frank. A survey of electrons $E > 40$ kev beyond 5 Earth radii with Explorer 14. *Journal of Geophysical Research*, 70(7):1593–1626, Apr. 1965. ISSN 01480227. doi: 10.1029/JZ070i007p01593.

L. A. Frank, K. L. Ackerson, and R. P. Lepping. On hot tenuous plasmas, fireballs, and boundary layers in the Earth's magnetotail. *J. Geophys. Res.*, 81(34):5859–5881, 1976. doi: 10.1029/ja081i034p05859.

H. Fu, E. E. Grigorenko, C. Gabrielse, C. Liu, S. Lu, K. J. Hwang, X. Zhou, Z. Wang, and F. Chen. Magnetotail dipolarization fronts and particle acceleration: A review. *Sci. China Earth Sci.*, 63(2):235–256, 2020. ISSN 18691897. doi: 10.1007/s11430-019-9551-y.

S. A. Fuselier, W. S. Lewis, C. Schiff, R. Ergun, J. L. Burch, S. M. Petrinec, and K. J. Trattner. Magnetospheric Multiscale Science Mission Profile and Operations. *Space Science Reviews*, 199(1-4):77–103, Mar. 2016. ISSN 0038-6308, 1572-9672. doi: 10.1007/s11214-014-0087-x.

K. J. Genestreti, S. A. Fuselier, J. Goldstein, T. Nagai, and J. P. Eastwood. The location and rate of occurrence of near-Earth magnetotail reconnection as observed by Cluster and Geotail. *J. Atmos. Solar-Terrestrial Phys.*, 121:98–109, 2014. ISSN 13646826. doi: 10.1016/j.jastp.2014.10.005.

K. J. Genestreti, T. K. M. Nakamura, R. Nakamura, R. E. Denton, R. B. Torbert, J. L. Burch, F. Plaschke, S. A. Fuselier, R. E. Ergun, B. L. Giles, and C. T. Russell. How Accurately

Can We Measure the Reconnection Rate EM for the MMS Diffusion Region Event of 11 July 2017? *Journal of Geophysical Research*, page 20, 2018. doi: 10.1029/2018JA025711.

T. I. Gombosi, D. L. DeZeeuw, C. P. T. Groth, K. G. Powell, and P. Song. The Length of the Magnetotail for Northward IMF: Results of Global 3D MHD Simulations. *PHYSICS OF SPACE PLASMAS*, (15):121–128, 1998.

E. G. Harris. On a plasma sheath separating regions of oppositely directed magnetic field. *Il Nuovo Cimento*, 23(1):115–121, Jan. 1962. ISSN 0029-6341, 1827-6121. doi: 10.1007/BF02733547.

C. C. Harvey. Spatial Gradients and the Volumetric Tensor. *ISSI Scientific Reports Series*, 1:307–322, Jan. 1998.

A. Hellemans. Cluster Mission to Rise From the Ashes. *Science*, 274(5291):1295–1295, Nov. 1996. ISSN 0036-8075, 1095-9203. doi: 10.1126/science.274.5291.1295.

E. Hones. Magnetic Reconnection in the Earth's Magnetotail. *Australian Journal of Physics*, 38(6):981, 1985. ISSN 0004-9506. doi: 10.1071/PH850981.

E. W. Hones. Transient phenomena in the magnetotail and their relation to substorms. *Space Science Reviews*, 23(3):393–410, May 1979. ISSN 0038-6308, 1572-9672. doi: 10.1007/BF00172247.

F. Hoyle. *Some Recent Researches in Solar Physics*. Cambridge University Press, Cambridge, 1949. ISBN 978-1-107-41892-9.

S. Y. Huang, K. Jiang, Z. G. Yuan, F. Sahraoui, L. H. He, M. Zhou, H. S. Fu, X. H. Deng, J. S. He, D. Cao, X. D. Yu, D. D. Wang, J. L. Burch, C. J. Pollock, and R. B. Torbert. Observations of the Electron Jet Generated by Secondary Reconnection in the Terrestrial Magnetotail. *Astrophys. J.*, 862:144, 2018. doi: 10.3847/1538-4357/aacd4c.

M. G. Kivelson and C. T. Russell, editors. *Introduction to Space Physics*. Cambridge University Press, Cambridge ; New York, 1995. ISBN 978-0-521-45104-8 978-0-521-45714-9.

D. Liu, S. Lu, Q. Lu, W. Ding, and S. Wang. Spontaneous Onset of Collisionless Magnetic Reconnection on an Electron Scale. *The Astrophysical Journal*, 890(2):L15, Feb. 2020. ISSN 2041-8213. doi: 10.3847/2041-8213/ab72fe.

Y.-h. Liu, J. Birn, W. Daughton, M. Hesse, and K. Schindler. Onset of reconnection in the near magnetotail: PIC simulations. *J. Geophys. Res. Sp. Phys.*, 119:9773–9789, 2014. doi: 10.1002/2014JA020492.

Y. H. Liu, T. C. Li, M. Hesse, W. J. Sun, J. Liu, J. Burch, J. A. Slavin, and K. Huang. Three-Dimensional Magnetic Reconnection With a Spatially Confined X-Line Extent: Implications for Dipolarizing Flux Bundles and the Dawn-Dusk Asymmetry. *J. Geophys. Res. Sp. Phys.*, 124(4):2819–2830, 2019. ISSN 21699402. doi: 10.1029/2019JA026539.

S. Lu, Y. Lin, V. Angelopoulos, A. V. Artemyev, P. L. Pritchett, Q. Lu, and X. Y. Wang. Hall effect control of magnetotail dawn-dusk asymmetry: A three-dimensional global hybrid simulation. *J. Geophys. Res. Sp. Phys.*, 121(12):11,882–11,895, 2016. ISSN 21699402. doi: 10.1002/2016JA023325.

S. Lu, P. L. Pritchett, V. Angelopoulos, and A. V. Artemyev. Formation of Dawn-Dusk Asymmetry in Earth's Magnetotail Thin Current Sheet: A Three-Dimensional Particle-In-Cell Simulation. *J. Geophys. Res. Sp. Phys.*, 123(4):2801–2814, Apr. 2018. ISSN 21699402. doi: 10.1002/2017JA025095.

S. Lu, A. V. Artemyev, V. Angelopoulos, Y. Lin, X. J. Zhang, J. Liu, L. A. Avanov, B. L. Giles, C. T. Russell, and R. J. Strangeway. The Hall Electric Field in Earth's Magnetotail Thin Current Sheet. *J. Geophys. Res. Sp. Phys.*, 124(2):1052–1062, 2019. ISSN 21699402. doi: 10.1029/2018JA026202.

M. E. Mandt, R. E. Denton, and J. F. Drake. Transition to whistler mediated magnetic reconnection. *Geophys. Res. Lett.*, 21(1):73–76, 1994. ISSN 19448007. doi: 10.1029/93GL03382.

B. H. Mauk, J. B. Blake, D. N. Baker, J. H. Clemmons, G. D. Reeves, H. E. Spence, S. E. Jaskulek, C. E. Schlemm, L. E. Brown, S. A. Cooper, J. V. Craft, J. F. Fennell, R. S. Gurnee, C. M. Hammock, J. R. Hayes, P. A. Hill, G. C. Ho, J. C. Hutcheson, A. D. Jacques, S. Kerem, D. G. Mitchell, K. S. Nelson, N. P. Paschalidis, E. Rossano, M. R. Stokes, and J. H. Westlake. The Energetic Particle Detector (EPD) Investigation and the Energetic Ion Spectrometer (EIS) for the Magnetospheric Multiscale (MMS) Mission. *Space Science Reviews*, 199(1-4):471–514, Mar. 2016. ISSN 0038-6308, 1572-9672. doi: 10.1007/s11214-014-0055-5.

I. B. McDiarmid and J. R. Burrows. Electron fluxes at 1000 kilometers associated with the tail of the magnetosphere. *Journal of Geophysical Research*, 70(13):3031–3044, July 1965. ISSN 01480227. doi: 10.1029/JZ070i013p03031.

F. S. Mozer, R. B. Torbert, U. V. Fahleson, C.-G. Fälthammar, A. Gonfalone, A. Pedersen, and C. T. Russell. Direct observation of a tangential electric field component at the magnetopause. *Geophysical Research Letters*, 6(4):305–308, Apr. 1979. ISSN 00948276. doi: 10.1029/GL006i004p00305.

T. Nagai, M. Fujimoto, Y. Saito, . S. Machida, T. Terasawa, R. Nakamura, •. T. Yamamoto, . T. Mukai, . A. Nishida, •', and S. Kokubun. Structure and dynamics of magnetic reconnection for substorm onsets with Geotail observations. Technical Report A3, 1998.

T. Nagai, I. Shinohara, M. Fujimoto, M. Hoshino, Y. Saito, S. Machida, and T. Mukai. Geotail observations of the Hall current system: Evidence of magnetic reconnection in the magnetotail. *Journal of Geophysical Research: Space Physics*, 106(A11):25929–25949, Nov. 2001. ISSN 01480227. doi: 10.1029/2001JA900038.

T. Nagai, M. Fujimoto, R. Nakamura, W. Baumjohann, A. Ieda, I. Shinohara, S. Machida, Y. Saito, and T. Mukai. Solar wind control of the radial distance of the magnetic reconnection site in the magnetotail. *J. Geophys. Res. Sp. Phys.*, 110(A9):1–11, 2005. ISSN 21699402. doi: 10.1029/2005JA011207.

T. Nagai, I. Shinohara, S. Zenitani, R. Nakamura, T. K. Nakamura, M. Fujimoto, Y. Saito, and T. Mukai. Three-dimensional structure of magnetic reconnection in the magnetotail from Geotail observations. *J. Geophys. Res. Sp. Phys.*, 118:1667–1678, 2013. ISSN 21699402. doi: 10.1002/jgra.50247.

N. F. Ness. The Earth's magnetic tail. *Journal of Geophysical Research*, 70(13):2989–3005, July 1965. ISSN 01480227. doi: 10.1029/JZ070i013p02989.

A. Nishida. The Geotail Mission. *Geophysical Research Letters*, 21(25):2871–2873, Dec. 1994. ISSN 00948276. doi: 10.1029/94GL01223.

M. Nose, M. Sugiura, T. Kamei, T. Iyemori, and Y. Koyama. Dst Index, 2015.

K. W. Ogilvie, T. von Rosenvinge, and A. C. Durney. International Sun-Earth Explorer: A Three-Spacecraft Program. *Science*, 198(4313):131–138, Oct. 1977. ISSN 0036-8075, 1095-9203. doi: 10.1126/science.198.4313.131.

M. Øieroset, T. D. Phan, R. P. Lin, and B. U. Ö. Sonnerup. Walén and variance analyses of high-speed flows observed by Wind in the midtail plasma sheet: Evidence for reconnection. *Journal of Geophysical Research: Space Physics*, 105(A11):25247–25263, Nov. 2000. ISSN 01480227. doi: 10.1029/2000JA900075.

M. Øieroset, T. D. Phan, M. Fujimoto, R. P. Lin, and R. P. Lepping. In situ detection of reconnection in the Earth's magnetotail. *Lett. to Nat.*, 412(July):414–416, 2001. doi: 10.1038/35086520.

E. N. Parker. Sweet's mechanism for merging magnetic fields in conducting fluids. *Journal of Geophysical Research*, 62(4):509–520, Dec. 1957. ISSN 01480227. doi: 10.1029/JZ062i004p00509.

E. N. Parker. Interaction of the Solar Wind with the Geomagnetic Field. *Physics of Fluids*, 1(3):171, 1958a. ISSN 00319171. doi: 10.1063/1.1724339.

E. N. Parker. Dynamics of the Interplanetary Gas and Magnetic Fields. *The Astrophysical Journal*, 128:664, Nov. 1958b. ISSN 0004-637X, 1538-4357. doi: 10.1086/146579.

G. Paschmann and P. W. Daly. *Analysis Methods for Multi-Spacecraft Data*. 1998.

D. S. Payne, C. J. Farrugia, R. B. Torbert, K. Germaschewski, A. R. Rogers, and M. R. Argall. Origin and structure of electromagnetic generator regions at the edge of the electron diffusion region. *Physics of Plasmas*, 28(11):112901, Nov. 2021. ISSN 1070-664X, 1089-7674. doi: 10.1063/5.0068317.

H. Petschek. Magnetic Field Annihilation. In *The Physics of Solar Flares*, Goddard Space Flight Center, Greenbelt, MD, 1964. National Aeronautics and Space Administration, Science and Technical Information Division.

W. G. Pilipp and G. Morfill. The formation of the plasma sheet resulting from plasma mantle dynamics. *Journal of Geophysical Research*, 83(A12):5670, 1978. ISSN 0148-0227. doi: 10.1029/JA083iA12p05670.

C. Pollock, T. Moore, A. Jacques, J. Burch, U. Gliese, Y. Saito, T. Omoto, L. Avanov, A. Barrie, V. Coffey, J. Dorelli, D. Gershman, B. Giles, T. Rosnack, C. Salo, S. Yokota, M. Adrian, C. Aoustin, C. Auletti, S. Aung, V. Bigio, N. Cao, M. Chandler, D. Chornay, K. Christian, G. Clark, G. Collinson, T. Corris, A. De Los Santos, R. Devlin, T. Diaz, T. Dickerson, C. Dickson, A. Diekmann, F. Diggs, C. Duncan, A. Figueroa-Vinas, C. Firman, M. Freeman, N. Galassi, K. Garcia, G. Goodhart, D. Guererro, J. Hageman, J. Hanley, E. Hemminger, M. Holland, M. Hutchins, T. James, W. Jones, S. Kreisler, J. Kujawski, V. Lavu, J. Lobell, E. LeCompte, A. Lukemire, E. MacDonald, A. Mariano, T. Mukai, K. Narayanan, Q. Nguyan, M. Onizuka, W. Paterson, S. Persyn, B. Piepgrass, F. Cheney, A. Rager, T. Raghuram, A. Ramil, L. Reichenthal, H. Rodriguez, J. Rouzaud, A. Rucker, Y. Saito, M. Samara, J. A. Sauvaud, D. Schuster, M. Shappirio, K. Shelton, D. Sher, D. Smith, K. Smith, S. Smith, D. Steinfeld, R. Szymkiewicz, K. Tanimoto, J. Taylor, C. Tucker, K. Tull, A. Uhl, J. Vloet, P. Walpole, S. Weidner, D. White, G. Winkert, P. S. Yeh, and M. Zeuch. Fast Plasma Investigation for Magnetospheric Multiscale. *Space Sci. Rev.*, 199, 2016. ISSN 15729672. doi: 10.1007/s11214-016-0245-4.

J. Posch, M. Engebretson, S. Mende, H. Frey, R. Arnoldy, M. Lessard, L. Lanzerotti, J. Watermann, M. Moldwin, and P. Ponomarenko. Statistical observations of spatial characteristics of Pi1B pulsations. *Journal of Atmospheric and Solar-Terrestrial Physics*, 69 (15):1775–1796, Nov. 2007. ISSN 13646826. doi: 10.1016/j.jastp.2007.07.015.

P. L. Pritchett and S. Lu. Externally Driven Onset of Localized Magnetic Reconnection and Disruption in a Magnetotail Configuration. *J. Geophys. Res. Sp. Phys.*, 123(4): 2787–2800, 2018. ISSN 21699402. doi: 10.1002/2017JA025094.

A. Raj, T. Phan, R. P. Lin, and V. Angeloppulos. Wind survey of high-speed bulk flows and field-aligned beams in the near-Earth plasma sheet. *J. Geophys. Res. Sp. Phys.*, 107(A12), 2002. ISSN 21699402. doi: 10.1029/2001JA007547.

A. Rogers and T. Rogers. Github.com/unh-mms-rogers/mms-curvature: MMS-Curvature Functioning Beta. doi: 10.5281/ZENODO.6456333, Apr. 2022.

A. J. Rogers, C. J. Farrugia, and R. B. Torbert. Numerical Algorithm for Detecting Ion Diffusion Regions in the Geomagnetic Tail With Applications to MMS Tail Season 1 May to 30 September 2017. *Journal of Geophysical Research: Space Physics*, 124(8): 6487–6503, Aug. 2019a. ISSN 2169-9380, 2169-9402. doi: 10.1029/2018JA026429.

A. J. Rogers, C. J. Farrugia, and R. B. Torbert. Testing the Efficacy of Selected Scalar Parameters for Identifying Ion Diffusion Regions in MMS Data. In *AGU Fall Meeting*, volume 2019, pages SM21B–3155, Dec. 2019b.

A. J. Rogers, C. J. Farrugia, R. B. Torbert, and T. J. Rogers. Applying Magnetic Curvature to to MMS data to identify thin current sheets relative to tail reconnection. *Journal of Geophysical Research: Space Physics*, 2021. doi: 10.48550/ARXIV.2112.04646.

Z. Rong, C. Shen, A. Petrukovich, W. Wan, and Z. Liu. The analytic properties of the flapping current sheets in the earth magnetotail. *Planetary and Space Science*, 58(10): 1215–1229, Aug. 2010. ISSN 00320633. doi: 10.1016/j.pss.2010.04.016.

Z. J. Rong, W. X. Wan, C. Shen, X. Li, M. W. Dunlop, A. A. Petrukovich, T. L. Zhang, and E. Lucek. Statistical survey on the magnetic structure in magnetotail current sheets. *J. Geophys. Res. Sp. Phys.*, 116(9):1–17, 2011. ISSN 21699402. doi: 10.1029/2011JA016489.

B. Rossi and S. Olbert. *Introduction to the Physics of Space*. Mcgraw-Hill, New York, 1970. ISBN 978-0-07-053892-4.

A. Runov, R. Nakamura, W. Baumjohann, R. A. Treumann, T. L. Zhang, M. Volwerk, Z. Vörös, A. Balogh, K. H. Glaßmeier, B. Klecker, H. Rème, and L. Kistler. Current sheet structure near magnetic X-line observed by Cluster. *Geophys. Res. Lett.*, 30(11), 2003. ISSN 00948276. doi: 10.1029/2002GL016730.

A. Runov, V. A. Sergeev, W. Baumjohann, R. Nakamura, S. Apatenkov, Y. Asano, M. Volwerk, Z. Vörös, T. L. Zhang, A. Petrukovich, A. Balogh, J. A. Sauvaud, B. Klecker, and H. Rème. Electric current and magnetic field geometry in flapping magnetotail current sheets. *Ann. Geophys.*, 23(4):1391–1403, 2005. ISSN 09927689. doi: 10.5194/angeo-23-1391-2005.

A. Runov, V. Angelopoulos, and X. Z. Zhou. Multipoint observations of dipolarization front formation by magnetotail reconnection. *J. Geophys. Res. Sp. Phys.*, 117(5):1–16, 2012. ISSN 21699402. doi: 10.1029/2011JA017361.

C. Russell and R. Elphic. Initial ISEE magnetometer results: Magnetopause observations. *Space Science Reviews*, 22(6), Dec. 1978. ISSN 0038-6308, 1572-9672. doi: 10.1007/BF00212619.

C. Russell and R. McPherron. The magnetotail and substorms. *Space Science Reviews*, 15 (2-3), 1973. ISSN 0038-6308, 1572-9672. doi: 10.1007/BF00169321.

C. T. Russell, B. J. Anderson, W. Baumjohann, K. R. Bromund, D. Dearborn, D. Fischer, G. Le, H. K. Leinweber, D. Leneman, W. Magnes, J. D. Means, M. B. Moldwin, R. Nakamura, D. Pierce, F. Plaschke, K. M. Rowe, J. A. Slavin, R. J. Strangeway,

R. Torbert, C. Hagen, I. Jernej, A. Valavanoglou, and I. Richter. The Magnetospheric Multiscale Magnetometers. *Space Sci. Rev.*, 199, 2016. ISSN 15729672. doi: 10.1007/s11214-014-0057-3.

J. Scudder and W. Daughton. Illuminating electron diffusion regions of collisionless magnetic reconnection using electron agyrotropy. *J. Geophys. Res. Sp. Phys.*, 113(6):1–16, 2008. ISSN 21699402. doi: 10.1029/2008JA013035.

J. D. Scudder and F. S. Mozer. Electron demagnetization and collisionless magnetic reconnection in Be1 plasmas. *Physics of Plasmas*, 12(9):092903, Sept. 2005. ISSN 1070-664X, 1089-7674. doi: 10.1063/1.2046887.

J. D. Scudder, F. S. Mozer, N. C. Maynard, and C. T. Russell. Fingerprints of collisionless reconnection at the separator, I, Ambipolar-Hall signatures. *J. Geophys. Res. Sp. Phys.*, 107(A10):1–38, 2002. ISSN 21699402. doi: 10.1029/2001JA000126.

J. D. Scudder, R. D. Holdaway, R. Glassberg, and S. L. Rodriguez. Electron diffusion region and thermal demagnetization. *J. Geophys. Res. Sp. Phys.*, 113(10):1–14, 2008. ISSN 21699402. doi: 10.1029/2008JA013361.

V. A. Sergeev, N. A. Tsyganenko, and V. Angelopoulos. Dynamical response of the magnetotail to changes of the solar wind direction: An MHD modeling perspective. *Annales Geophysicae*, 26(8):2395–2402, Aug. 2008. ISSN 1432-0576. doi: 10.5194/angeo-26-2395-2008.

C. Shen, Z. J. Rong, X. Li, M. Dunlop, Z. X. Liu, H. V. Malova, E. Lucek, and C. Carr. Magnetic configurations of the tilted current sheets in magnetotail. Technical report, 2008.

I. Shinohara, M. Fujimoto, T. Nagai, S. Zenitani, and H. Kojima. Low-Frequency Waves in the Tail Reconnection Region. In A. Keiling, D.-H. Lee, and V. Nakariakov, editors, *Geophysical Monograph Series*, pages 181–191. John Wiley & Sons, Inc, Hoboken, NJ, Feb. 2016. ISBN 978-1-119-05500-6 978-1-119-05495-5. doi: 10.1002/9781119055006.ch11.

D. G. Sibeck and V. Angelopoulos. THEMIS Science Objectives and Mission Phases. *Space Science Reviews*, 141(1-4):35–59, Dec. 2008. ISSN 0038-6308, 1572-9672. doi: 10.1007/s11214-008-9393-5.

H. Singer, E. Hones, and T. Rosenberg. Multipoint measurements from substorm onset to recovery: The relation between magnetic pulsations and plasma sheet thickening. *Advances in Space Research*, 8(9-10):443–446, Jan. 1988. ISSN 02731177. doi: 10.1016/0273-1177(88)90158-5.

B. U. Ö. Sonnerup. Magnetic Field Reconnection. In L. J. Lanzerotti, C. F. Kennel, and E. N. Parker, editors, *Sol. Syst. Plasma Phys.*, chapter III.1.2, pages 45–108. North-Holland Publishing Co., Amsterdam, 1979. ISBN 0-444-85267-0.

B. U. Ö. Sonnerup and L. J. Cahill. Magnetopause structure and attitude from Explorer 12 observations. *Journal of Geophysical Research*, 72(1):171, 1967. ISSN 0148-0227. doi: 10.1029/JZ072i001p00171.

B. U. Ö. Sonnerup, G. Paschmann, I. Papamastorakis, N. Sckopke, G. Haerendel, S. J. Bame, J. R. Asbridge, J. T. Gosling, and C. T. Russell. Evidence for magnetic field reconnection at the Earth's magnetopause. *Journal of Geophysical Research*, 86(A12): 10049, 1981. ISSN 0148-0227. doi: 10.1029/JA086iA12p10049.

M. Swisdak. Quantifying gyrotropy in magnetic reconnection. *Geophysical Research Letters*, 43(1):43–49, Jan. 2016. ISSN 0094-8276, 1944-8007. doi: 10.1002/2015GL066980.

R. B. Torbert, C. T. Russell, W. Magnes, R. E. Ergun, P.-A. Lindqvist, O. LeContel, H. Vaith, J. Macri, S. Myers, D. Rau, J. Needell, B. King, M. Granoff, M. Chutter, I. Dors, G. Olsson, Y. V. Khotyaintsev, A. Eriksson, C. A. Kletzing, S. Bounds, B. Anderson, W. Baumjohann, M. Steller, K. Bromund, G. Le, R. Nakamura, R. J. Strangeway, H. K. Leinweber, S. Tucker, J. Westfall, D. Fischer, F. Plaschke, J. Porter, and K. Lappalainen. The FIELDS Instrument Suite on MMS: Scientific Objectives, Measurements, and Data Products. *Space Science Reviews*, 199(1-4):105–135, Mar. 2016. ISSN 0038-6308, 1572-9672. doi: 10.1007/s11214-014-0109-8.

R. B. Torbert, J. L. Burch, T. D. Phan, M. Hesse, M. R. Argall, J. Shuster, R. E. Ergun, L. Alm, R. Nakamura, K. J. Genestreti, D. J. Gershman, W. R. Paterson, D. L. Turner, I. Cohen, B. L. Giles, C. J. Pollock, S. Wang, L. J. Chen, J. E. Stawarz, J. P. Eastwood, K. J. Hwang, C. Farrugia, I. Dors, H. Vaith, C. Mouikis, A. Ardakani, B. H. Mauk, S. A. Fuselier, C. T. Russell, R. J. Strangeway, T. E. Moore, J. F. Drake, M. A. Shay, Y. V. Khotyaintsev, P. A. Lindqvist, W. Baumjohann, F. D. Wilder, N. Ahmadi, J. C. Dorelli, L. A. Avanov, M. Oka, D. N. Baker, J. F. Fennell, J. B. Blake, A. N. Jaynes, O. L. Contel, S. M. Petrinec, B. Lavraud, and Y. Saito. Electron-scale dynamics of the diffusion region during symmetric magnetic reconnection in space. *Science (80-.).*, 2018. ISSN 10959203. doi: 10.1126/science.aat2998.

J. P. Vallee. Cosmic Magnetism in 15 Easy Steps. *Journal of the Royal Astronomical Society of Canada*, 92:83, Apr. 1998. ISSN 0035-872X.

V. M. Vasyliunas. Theoretical Models of Magnetic Field Line Merging , 1. *Rev. Geophys. Sp. Phys.*, 13(1), 1975. ISSN 8755-1209. doi: 10.1029/RG013i001p00303.

L. B. Wilson, A. L. Brosius, N. Gopalswamy, T. Nieves-Chinchilla, A. Szabo, K. Hurley, T. Phan, J. C. Kasper, N. Lugaz, I. G. Richardson, C. H. K. Chen, D. Verscharen, R. T. Wicks, and J. M. TenBarge. A Quarter Century of *Wind* Spacecraft Discoveries. *Reviews of Geophysics*, 59(2), June 2021. ISSN 8755-1209, 1944-9208. doi: 10.1029/2020RG000714.

S. Xiao, T. Zhang, G. Wang, M. Volwerk, Y. Ge, D. Schmid, R. Nakamura, W. Baumjohann, and F. Plaschke. Occurrence rate of dipolarization fronts in the plasma sheet: Cluster

observations. *Ann. Geophys.*, 35(4):1015–1022, 2017. ISSN 14320576. doi: 10.5194/angeo-35-1015-2017.

T. Yeh and W. I. Axford. On the re-connexion of magnetic field lines in conducting fluids. *Journal of Plasma Physics*, 4(2):207–229, 1970. doi: 10.1017/S0022377800004967.

D. T. Young, J. L. Burch, R. G. Gomez, A. De Los Santos, G. P. Miller, P. Wilson, N. Paschalidis, S. A. Fuselier, K. Pickens, E. Hertzberg, C. J. Pollock, J. Scherrer, P. B. Wood, E. T. Donald, D. Aaron, J. Furman, D. George, R. S. Gurnee, R. S. Hourani, A. Jacques, T. Johnson, T. Orr, K. S. Pan, S. Persyn, S. Pope, J. Roberts, M. R. Stokes, K. J. Trattner, and J. M. Webster. Hot Plasma Composition Analyzer for the Magnetospheric Multiscale Mission. *Space Science Reviews*, 199(1-4):407–470, Mar. 2016. ISSN 0038-6308, 1572-9672. doi: 10.1007/s11214-014-0119-6.

T. L. Zhang, W. Baumjohann, R. Nakamura, A. Balogh, and K.-H. Glassmeier. A wavy twisted neutral sheet observed by CLUSTER. *Geophys. Res. Lett.*, 29(19):5–1–5–4, 2002a. ISSN 0094-8276. doi: 10.1029/2002gl015544.

T. L. Zhang, W. Baumjohann, R. Nakamura, A. Balogh, and K.-H. Glassmeier. A wavy twisted neutral sheet observed by CLUSTER. *Geophys. Res. Lett.*, 29(19):5–1–5–4, 2002b. ISSN 0094-8276. doi: 10.1029/2002gl015544.